INVESTIGATION OF WALL-MODELED LARGE EDDY SIMULATIONS FOR JET AEROACOUSTICS

A Dissertation

Submitted to the Faculty

of

Purdue University

by

Shanmukesh Vankayala

In Partial Fulfillment of the

Requirements for the Degree

of

Doctor of Philosophy

December 2018

Purdue University

West Lafayette, Indiana

THE PURDUE UNIVERSITY GRADUATE SCHOOL
STATEMENT OF DISSERTATION APPROVAL

Dr. Gregory A. Blaisdell, Chair

School of Aeronautics and Astronautics

Dr. Anastasios S. Lyrintzis

Department of Aerospace Engineering, Embry-Riddle

Dr. Tom I. Shih

School of Aeronautics and Astronautics

Dr. Haifeng Wang

School of Aeronautics and Astronautics

Approved by:

Dr. Weinong Chen

Head of the School Graduate Program

ACKNOWLEDGMENTS

I express my sincere thanks to my advisor, Dr. Gregory Blaisdell for his support, guidance and encouragement given to me throughout this work. His knowledge, abundant patience and honesty has been critical in shaping and completion of my research work. I am grateful to Dr. Anastasios Lyrintzis of Embry-Riddle Aeronautical University for serving on my dissertation committee and providing me with valuable feedback and suggestions throughout this work. I also want to thank Profs. Tom Shih and Haifeng Wang for agreeing to be on my dissertation committee and reviewing my thesis. I am very thankful to Don Brier of the Purdue Graduate School for hiring me as a graduate assistant, which helped me in funding most part of my graduate studies. I am indebted to the help provided by Dr. Nitin Dhamankar of Intel Corp., and Dr. Kurt Aikens of Houghton College. This work would not have been completed without their help. I really appreciate Dr. Dhamankar for his patience in explaining and making me understand the code and using it. Lastly, I would like to thank all my family and friends for their support during my doctoral studies.

Part of this work utilized computational resources provided by the Extreme Science and Engineering Discovery Environment (XSEDE, sponsored by the NSF under grant number ACI 1053575) under allocation TG-ASC040044N on the Stampede and Stampede 2 supercomputers at the Texas Advanced Computing Center (TACC). Simulations in the current work were also performed on the Conte, and Rice community clusters of the Rosen Center for Advanced Computing (RCAC) at Purdue. I also thank the staff of both RCAC and TACC for providing technical support in resolving issues encountered during the use of their clusters.

TABLE OF CONTENTS

Page

LIST OF TABLES

Table Page

LIST OF FIGURES

Figure Page

SYMBOLS

Roman Symbols

B	Log-law integration constant
c	Speed of sound
C_f	Skin friction coefficient
C_p	Pressure coefficient
C_S	Smagorinsky constant
D	Diameter
e_t	Total energy per unit volume
f	An arbitrary flow variable, frequency
$\boldsymbol{F}, \boldsymbol{G}, \boldsymbol{H}$	Flux vectors in curvilinear coordinates
h	Uniform grid spacing on the transformed computational grid or channel half-height
H	Shape factor, δ^*/θ transformed computational grid
L_r	Reference length
J	Determinant of Jacobian of the coordinate transformation
k	Turbulent kinetic energy
M	Mach number
N	Number of grid points
p	Static pressure
$p'_L,\ p'_T,\ p'_Q$	Loading noise, thickness noise, and quadrupole noise in the FWH method
Pr	Prandtl number
Pr_t	Turbulent Prandtl number

q_i	Resolved heat flux
$\boldsymbol{Q}$	Vector of conservative flow variables
Q_i	SGS heat flux
r	radial coordinate, radius
R	Radius
Re	Reynolds number
S	Sutherland's constant
St	Strouhal number
T	Static temperature or simulation reference time
U	Velocity magnitude
$\vec{U}_c$	Convection velocity for Ikeda's method
$U_{\|\|}$	Magnitude of velocity parallel to wall
$u,\ v,\ w$	Cartesian velocity components
u_τ	Friction velocity
$x,\ y,\ z$	Cartesian coordinates

Greek Symbols

α_f	Spatial filtering parameter
γ	Ratio of specific heats for air
δ_{99}	Boundary layer thickness based on a location where the streamwise velocity is 99% of the freestream velocity
δ^*	Boundary layer displacement thickness
Δs	Grid spacing in direction s
Δt	Time-step size
ΔT	Time period
θ	Angle, azimuthal coordinate, boundary layer momentum thickness
Θ	Angular location from downstream jet axis
κ	Log-law von Kármán constant

μ	Dynamic molecular viscosity
ν	Kinematic molecular viscosity
$\xi,\ \eta,\ \zeta$	Generalized curvilinear coordinates
Π	Coles' wake strength parameter
ρ	Density
τ	Shear stress, retarded time, or reference time unit, L_r/U_r
τ_w	Wall shear stress
Ψ_{ij}	SGS stress tensor

Accent Marks

$\widetilde{(\ )}$	Favre-filtered quantity
$\widehat{(\ )}$	Resolved-scale component
$\breve{(\ )}$	Spatially-filtered quantity
$\overline{(\ )}$	Time-averaged quantity
$\vec{(\ )}$	Vector quantity

Subscripts

$(\ )_0$	Stagnation quantity
$(\ )_\infty$	Freestream quantity
$(\ )_J$	Quantity at the nozzle exit centerline
$(\ )_{ref}$	Reference quantity
$(\ )_v$	Viscous quantity
$(\ )_w$	Quantity at the wall
$(\ )_\theta$	Quantity along the azimuthal direction

Superscripts

$(\ )'$	Differentiated quantity, perturbation quantity
$(\ )^*$	Dimensional quantity
$(\ )^+$	Quantity in inner (viscous) wall units

$(\ )^p$	Physical component of the indicated quantity in the generalized coordinate directions
$(\ )^T$	Transpose of the given vector or matrix

ABBREVIATIONS

ADS	Acoustic Data Surface for the Ffowcs Williams-Hawkings method
AIAA	American Institute of Aeronautics and Astronautics
CAA	Computational Aeroacoustics
CFD	Computational Fluid Dynamics
CFL	Courant-Friedrichs-Lewy (condition number)
DNS	Direct Numerical Simulation
DSM	Dynamic Smagorinsky Model
EWM	Equilibrium Wall Model
FAA	Federal Aviation Administration
FTC	Flow-Through-Cycle
FWH	Ffowcs Williams-Hawkings
GEWM	Generalized Equilibrium Wall Model
GNEWM	Generalized Non-Equilibrium Wall Model
I/O	Input/Output from Computer Code
ILES	Implicit Large Eddy Simulation
ILS	Integral Length Scale
IWM	Integral Wall Model
LES	Large Eddy Simulation
MP	Matching Point
MPI	Message Passing Interface
NASA	National Aeronautics and Space Administration
NPR	Nozzle Pressure Ratio
OASPL	Overall Sound Pressure Level
ODE	Ordinary Differential Equation
PDE	Partial Differential Equation

PIV	Particle Image Velocimetry
RANS	Reynolds-Averaged-Navier-Stokes
rms	Root Mean Square
SGS	Sub-Grid Scale
SMC	Short Metal Chevron (series of nozzles)
SPL	Sound Pressure Level
TACC	Texas Advanced Computing Center
TKE	Turbulent Kinetic Energy
TTR	(Nozzle) Total Temperature Ratio

ABSTRACT

Vankayala, Shanmukesh Ph.D., Purdue University, December 2018. INVESTIGATION OF WALL-MODELED LARGE EDDY SIMULATIONS FOR JET AEROACOUSTICS. Major Professor: Gregory A. Blaisdell.

In recent years, jet noise has been an active area of research due to an increase in the use of aircraft in both commercial and military applications. To meet the noise standards laid out by government agencies, novel nozzle design concepts are being developed with an aim to attenuate the noise levels. To reduce the high costs incurred by experiments, simulation techniques such as large eddy simulation (LES) in combination with a surface integral acoustic method have received much attention for investigating various nozzle concepts. LES is utilized to predict the unsteady flow in the nearfield, whereas the surface integral acoustic method is used for the computation of noise in the farfield. However, Reynolds numbers at which nozzles operate in the real world are very high making wall-resolved LES simulations prohibitively expensive. To make LES simulations affordable, wall-models are being used to model the flow in the near wall region. Using a highly scalable, sixth-order finite-difference-based, in-house LES code, both wall-resolved and wall-modeled simulations of jets through the baseline short metal chevron (SMC000) nozzle were carried out earlier using an implicit LES (ILES) approach. However, differences exist in noise levels between the two simulations. Understanding the cause and reducing the differences between the two methodologies, while at the same time improving the fidelity of the wall-modeled LES is the main aim of the present work. Three new wall-models are implemented in the in-house LES code. A generalized equilibrium wall-model (GEWM) is implemented along with two wall-models that can account for non-equilibrium effects. First, a series of preliminary SMC000 wall-modeled LES simulations were performed and analyzed using the GEWM. The effect of turbulent length scales and

velocity fluctuations specified at the inflow, wall-model formulation, and wall-normal grid refinement are analyzed. The adjustment of the fluctuations levels at the inflow proves to be useful in producing flowfields similar to that of the wall-resolved simulation. The newly implemented wall-models are validated for non-canonical problems such as an accelerating boundary layer developing over a flat plate and flow through a converging-diverging channel. It is noticed that the Reynolds number should be high enough for the non-equilibrium wall-models to be effective. At low Reynolds numbers, both equilibrium and non-equilibrium models produce similar wall shear-stresses. However, the wall shear stress boundary conditions supplied by the wall-models do not affect the mean velocity, turbulent kinetic energy, and Reynolds shear stress. Since all the wall-models produce similar results, and the GEWM is the most economical among the implemented wall-models, it is used in performing two wall-modeled LES SMC000 nozzle simulations for noise predictions. The inflow velocity and density fluctuations are varied between the simulations. The first SMC000 simulation uses similar inflow conditions as the previous wall-resolved SMC000 simulation. The second wall-modeled simulation was carried out by reducing the density and velocity fluctuations added to the mean flow at the inlet by 65%. The flowfield and acoustics agree reasonably well in comparison with the wall-resolved LES and similar experiments. Lowering of the velocity and density fluctuations in the wall-model LES improves the agreement of the far-field noise predictions with the wall-resolved LES at most observer locations. However, the preliminary SMC000 simulations performed using a higher Reynolds number and Mach number than that of the previous case show that the approach of adjusting the velocity and density fluctuations added to the mean flow have minimal impact on the developing flowfield which in turn affects the farfield noise. Thus, unless a more effective wall-modeling method is developed, possibly employing an explicit SGS model, the postdictive process of using a wall-model while adjusting the velocity and density fluctuations, seems to be an affordable tool for testing various nozzle designs, subject to the Reynolds number and Mach number being used.

1. INTRODUCTION

1.1 Motivation and Background

Jet noise is one of the significant sources of noise generated during the flight of an aircraft that could constrain the natural growth of the air transportation system. With air transportation becoming more widely available, jet noise has reached levels such that it not only affects the passengers and crew of an aircraft but also others who are in the close vicinity of an aircraft that is in operation. The ever-increasing levels of noise have adverse impacts on humans, from annoyance to hearing loss. With these, government agencies, such as the Federal Aviation Administration (FAA), that regulate several aspects of civil aviation started to impose stricter rules for certifying new aircraft. The certification of new aircraft types requires them to follow the noise standards prescribed by Federal Aviation Regulations (FAR), Part 36. The FAA through FAR, Part 150 has laid out recommended guidelines for the maximum noise exposure levels that are acceptable for people living in the vicinity of airports. For residential areas, acceptable noise levels are less than 65dB. These restrictions could impact the airport and airspace operations, such as arrival or departure flight paths, the maximum number of airplanes that the airports or airspace can handle at any point of time, etc. The government spends huge sums of money on sound insulation programs, medical claims, etc. For example, between 1977 and 2006, the Navy spent about $8.4 billion for noise related disability medical claims of carrier deck personnel who work in the harsh noise environment of military aircraft [1]. The above factors have motivated many researchers to have a better understanding of the generation and propagation of noise and to develop new technologies that reduce noise levels.

The interaction of jet exhaust with the surrounding air generates jet noise. Both fine and large-scale turbulent structures present in the jet contribute to noise gener-

ation [2]. For subsonic jets, large-scale turbulent structures play a dominant role in noise generation. Unlike subsonic jets, both fine and large-scale turbulent structures play an essential role in noise generation in supersonic jets. Various parameters such as acoustic Mach number, temperature of the jet, etc., influence the jet and in-turn affect the noise spectrum of the jet. The complexity of noise generation mechanisms have made it very difficult to understand from the limited data that can be obtained through experiments. With the advent of computers having higher processing and parallelization capabilities, computational aeroacoustics (CAA) has become one of the important tools to analyze noise generation mechanisms as more detailed information about the acoustic field and flowfield can be obtained. Most CAA methodologies used today employ a two-step process. First, the flowfield data is computed by solving the governing equations of fluid dynamics. Samples of time-dependent flowfield data are collected over a surface that encloses the nonlinear acoustic source region. Then, these acoustic sources are used as input to predict the propagating noise by using an analytic solution of the governing acoustic wave equation.

The computational fluid dynamics (CFD) techniques available to compute the nonlinear flowfield usually fall into one of the three categories: direct numerical simulation (DNS), large eddy simulations (LES) and Reynolds averaged Navier-Stokes (RANS). However, when simulating high Reynolds number turbulent flows, a wide range of length and time scales are present, which requires very fine meshes to solve and makes DNS computationally very expensive. It has been estimated that computational cost increases as the cube of the Reynolds number [3]. This makes DNS infeasible for solving high Reynolds number turbulent flows of practical interest as tremendous resolution requirements are necessary that are far beyond the capability of even the fastest supercomputers available today. On the other hand, RANS uses less computational time and resources, but the accuracy of the flowfield is compromised due to time averaging. Also, RANS does not provide a time-dependent solution. Therefore, noise cannot be computed directly, and RANS-based approaches rely on noise models, which have been shown to be inaccurate except for the simple round jet

for which they have been tuned. This makes LES a good option to solve high Reynold number turbulent flows with lower computational cost. In LES, the flow problem is solved by only considering the larger three-dimensional turbulent motions which are represented by the Navier-Stokes equations filtered in space and a turbulence model is used to represent the residual subgrid scale (SGS) stress tensor.

The advantages of LES over other computational approaches for flowfield prediction have increased the use of LES for noise predictions [4]. In recent years, LES along with surface integral methods are extensively used to propagate noise to the farfield [5]. The surface integral methods include Kirchhoff's [6] and porous Ffowcs Williams-Hawkings (FWH) [7] methods. However, the robustness of the FWH method in the placement of the surface over which time-dependent flowfield data are collected gives it an added advantage [5]. Therefore, in the current work, LES in combination with FWH are used to simulate the flowfield and predict the farfield noise.

Various jet parameters, such as the perimeter of the jet, length of the potential core and mixing rates in the shear layer, have suppressed noise levels. This led researchers to look into different nozzle designs that affect the aforementioned jet parameters and reduce jet noise.Various noise-reducing design ideas, such as chevrons [8], lobed mixers [9], beveling [10], hard-wall corrugations [11] and fluidic injectors [12, 13], have been tested. But simulations including nozzle walls are expensive due to the formation of the turbulent boundary layer along the nozzle walls. The boundary layer development depends on the Reynolds number. For a turbulent boundary layer, Larsson et al. [14] defines the inner layer as $y/\delta < 0.2$ and the outer layer as $y/\delta \geq 0.2$. Table 1.1 summarizes the estimates of grid points necessary to resolve the inner and outer layers for wall-bounded flows by various authors. Chapman's [15] estimates were based on the wall-resolved simulation of a flat plate turbulent boundary layer, whereas the estimates of Larsson et al. [14] were based on a practical example of a NACA0012 airfoil. These estimates show the necessity of a highly refined grid and its scaling with Reynolds number to capture the dynamics of the small-scale motions

of a wall-bounded flow. At the same time, the time-step size has to be decreased due to the stringent Courant-Friedrichs-Lewy (CFL) condition where $\Delta t \propto \frac{\Delta x}{U}$. These factors increase the overall cost of the simulation, and with current computational capabilities it is not feasible to run simulations for practical applications that operate at very high Reynolds numbers. For example, Dhamankar et al. [16] utilized a total of 2.7 million core-hours to perform a wall-resolved large eddy simulation of a Mach 0.9 isothermal jet through a short metal chevron (SMC) baseline nozzle [8, 17] operating at a Reynolds number of 10^5 using 3792 cores on the Kraken supercomputer at the National Institute for Computational Sciences to collect flowfield and acoustic data. The grid used in the simulation of Dhamankar et al. [16] consists of 125 million grid points.

Table 1.1. Estimates of Reynolds number scaling for number of grid points required for wall bounded flows.

Author	**Grid points in inner layer**	**Grid points in outer layer**
Chapman [15]	$Re^{1.8}$	$Re^{0.4}$
Larsson, et al. [14]	$Re^{2.16}$	$Re^{0.58}$

Due to the high costs involved in resolving the inner layer which accounts for less than 20% of the entire boundary layer, researchers have developed alternatives to bypass the computation of the inner layer. The contribution of the eddies in the inner layer to the momentum transport is modeled. The simulations with inner layer modeling use a coarse grid in the near-wall region along with an increased time-step size, which helps to significantly reduce the simulation cost. However, when coarse grids are used, the velocity gradient at the wall due to the imposed no-slip condition is underpredicted, leading to an underprediction of the wall-shear stress. Therefore, the inner layer modeling should be robust enough to supply approximate boundary conditions to the resolved LES in the outer layer by modeling the momentum transport

of the under-resolved small-scale eddies near the wall dictated by the grid resolution. In 1970, Deardorff [18] formulated one of the first wall models neglecting viscosity and making the model valid for infinite Reynolds number. Second order derivatives of the mean flow are included in the boundary conditions imposed on the wall such that the mean flow follows the logarithmic law of the wall. This formulation also assumes that the turbulence is isotropic in the near-wall region. With the widespread use of LES in engineering applications involving high Reynolds number flows, many new wall-models have been developed.

A comprehensive review of wall-models is given by Piomelli and Balaras [19], Piomelli [20] and Larsson et al. [14]. There are subtle differences in how different researchers categorize these wall models. We follow the categorization based on [14] and give a brief description of various wall-models. Wall-modeled LES can be categorized based on how the LES is defined. The approaches in which LES is defined in the entire flow field is classified as wall-stress models and approaches in which the LES is defined above a certain height from the wall is classified as Hybrid LES/RANS.

The wall-stress models are formulated to estimate the wall shear stress from the flow variables at a grid location specified above the wall. The wall shear stress can be written as

$$\tau_{w,i} = f(u_i, \rho, \nu, \frac{dp}{dx_i}), \tag{1.1}$$

where f is a function that can relate the flow variables with the stress in the wall tangential direction. The function f can be an algebraic expression, such as the logarithmic law, which can be solved by root-finding methods or an ODE, such as the equilibrium model [21], in which the convection and pressure gradient terms are balanced in the axial mean-momentum equation and solved numerically. PDE based methods also fall under this category of wall-stress models, which some researchers classify as zonal methods.

The approximate boundary conditions suggested by Schumann [22] is the first successful application of a wall-model. The wall-model is used in the simulations of channel and annuli flows at finite Reynolds numbers. Schumann uses algebraic

expressions to relate the instantaneous wall stresses with the velocity obtained from the first grid point off the wall. The streamwise wall shear stress is also dependent on the mean streamwise velocity averaged in the plane parallel to the wall and the mean wall shear stress which should be known *a priori*. For example, in channel flows, the imposed pressure gradient can be used to specify the mean wall shear stress. For flows in which the mean wall shear stress cannot be obtained *a priori*, the logarithmic law can be solved iteratively to compute the mean wall shear stress [23]. Alternatively, the wall shear stress can also be obtained from a RANS simulation [24]. A linear velocity profile assumption along with constant eddy viscosity is used to approximate the spanwise component of the wall shear stress. Grotzbach [23] relaxed the *a prior* requirement of mean wall shear stress in Schumann's formulation. Grotzbach computed the friction velocity by iteratively solving the logarithmic law and obtained the wall shear stress. Piomelli et al. [25] modified Schumann's model by introducing a streamwise displacement in its formulation. The use of streamwise displacement is found to increase the correlation between the wall shear stress and velocity which in turn improves the accuracy of Schumann's model [26]. The wall-models discussed so far rely on the space and time averaged velocity at the sampling grid location. Mason and Callen [27] used the instantaneous velocity such that the logarithmic law is satisfied both locally and instantaneously.

The wall-stress models discussed so far rely on the logarithmic law. However, there are other models like the model proposed by Werner and Wengle [28] which computes the instantaneous wall shear stress assuming the instantaneous velocity at the sampling grid location satisfies a power law. The logarithmic law can also be replaced by a unified law such as the Spalding's law [29] which extends the logarithmic law's applicability to the viscous sub-layer and buffer layer. Several modifications have been made to the logarithmic law to account for the effects of local acceleration and pressure gradients [30–33].

In another class of wall-stress models, instead of using an algebraic expression, governing equations are solved numerically to obtain the wall shear stress. The tur-

bulent boundary layer equations are solved on an embedded grid placed between the wall and the first grid point to capture some of the non-equilibrium effects. Such a method was first implemented by Balaras et al. [34] for plane channel flow, square duct and rotating channel flow. Unlike the use of a Prandtl mixing-length model used in reference [34] for the computation of eddy viscosity, Diurno et al. [35] used the Spalart-Allmaras model [36] for calculation of the eddy-viscosity present in the turbulent boundary layer equations and found improved results in their simulations of the backward-facing step flow. Wang and Moin [37] used a dynamically adjusted mixing-length eddy viscosity for flows past asymmetric trailing-edge and found good agreement with resolved LES results. Building upon the work in references [34, 37], Kawai and Larsson [38] suggested an improved wall-model which takes into account how the turbulence length scale changes with wall distance in the logarithmic region, grid resolution, and the resolution-characteristics of the numerical method. By dynamically computing the eddy viscosity parameter, κ, Kawai and Larsson [38] found better skin-friction predictions for both equilibrium and non-equilibrium flows.

All the wall-stress models discussed so far are based on physics. Another set of wall-stress models were developed based on non-physics-based arguments. An example of such a method is the one based on suboptimal control strategy by Nicoud [39], who uses instantaneous wall stress as a control to force the outer LES towards a log law solution.

Hybrid LES/RANS methods are a group of methods in which the domain is split into a near-wall region and an exterior region, and different turbulence models are applied in each of the regions. Some methods use the same turbulence model, such as detached eddy simulations (DES) [40], whereas others use LES in the exterior region and different choices of RANS models in the near-wall region. Larsson et al. [14] classified these models based on how the near wall region height is defined, whether set by the user, called zonal methods, or set by the grid or solution, called seamless methods. Researchers have developed many zonal methods by altering the RANS models. The works of Baurle et al. [41] for the simulation of cavity flows and

Temmerman et al. [42] for the simulation of high Reynolds number fully developed channel flows utilize zonal methods. More examples of such zonal methods can be found in references [14, 20, 43].

There is no single method which can be deemed as accurate. There are several challenges involved, and some errors plague all the methods. For example, a standard error is the logarithmic law mismatch error [44] where the mean velocity profile in viscous units ends up above the log-law called a positive mismatch or below the log-law called a negative mismatch. The algebraic wall-stress models relying on the equilibrium assumption are known to not perform well with flows subjected to shallow separation, or with strong pressure gradients [34]. Although PDE based wall-stress models perform better for non-equilibrium flows, their requirement to have an embedded grid makes them not practical for realistic and complex geometries [14]. Moreover, the need for the embedded grid to be refined in the wall-normal direction on which PDEs are to be solved increases the simulation costs. On the other hand, Hybrid LES/RANS methods require a separate grid in the near-wall region with grid points located in the viscous-sublayer over which governing equations need to be solved. This adds additional costs and also requires the use of different numerical techniques in each of the regions. Damped velocity fluctuations were observed in the crossover region of RANS and LES [43] causing a reduction of turbulence in the LES region. With already high simulation costs involved in simulating high Reynolds number flows, it is necessary to choose a wall model which does not add more cost to the already expensive simulations. Among the different wall model formulations, the algebraic wall stress methods are the least expensive. Moreover, they are easy to implement and can be used with the underlying numerical methods avoiding complications of programming. For example, LES/RANS methods require the implementation of a RANS model and an implicit time advancement scheme. An implicit time advancement scheme facilitates the use of a large time step with fine grid resolution required by RANS models in the wall-normal direction. Because of the above advantages, the

algebraic wall stress methods are a viable choice for use with already expensive jet simulations.

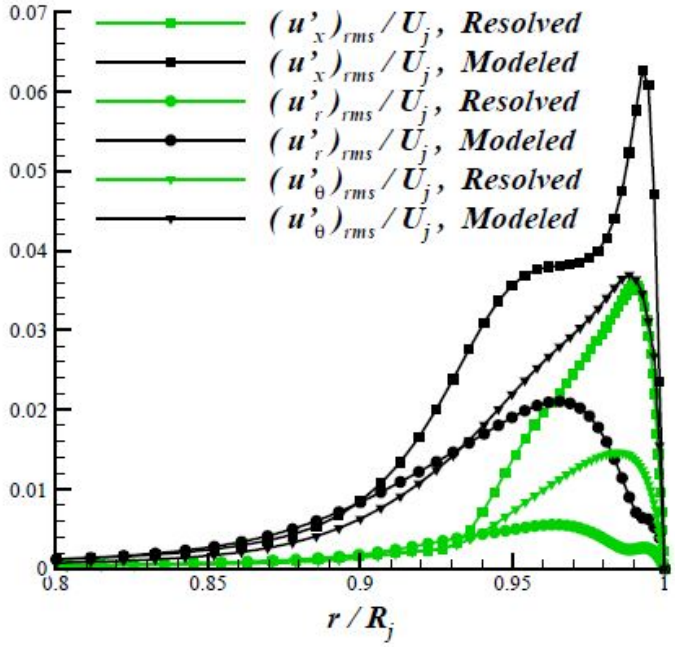

(a) Normal Reynolds stresses.

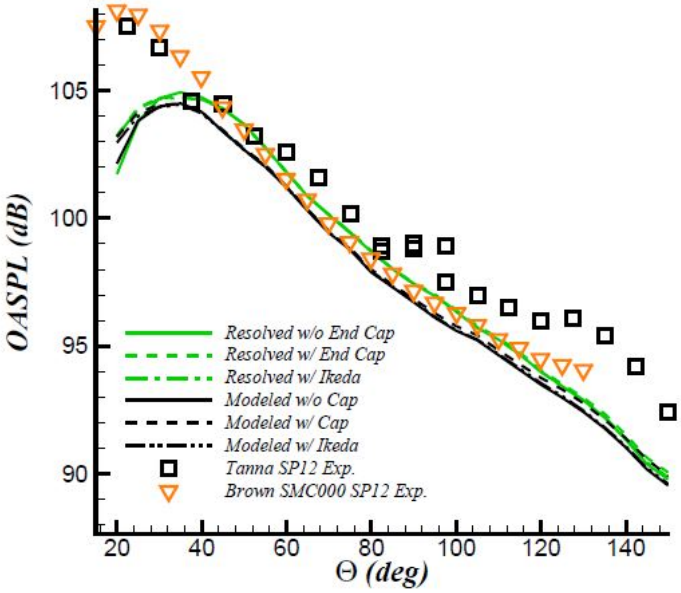

(b) OASPL at R = $144R_j$.

Figure 1.1. Comparision between wall-resolved and wall-modeled cases [45].

Martha [46] and Situ [47] developed an in-house LES solver initially to simulate subsonic jets, which was extended by Dhamankar [48] by incorporating various wall, inflow and outflow boundary conditions. Aikens [45] added the capability of shock capturing for handling supersonic flows along with an equilibrium wall model. More recently, Dhamankar [49] implemented immersed boundary methods, which extended the ability of the code to handle complex nozzle shapes. Several wall-resolved and wall-modeled simulations have been carried out using the in-house LES solver. The wall-resolved simulations of subsonic converging nozzles [16, 46] and supersonic converging-diverging nozzles [50] performed with the in-house LES solver showed good accuracy of the results. The wall-model implemented into the solver has been validated for both quasi-incompressible [51] and compressible [45] flat plate boundary layers. It has also been used to evaluate the noise benefits of a chevron nozzle operating at a subsonic test condition [49], the impact of beveling [52] the nozzle exit for converging-diverging nozzles operating under typical takeoff conditions (supersonic overexpanded), and the effectiveness of fluidic injection [53–55].

The wall-resolved [48] and wall-modeled [45] cases simulated for a Mach 0.9 isothermal jet through a baseline short metal chevron (SMC) nozzle [8] operating at a Reynolds number of 10^5 using the in-house LES solver showed some discrepancies. The operating conditions are referred to as SP12 by Tanna et al. [56]. There are considerable differences between the normal Reynolds stresses at the nozzle exit which in turn affects the noise levels obtained in the farfield. Due to the higher turbulence levels for the wall-modeled case, the noise levels in the farfield are lower compared with the wall-resolved case. The normal stresses at the nozzle exit and the overall sound pressure level (OASPL) at an observer location of 144 jet exit radii for these cases can be seen in figure 1.1. These trends are consistent with the findings of Bogey et al. [57]. They carried out numerical simulations of an isothermal round jet operating at Mach number 0.9 and Reynolds number $Re_D = 10^5$. Bogey et al. found that with an increase in initial turbulence levels, the vortex roll-ups and pairing that usually take place in laminar-turbulent flow transition disappear in the shear layer

causing it to develop more slowly than with lower turbulence levels, which indeed lengthens the jet's potential core and also contributes to the lower noise levels. Given the above discussion, the primary objective of the current research is to improve the fidelity of the current wall-modeled simulations for jet noise predictions by assessment and development of the capabilities of the current in-house LES code.

1.2 Objectives

To this end, the research can be decomposed into the following parts:

1. **Preliminary wall-modeled simulations of the SMC000 nozzle using a short domain.**

   (a) In the previous wall-modeled simulation [45], at the matching point location, $y^+ < 50$, and it is typically between 8 and 12. The wall-model utilized is valid for $y^+ < 10.8$ or $y^+ > 50$. In between, the predicted wall shear stress is not accurately modeled. So, a simulation utilizing a generalized equilibrium wall model (GEWM) [29], which is valid for $0 < y^+ < 0.3\delta^+$, is carried out. The GEWM is implemented as part of this work.

   (b) There are differences between the wall-resolved [16] and wall-modeled [45] simulations in the specification of turbulent length scales in the axial and azimuthal directions at the inflow boundary. They are given in table 1.2. The impact of this difference is unknown on the flowfield. So, simulations are carried out using length scales that are consistent with the wall-resolved case.

   (c) To understand the impact of the velocity fluctuations specified at the inflow, simulations are carried out by reducing the magnitude of the fluctuations.

   (d) Finally, one case is simulated to test the sensitivity of grid-refinement in the wall-normal direction.

Table 1.2. Turbulent length scales used in previous simulations

Simulation	**Axial** (δ_{99})	**Radial** (δ_{99})	**Azimuthal** (δ_{99})
Wall-Resolved [16]	1.2	0.4	0.4
Wall-Modeled [45]	1.6	0.4	0.8

2. **Implementation and validation of non-equilibrium wall-models in the in-house LES code.**

   The equilibrium wall-model implementation has been previously validated for the canonical turbulent boundary layer generated over a flat plate with zero pressure gradient for both quasi-incompressible [51] and compressible [45] cases. The quasi-incompressible case was simulated to obtain a Reynolds number based on momentum thickness of $Re_\theta = 13,000$, whereas the compressible case operates at Mach 1.69 and obtains $Re_\theta = 31,000$. Results of both simulations agree well with experiments at matching Reynolds numbers. Various grid resolutions were tested with good accuracy of the results.

   However, due to discrepancies noticed in the wall-modeled SMC000 simulations, there is a need for the current implementation to be throughly investigated for flows involving favorable pressure gradients (FPG) as their effects are neglected in the equilibrium-stress models used in the previous implementation. Flows subjected to acceleration tend to re-laminarize making the wall-model inaccurate. Depending on the severity of the acceleration, accelerating boundary layers that are turbulent initially may deviate from the standard laws valid for a turbulent boundary layer. An accelerating boundary layer exhibiting this kind of behavior is said be in a laminarescent state. On further acceleration, the boundary layer completely re-laminarizes and attains a laminar state. Thorough reviews of the boundary layers that are undergoing re-laminarization (laminarescent), re-laminarized and retransitioning are given by Narasimha and

Sreenivasan [58] and Sreenivasan [59]. Accelerating boundary layers are said to be in a re-transition state when they transition from laminar back to a turbulent state. This occurs when the source of the acceleration is cut off.

Due to the multitude of flow dynamics of accelerating boundary layers, there is a need for wall-models that account for pressure gradients effects. For this purpose, two non-equilibrium wall models by Shih et al. [33, 60] and Yang et al. [61] are implemented in the in-house LES code. These new wall-models along with the generalized equilibrium wall-model are validated using two test cases involving accelerating flows. The test cases are flow through a converging-diverging channel and a spatially developing accelerating boundary layer.

3. **Aeroacoustics of jets through an SMC000 nozzle.**

   Finally, the SMC000 nozzle flow simulations are carried out to gather both the near field turbulent statistics and farfield acoustics. The simulations are carried out using the wall-model which is best capable of accurately predicting the Reynolds stresses for flows involving accelerating boundary layers. Based on the results of the preliminary SMC000 simulations, first, the simulations are carried out for jets operating at the SP12 condition. However, due to the lack of available experimental flowfield data at the SP12 operating condition, the operating condition referred to as SP07 by Tanna et al. [56] is also used for the SMC000 simulations. At the SP07 operating condition, both experimental [62] and acoustic data [8] are available. The SP07 operating conditions correspond to an unheated jet operating at a Mach number of M=0.9832 and $Re = 10^6$. These simulations help in demonstrating the capabilities of the wall-modeled LES for flowfield and acoustic predictions.

1.3 Dissertation Organization

The dissertation is organized as follows. Chapter 2 gives a brief description of the LES and acoustic methodologies used in this work. The governing fluid flow

equations, boundary conditions, subgrid-scale modeling and the numerical methods used to solve these equations are described along with the Ffowcs Williams-Hawkings surface integral acoustic method. Chapter 3 presents the various wall-model boundary conditions used in the current work. Both the formulation and implementation details are provided. Chapter 4 discusses the SMC000 preliminary simulations that were performed to understand the cause of differences between the wall-resolved [48] and wall-modeled [45] simulations described in section 1.1. The validation results of the accelerating boundary layer developing over a flat plate and flow through a converging-diverging channel using the newly implemented wall-models are presented in Chapter 5. The near field turbulent statistics and farfield acoustics for the jet through an SMC000 nozzle are given in Chapter 6. Finally, in Chapter 7, a summary of the current work is given along with a few suggestions for future work.

2. LARGE EDDY SIMULATION AND ACOUSTIC METHODOLOGY

This chapter gives a brief description of the LES and acoustic methodologies used in this work. The methodologies have been incorporated into a 3-D solver by Uzun [63] to study the jet noise of flows in subsonic regime. Lo [64] incorporated shock-capturing schemes and extended the solver capability to handle supersonic flows. Building upon this work, a more robust, higher efficiency parallel solver has been developed by Martha [46] and Situ [47]. This version of the solver is utilized in the present work and referred to as the modular-LES code hereafter. Dhamanakar [48,49] implemented various boundary conditions and immersed boundary methods into the modular-LES code for more realistic jet flow simulations and simulations which can handle complex nozzle geometries. The wall-modeling and shock capturing capabilities have been added into the modular-LES code by Aikens [45].

First, the governing equations that describe the fluid flow are presented in section 2.1. Section 2.2 describes the various numerical methods used for solving the governing equations. The boundary conditions and subgrid-scale (SGS) modeling is presented in sections 2.3 and 2.4 respectively. It is then followed by a brief overview of the parallelization strategy and is given in section 2.5. Lastly, the details of the acoustic methodology utilized in the current work are covered in section 2.6.

2.1 Governing Equations

In LES, the turbulent flowfield is decomposed into a large-scale component $\bar{f}$ and a subgrid-scale component f_{SGS}. The large-scales are defined such that they are supported by the grid resolution and are solved explicitly. The unresolved subgrid-scales

and their impact on the large-scales are modeled. Hence, any arbitrary parameter f, when filtered by a low-pass filter, can be written as

$$f = \bar{f} + f_{SGS}. \tag{2.1}$$

For compressible flows, the large-scales are written in terms of Favre-filtered variable

$$\tilde{f} = \frac{\overline{\rho f}}{\bar{\rho}}. \tag{2.2}$$

When the filtering operation is applied, additional terms appear in the energy and momentum equations. They are the unresolved terms that represent the impact of the small-scales on the resolved large-scales and require modeling. An explicit or implicit approach can be followed to model the SGS terms. In the explicit approach, subgrid-scale models such as the classical Smagorinsky model [65], Dynamic Smagorinsky model (DSM) [66], Wall-Adapting Local Eddy-viscosity (WALE) model [67], etc., can be used to model the SGS terms. Multiple studies [68–72] used a spatial filter associated with the numerical method (described below in section 2.2) as an implicit SGS model and noticed results on par with the results of simulations carried out using an explicit SGS model. In the implicit approach, the physics of the small-scales are assumed to be represented by the dissipation provided by the grid and the spatial filter. The DSM formulation has also been implemented into the modular-LES code by Aikens [45] for meshes with Cartesian topologies. The details about the DSM formulation is given in section 2.4. The simulations using DSM were found to be more expensive than those simulations performed using the implicit approach [45,71]. Moreover, the use of DSM was found to be dissipative for jet noise studies [63, 71]. So, in most of the current work, the SGS terms are modeled implicitly, unless DSM is otherwise mentioned. The modeling of the SGS terms using the implicit approach is referred as ILES in this work.

The final conservative form of the three-dimensional compressible Favre-filtered Navier-Stokes equations in generalized coordinates that are to be solved numerically are

$$\frac{1}{J}\frac{\partial \mathbf{Q}}{\partial t} + \frac{\partial}{\partial \xi}\left(\frac{\mathbf{F} - \mathbf{F_v}}{J}\right) + \frac{\partial}{\partial \eta}\left(\frac{\mathbf{G} - \mathbf{G_v}}{J}\right) + \frac{\partial}{\partial \zeta}\left(\frac{\mathbf{H} - \mathbf{H_v}}{J}\right) = 0. \tag{2.3}$$

These equations are nondimensionalized using the quantities at the chosen reference location. They are: length, R^*_{ref}, density, ρ^*_{ref}, velocity, U^*_{ref}, pressure, $\rho^*_{ref}U^{*2}_{ref}$, time, R^*_{ref}/U^*_{ref} and temperature, T^*_{ref}. Generally, for nozzle flow simulations, the conditions at the nozzle exit are chosen as the reference quantities, with the radius of the nozzle at the exit usually chosen to be the reference length scale. However, for the simulations of the flat plate boundary layer, accelerating boundary layer and flow through the converging-diverging channel, the conditions at the inflow are chosen as reference quantities. For boundary layer flows, the inlet boundary layer thickness is used as the reference length scale, whereas the channel half-height is used as the reference length scale for simulations involving channel flows. The reference Reynolds number used in the modular-LES solver is also computed using the reference conditions that are considered depending on the problem type.

In equation 2.3, $\mathbf{Q}$ is the vector of conservative flow variables, $\mathbf{F}$, $\mathbf{G}$ and $\mathbf{H}$ are the inviscid flux vectors, $\mathbf{F_v}$, $\mathbf{G_v}$ and $\mathbf{H_v}$ are the viscous flux vectors, J is the Jacobian determinant of the transformation between physical (x, y, z) and computational coordinates (ξ, η, ζ) and t is the time. The quantities $\mathbf{Q}$, $\mathbf{F}$, $\mathbf{G}$, $\mathbf{H}$, $\mathbf{F_v}$, $\mathbf{G_v}$ and $\mathbf{H_v}$ are given as

$$\mathbf{Q} = [\bar{\rho} \;\; \bar{\rho}\tilde{u} \;\; \bar{\rho}\tilde{v} \;\; \bar{\rho}\tilde{w} \;\; \bar{\rho}\tilde{e_t}]^T, \tag{2.4}$$

$$\mathbf{F} = \begin{bmatrix} \bar{\rho}\tilde{U} \\ \bar{\rho}\tilde{u}\tilde{U} + \xi_x\bar{p} \\ \bar{\rho}\tilde{v}\tilde{U} + \xi_y\bar{p} \\ \bar{\rho}\tilde{w}\tilde{U} + \xi_z\bar{p} \\ (\bar{\rho}\tilde{e_t} + \bar{p})\tilde{U} \end{bmatrix} \quad \mathbf{G} = \begin{bmatrix} \bar{\rho}\tilde{V} \\ \bar{\rho}\tilde{u}\tilde{V} + \eta_x\bar{p} \\ \bar{\rho}\tilde{v}\tilde{V} + \eta_y\bar{p} \\ \bar{\rho}\tilde{w}\tilde{V} + \eta_z\bar{p} \\ (\bar{\rho}\tilde{e_t} + \bar{p})\tilde{V} \end{bmatrix} \quad \mathbf{H} = \begin{bmatrix} \bar{\rho}\tilde{W} \\ \bar{\rho}\tilde{u}\tilde{W} + \zeta_x\bar{p} \\ \bar{\rho}\tilde{v}\tilde{W} + \zeta_y\bar{p} \\ \bar{\rho}\tilde{w}\tilde{W} + \zeta_z\bar{p} \\ (\bar{\rho}\tilde{e_t} + \bar{p})\tilde{W} \end{bmatrix}, \tag{2.5}$$

$$\mathbf{F_v} = \begin{bmatrix} 0 \\ \xi_x(\tau_{xx} - \Psi_{xx}) + \xi_y(\tau_{xy} - \Psi_{xy}) + \xi_z(\tau_{xz} - \Psi_{xz}) \\ \xi_x(\tau_{yx} - \Psi_{yx}) + \xi_y(\tau_{yy} - \Psi_{yy}) + \xi_z(\tau_{yz} - \Psi_{yz}) \\ \xi_x(\tau_{zx} - \Psi_{zx}) + \xi_y(\tau_{zy} - \Psi_{zy}) + \xi_z(\tau_{zz} - \Psi_{zz}) \\ \tilde{u}F_{v2} + \tilde{v}F_{v3} + \tilde{w}F_{v4} - [\xi_x(q_x + Q_x) + \xi_y(q_y + Q_y) + \xi_z(q_z + Q_z)] \end{bmatrix}, \tag{2.6}$$

$$\mathbf{G_v} = \begin{bmatrix} 0 \\ \eta_x(\tau_{xx} - \Psi_{xx}) + \eta_y(\tau_{xy} - \Psi_{xy}) + \eta_z(\tau_{xz} - \Psi_{xz}) \\ \eta_x(\tau_{yx} - \Psi_{yx}) + \eta_y(\tau_{yy} - \Psi_{yy}) + \eta_z(\tau_{yz} - \Psi_{yz}) \\ \eta_x(\tau_{zx} - \Psi_{zx}) + \eta_y(\tau_{zy} - \Psi_{zy}) + \eta_z(\tau_{zz} - \Psi_{zz}) \\ \tilde{u}G_{v2} + \tilde{v}G_{v3} + \tilde{w}G_{v4} - [\eta_x(q_x + Q_x) + \eta_y(q_y + Q_y) + \eta_z(q_z + Q_z)] \end{bmatrix}, \quad (2.7)$$

$$\mathbf{H_v} = \begin{bmatrix} 0 \\ \zeta_x(\tau_{xx} - \Psi_{xx}) + \zeta_y(\tau_{xy} - \Psi_{xy}) + \zeta_z(\tau_{xz} - \Psi_{xz}) \\ \zeta_x(\tau_{yx} - \Psi_{yx}) + \zeta_y(\tau_{yy} - \Psi_{yy}) + \zeta_z(\tau_{yz} - \Psi_{yz}) \\ \zeta_x(\tau_{zx} - \Psi_{zx}) + \zeta_y(\tau_{zy} - \Psi_{zy}) + \zeta_z(\tau_{zz} - \Psi_{zz}) \\ \tilde{u}H_{v2} + \tilde{v}H_{v3} + \tilde{w}H_{v4} - [\zeta_x(q_x + Q_x) + \zeta_y(q_y + Q_y) + \zeta_z(q_z + Q_z)] \end{bmatrix}, \quad (2.8)$$

respectively.

In equation 2.4, $\bar{\rho}\tilde{e_t}$ is the total energy per unit volume given as

$$\bar{\rho}\tilde{e_t} = \frac{1}{2}\bar{\rho}\tilde{u_i}\tilde{u_i} + \frac{\bar{p}}{\gamma - 1}, \quad (2.9)$$

where $\bar{p}$ can be computed using the ideal gas law given in nondimensional form as

$$\bar{p} = \frac{\bar{\rho}\widetilde{T}}{\gamma M_{ref}^2}. \quad (2.10)$$

In the above expression, the Mach number, M_{ref} corresponds to the value at the reference location.

In equation 2.5, $\tilde{U}$, $\tilde{V}$ and $\tilde{W}$ are the contravarient velocity components in the generalized coordinate system and are computed using

$$\begin{bmatrix} \tilde{U} \\ \tilde{V} \\ \tilde{W} \end{bmatrix} = \begin{bmatrix} \xi_x & \xi_y & \xi_z \\ \eta_x & \eta_y & \eta_z \\ \zeta_x & \zeta_y & \zeta_z \end{bmatrix} \begin{bmatrix} \tilde{u} \\ \tilde{v} \\ \tilde{w} \end{bmatrix}. \quad (2.11)$$

The grid metric terms arising due to the coordinate transformation between the physical and computational space are evaluated by writing the metric terms in the conservation form as done in references [73–76]. The use of the conservative form of metric

terms and computing their derivatives using the same derivative scheme as employed for the evaluation of fluxes were found to reduce the metric evaluation errors and preserve a uniform freestream [75]. Hence, following the references, the metric terms are evaluated using

$$\begin{bmatrix} \xi_x & \xi_y & \xi_z \\ \eta_x & \eta_y & \eta_z \\ \zeta_x & \zeta_y & \zeta_z \end{bmatrix} = J \begin{bmatrix} (y_\eta z)_\zeta - (y_\zeta z)_\eta & (z_\eta x)_\zeta - (z_\zeta x)_\eta & (x_\eta y)_\zeta - (x_\zeta y)_\eta \\ (y_\zeta z)_\xi - (y_\xi z)_\zeta & (z_\zeta x)_\xi - (z_\xi x)_\zeta & (x_\zeta y)_\xi - (x_\xi y)_\zeta \\ (y_\xi z)_\eta - (y_\eta z)_\xi & (z_\xi x)_\eta - (z_\eta x)_\xi & (x_\xi y)_\eta - (x_\eta y)_\xi \end{bmatrix}, \tag{2.12}$$

where the Jacobian J is

$$J = \left| \frac{\partial(\xi, \eta, \zeta)}{\partial(x, y, z)} \right| = \left[x_\xi \left(y_\eta z_\zeta - y_\zeta z_\eta \right) - x_\eta \left(y_\xi z_\zeta - y_\zeta z_\xi \right) + x_\zeta \left(y_\xi z_\eta - y_\eta z_\xi \right) \right]^{-1}. \tag{2.13}$$

In equations 2.6, 2.7 and 2.8, the terms τ_{ij} and q_i are the resolved stress tensor and heat flux. Whereas ψ_{ij} and Q_i are the stress tensor and heat flux representing the subgrid-scales. They are given as

$$\tau_{ij} = \frac{\tilde{\mu}}{Re_{ref}} \left(2\tilde{S}_{ij} - \frac{2}{3} \tilde{S}_{kk} \delta_{ij} \right), \tag{2.14}$$

$$q_i = \frac{-\tilde{\mu}}{(\gamma - 1) M_{ref}^2 Re_{ref} Pr} \frac{\partial \widetilde{T}}{\partial x_i}, \tag{2.15}$$

$$\psi_{ij} = \bar{\rho} (\widetilde{u_i u_j} - \tilde{u}_i \tilde{u}_j), \tag{2.16}$$

$$Q_i = \bar{\rho} (\widetilde{u_i T} - \tilde{u}_i \tilde{T}). \tag{2.17}$$

In equation 2.14, $\tilde{S}_{ij}$ is the Favre-filtered strain rate tensor defined as

$$\tilde{S}_{ij} = \frac{1}{2} \left(\frac{\partial \tilde{u}_i}{\partial x_j} + \frac{\partial \tilde{u}_j}{\partial x_i} \right). \tag{2.18}$$

Sutherland's law is used to compute the dynamic viscosity,

$$\tilde{\mu} = \frac{\tilde{\mu}^*}{\mu^*_{ref}} = \widetilde{T}^{3/2} \frac{1 + S}{\widetilde{T} + S}, \tag{2.19}$$

where S is the Sutherland constant which is equal to $110K/T^*_{ref}$ and μ^*_{ref} is the reference dynamic viscosity. The Mach number, M_{ref} and the Reynolds number, Re_{ref} are given as

$$M_{ref} = \frac{U^*_{ref}}{\sqrt{\gamma R^* T^*_{ref}}}, \tag{2.20}$$

$$Re_{ref} = \frac{\rho^*_{ref} U^*_{ref} R^*_{ref}}{\mu^*_{ref}}. \tag{2.21}$$

In these expressions, the ratio of specific heat, $\gamma = 1.4$ and the specific gas constant, $R^* \approx 287 J/kg - K$. The Prandlt number, Pr in equation 2.15 is fixed to be 0.7.

As mentioned earlier, in most of the work, ILES is used. So, the SGS stress (equation 2.16) and the SGS heat flux (equation 2.17), ψ_{ij} and Q_i are set to zero.

2.2 Numerical Methods

This section describes the spatial discretization, spatial filter and additional numerical methods used in the modular-LES code for solving the system of governing equations. Additional numerical methods include the schemes used for handling cylindrical grids and time discretization. The details of the schemes are given in the following sections.

2.2.1 Spatial Discretization

The discretized governing equations are solved using finite-difference schemes. In order to capture the relevant scales that are essential for noise predictions, a high order compact finite-difference scheme has been used. The non-dissipative sixth order compact difference scheme developed by Lele [77] is used to calculate spatial derivatives at the interior grid points away from boundaries. It is given as

$$\frac{1}{3} f'_{i-1} + f'_i + \frac{1}{3} f'_{i+1} = \frac{7}{9\Delta\xi} \left(f_{i+1} - f_{i-1} \right) + \frac{1}{36\Delta\xi} \left(f_{i+2} - f_{i-2} \right), \tag{2.22}$$

where f_i' is the derivative of the quantity f at the i^{th} grid point with respect to the computational coordinate ξ. In computational space, uniform grid spacing is used. Therefore, the grid spacing in the ξ direction is set to $\Delta\xi = 1$.

For nodes at the left and right boundaries, third-order one-sided compact schemes given by

$$f_1' + 2f_2' = \frac{1}{2\Delta\xi}\left(-5f_1 + 4f_2 + f_3\right), \tag{2.23}$$

$$f_N' + 2f_{N-1}' = \frac{1}{2\Delta\xi}\left(5f_N - 4f_{N-1} - f_{N-2}\right), \tag{2.24}$$

are used. Similarly, fourth-order-central compact schemes given by

$$\frac{1}{4}f_1' + f_2' + \frac{1}{4}f_3' = \frac{3}{4\Delta\xi}\left(f_3 - f_1\right), \tag{2.25}$$

$$\frac{1}{4}f_{N-2}' + f_{N-1}' + \frac{1}{4}f_N' = \frac{3}{4\Delta\xi}\left(f_N - f_{N-2}\right), \tag{2.26}$$

are used for nodes located next to the left and right boundaries. The same discretization schemes are utilized in the other two computational coordinates η and ζ as well.

2.2.2 Spatial Filtering

Numerical instabilities could arise during the solution of the governing equations. If not suppressed, these instabilities could eventually cause the simulations to fail. Therefore, a spatial filter is used to keep the simulations stable. The sixth-order central tridiagonal spatial filter by Gatinode and Visbal [78] given by

$$\alpha_f \bar{f}_{i-1} + \bar{f}_i + \alpha_f \bar{f}_{i+1} = \sum_{n=0}^{3} \frac{a_n}{2}(f_{i+n} + f_{i-n}) \tag{2.27}$$

is used to damp out the unwanted spurious instabilities that arise from the boundary conditions, unresolved scales, and mesh non-uniformities. Additionally, the non-dissipative properties of the compact scheme used add to the growth of the instabilities. In equation 2.27, $\bar{f}$ is a filtered conservative flow variable and f is the corresponding unfiltered value. The filtering parameter α_f can take any value between

-0.5 and 0.5. The amount of damping can be controlled by adjusting α_f. Higher values of α_f make the filter less dissipative. The coefficients a_0,...,a_3 used in equation 2.27 are listed in table 2.1.

At the boundary points, no filtering operation is carried out. But, sixth-order one-sided spatial filters by Gatinode and Visbal [78] are used for the first two points away from the boundaries. Near the left boundary, the spatial filter equations at the first and second point away from the boundary are given as

$$\alpha_f \bar{f}_1 + \bar{f}_2 + \alpha_f \bar{f}_3 = \sum_{n=1}^{7} a_n f_n, \tag{2.28}$$

$$\alpha_f \bar{f}_2 + \bar{f}_3 + \alpha_f \bar{f}_4 = \sum_{n=1}^{7} a_n f_n, \tag{2.29}$$

respectively. The coefficients a_1,...,a_7 used in the above equations are also given in table 2.1. Near the right boundary, expressions analogous to equation 2.28 and equation 2.29 are used.

As mentioned earlier, in the absence of an SGS model, the spatial filter is used as an implicit SGS model to remove the unresolved turbulent scales. The spatial filter is applied after each time step. As in the previous works [45,46,49,63,64], the spatial filter parameter α_f is usually set to 0.47.

2.2.3 Additional Numerical Methods

The simulations of jets through various nozzles utilize cylindrical grids. The centerline singularity that arises by the use of cylindrical grids is handled by the radial treatment suggested by Mohseni and Colonius [79]. The radial points are shifted by a distance from the pole, thereby avoiding the singularity when computing the derivatives. The fine azimuthal grid spacing near the centerline restricts the time-step specification to a lower value due to the Courant-Friedrichs-Lewy (CFL) condition. The use of smaller time-steps increases the simulation time considerably. This issue is addressed by utilizing the point-skipping method of Bogey et al. [80]. The point-

Table 2.1. Sixth-order spatial filter (equations 2.27, 2.28 and 2.29) coefficients.

Equation	a_0	a_1	a_2	a_3	a_4	a_5	a_6	a_7
2.27	$\frac{11}{16}+\frac{5\,\alpha_f}{8}$	$\frac{15}{32}+\frac{17\,\alpha_f}{16}$	$\frac{-3}{16}+\frac{3\,\alpha_f}{8}$	$\frac{1}{32}-\frac{\alpha_f}{16}$				
2.28		$\frac{1}{64}+\frac{31\,\alpha_f}{32}$	$\frac{29}{32}+\frac{3\,\alpha_f}{16}$	$\frac{15}{64}+\frac{17\,\alpha_f}{32}$	$\frac{-5}{16}+\frac{5\,\alpha_f}{8}$	$\frac{15}{64}-\frac{15\,\alpha_f}{32}$	$\frac{-3}{32}+\frac{3\,\alpha_f}{16}$	$\frac{1}{64}-\frac{\alpha_f}{32}$
2.29		$\frac{-1}{64}+\frac{\alpha_f}{32}$	$\frac{3}{32}+\frac{13\,\alpha_f}{16}$	$\frac{49}{64}+\frac{15\,\alpha_f}{32}$	$\frac{5}{16}+\frac{3\,\alpha_f}{8}$	$\frac{-15}{64}+\frac{15\,\alpha_f}{32}$	$\frac{3}{32}-\frac{3\,\alpha_f}{16}$	$\frac{-1}{64}+\frac{\alpha_f}{32}$

skipping method coarsens the grid artificially near the centerline. The implementation details of these methods can be found in [45, 46].

For time-advancement, the four-stage fourth-order classical Runge-Kutta method is utilized. The details of the method can be found in [63].

2.3 Boundary Conditions

The governing equations given by equation 2.3 are to be supplied with additional constraints to close the system of equations. To that end, various boundary conditions are implemented into the modular LES solver. Boundary conditions are available to simulate both subsonic and supersonic flows. A brief overview of some of the boundary conditions utilized in the current work is given next. The wall-model boundary conditions are not discussed in this section and are deferred to chapter 3.

2.3.1 Inflow Boundary Condition

For turbulent flows, adequate flow conditions need to be specified at the inflow to achieve the targeted flow conditions at a reasonable cost. In physical experiments, turbulence comes from a boundary layer developing along the walls of a nozzle, flat plate, channel, etc. So, along with the mean flow data supplied at the inflow, the provided fluctuations should help in the sustenance of the turbulent state of the boundary layer. Moreover, for jet noise studies, the state of the boundary layer is crucial as it affects the shear layer developing downstream and the associated noise. One of the approaches is to use a laminar boundary layer at the inflow boundary and allow the boundary layer to naturally transition from laminar to a turbulent state. However, this approach needs extended domains to foresee the natural transition, which at high Reynolds numbers makes the simulations prohibitively expensive [81]. As a result, over the past few years, several turbulent inflow methods have been developed and applied to jet noise studies. Dhamankar et al. [82] provide a comprehensive review of several turbulent inflow methods used with the LES. Among the available turbulent

inflow methods, the recycling - rescaling - based methods and synthetic turbulence generation methods are found to be useful when it comes to problems of practical interest. However, the ability of synthetic turbulence generation methods to avoid any artificial periodicity in the flowfield and their ease of application to curvilinear grids give them an added advantage over the recycling - rescaling - based methods [16]. As a result, the digital filter-based inflow turbulent boundary condition [16, 48], which is a type of synthetic turbulence generation method, is implemented in the modular LES solver. It is based on the approach of Xie and Castro [83] and generates space and time correlated random velocity fluctuations on the fly. Xie and Castro's [83] approach is limited to uniform Cartesian meshes. The formulation was extended to handle non-uniform curvilinear grids in the modular-LES code [48].

The following information needs to be provided as an input for the digital-filter boundary condition: Reference Reynolds stress profiles, mean velocity, density, and pressure, and integral length scales (ILS) in each of the flow directions. All this information may or may not be provided in the references of the matching experiments or simulations that are intended to be performed. But, by making use of the available data from DNS, precursor RANS/LES simulations, experiments or empirical relations, the inflow conditions are specified as closely as possible with the matching experiments or simulations. The digital-filter boundary condition imposes the instantaneous density, velocity components and pressure at the inflow during the runtime of the simulation. The velocity and density fluctuations are computed and added to their mean at each sub-step of the time advancement scheme. The density fluctuations are determined based on the suggestions of Touber and Sandham [84]. No pressure fluctuations are imposed, and only a mean pressure is specified.

The use of digital-filter inflow boundary conditions, however, requires a redevelopment region [16, 82]. It was found from the simulations of high Reynolds number boundary layers that a redevelopment region of approximately 11.5 boundary layer thickness is necessary for the artificial turbulence introduced at the inflow to become realistic. In addition, a sponge zone is placed near the inflow to dampen the spurious

noise that arises due to the specification of a constant mean pressure at the inlet, which acts as a reflecting surface and causes small pressure waves to propagate in the downstream direction polluting the acoustic field.

2.3.2 Radiation and Outflow Boundary Conditions

As the computational domain extents used in the simulations are restricted due to the operational costs involved, the turbulent structures evolved during the flow simulation reach the end of the domain. These structures when exiting the domain create disturbances and contaminate the solution if not treated properly. So, the boundary condition should be robust enough to let these structures out of the domain without any numerical reflections. Therefore, the mean flow based 2-D non-reflecting farfield boundary conditions of Tam and Dong [85] generalized to 3-D by Bogey and Bailly [86] are utilized in some of the simulations performed in the current work. Two different boundary conditions were formulated to handle different type of disturbances reaching the boundary. For boundaries where only acoustic disturbances are present, radiation boundary conditions are used. But in the mean flow direction, both acoustic and aerodynamic disturbances reach the boundary. Such boundaries are treated using outflow boundary conditions. These formulations rely on the local mean flow variables, and an acoustic source position needs to be specified. The location of the acoustic source is usually assumed to be near the end of the potential core. The complete formulation details can be found in the original references [85, 86].

Even with the use of non reflecting outflow boundary conditions, when strong vortices are present in the flowfield, they need to be dampened out before they reach the outflow boundary to avoid spurious reflections and numerical instabilities, which if not treated may cause the simulations to fail. The simulations used a sponge zone which prevents the simulation from failing. The sponge zone formulation by Colonius et al. [87] is prescribed near the outflow boundary for reducing the amplitude of the vortices before they reach the outflow boundary. The sponge zone provides

artificial damping by forcing the local turbulent flowfield towards a smooth target solution. The jet flow simulations usually use the self-similar solution of an isothermal incompressible round jet [3] as the target solution. Implementation details of the sponge zone formulation are given in reference [45].

The characteristic-based outflow boundary condition [88, 89] based on an inviscid formulation is used in the converging-diverging channel flow simulations performed as part of the current work. The characteristic-based outflow boundary condition without the specification of a sponge zone near the outflow boundary was found to be more stable than the Tam and Dong outflow boundary condition with a sponge zone.

2.3.3 Other Boundary Conditions

Apart from the inflow, outflow and radiation boundary conditions, periodic boundary conditions are also used in both rotational and translational directions and used depending on the problem type. The details can be found in references [48, 90]. Periodicity can be either due to the flow-field or geometry. Cylindrical grids that are usually utilized for the nozzle flow simulations require the specification of rotational periodic boundary conditions in the azimuthal direction. Here, periodicity is due to the geometry. When dealing with flows involving channels or flat plate boundary layers, simulations which include the effect of side walls as in the experiments are expensive because of the need of a larger domain. However, translational periodic boundary conditions are used in the current work, which helps in constraining the domain extent in the spanwise direction along which flow can be assumed to be repeating. But, the domain should be sufficiently large enough to accommodate the largest scales present in the flow. The domain lengths are chosen based on *a priori* knowledge of the simulation in consideration. Periodic boundary conditions also help in avoiding the use of one-sided schemes near the boundaries where they are applied.

Same numerical schemes applied for the interior points can be used across the periodic boundaries.

Additionally, adiabatic viscous wall boundary condition [48] and edge boundary condition [48] are also used in the current work.

2.4 Subgrid-Scale Modeling

SGS modeling is used to model the flow physics of the unresolved scales in an LES. In turbulent flows, the turbulence energy dissipates at the smaller unresolved scales. Numerical issues could arise if the energy is not appropriately removed from the flow. So, an appropriate SGS model needs to be chosen, which can incorporate this kind of physical mechanism into the governing equations. With the primary focus of the modular-LES code being to perform jet flow simulations for noise computation, the use of SGS models has been found to be too dissipative [63, 71]. But with the coarser grids utilized in wall-modeled LES, it is essential to model the effects of small-scale motions more appropriately. So, Aikens [45] incorporated the dynamic Smagorinsky model (DSM) into the modular LES code. DSM utilizes the instantaneous flow data and computes the model coefficients in the eddy viscosity formulation dynamically. It has the potential to adjust the eddy viscosity in the wall-normal direction for various grid resolutions and flow regimes. The DSM method is based on the works of Moin et al. [66] and Lilly [91].

In DSM, the SGS stress (equation 2.16) and SGS heat flux (equation 2.17) which are set to zero when utilizing ILES, are now modeled as

$$\Psi_{ij} \approx \Psi_{ij} - \frac{1}{3}\Psi_{kk}\delta_{ij} = -2\overline{\rho}C_S\Delta^2\widetilde{S}_M\left(\widetilde{S}_{ij} - \frac{1}{3}\widetilde{S}_{kk}\delta_{ij}\right), \tag{2.30}$$

$$Q_i = -\frac{\overline{\rho}C_S\Delta^2\widetilde{S}_M}{Pr_t(\gamma-1)M_{ref}^2}\frac{\partial\widetilde{T}}{\partial x_i}, \tag{2.31}$$

respectively. The strain rate tensor, $\tilde{S_{ij}}$ in equation 2.30 is given by equation 2.18. Since the flows in which the DSM formulation is tested in the current work are nearly incompressible, the trace in equation 2.30 is neglected. In equation 2.17, M_{ref} is

the reference Mach number, $\widetilde{T}$ is the Favre-filtered temperature and the turbulent Prandtl number, Pr_t is set to 0.7. In equations 2.30 and 2.31, $\widetilde{S}_M$ is given as

$$\widetilde{S}_M = \sqrt{2\widetilde{S}_{lm}\widetilde{S}_{lm}}, \tag{2.32}$$

and C_S is the Smagorinsky coefficient given as

$$C_S = \frac{(L_{ij} - \frac{1}{3}L_{kk}\delta_{ij})M_{ij}}{M_{kl}M_{kl}}, \tag{2.33}$$

where

$$L_{ij} = \frac{\widehat{\overline{\rho u_i}}\,\widehat{\overline{\rho u_j}}}{\overline{\rho}} - \frac{\widehat{\overline{\rho u_i}}\,\widehat{\overline{\rho u_j}}}{\widehat{\overline{\rho}}}, \tag{2.34}$$

$$M_{ij} = \alpha_{ij} - \widehat{\beta_{ij}}, \tag{2.35}$$

and

$$\alpha_{ij} = -2\hat{\Delta}^2\widehat{\widetilde{S}}_M\widehat{\overline{\rho}}\left(\widehat{\widetilde{S}}_{ij} - \frac{1}{3}\widehat{\widetilde{S}}_{kk}\delta_{ij}\right), \tag{2.36}$$

$$\beta_{ij} = -2\Delta^2\widetilde{S}_M\overline{\rho}\left(\widetilde{S}_{ij} - \frac{1}{3}\widetilde{S}_{kk}\delta_{ij}\right). \tag{2.37}$$

Here, Δ is the local grid spacing computed using $(1/J)^{1/3}$ and the test filter scale is given as $\hat{\Delta} = 2\Delta$. The resolved solution is filtered using a second-order trapezoidal based method, given as

$$\hat{f}_i = \frac{1}{4}\left(f_{i+1} + 2f_i + f_{i-1}\right), \tag{2.38}$$

where f is any generic variable and the filtered terms in equations 2.37 to 2.37 are represented using $\widehat{\ }$.

2.5 Parallelization Strategy

The truncated SPIKE algorithm [92] is used to solve the tridiagonal linear systems associated with spatial derivatives and filtering as shown in equations 2.22 and 2.27, respectively. Complete details of the implementation can be found in references [93, 94]. It is an efficient parallel tridiagonal system solver for solving diagonally dominant systems. A nearly ideal scalability on up to 91,125 cores [46] has

been achieved with the current LES code using this algorithm. Such good efficiency is obtained by depending more on local communication between the cores. Network congestion is reduced by avoiding global communication. A multiblock topology has been used to take advantage of the SPIKE solver. A given computational domain can be decomposed into one or more subsets known as "superblocks". Each superblock is further divided into smaller blocks which are mapped to a core/processor during runtime. For each superblock, only one boundary condition is specified on each of its six faces. The use of superblocks helps in reducing the simulation setup time, file I/O, and network congestion, which might otherwise be an issue if the current process were block based.

2.6 Acoustic Methodology

This section gives a brief description of the surface integral acoustic method used for the computation of farfield noise and its numerical implementation. In the current jet noise simulations, the porous Ffowcs Williams-Hawkings (FWH) [7] method is used to project the nonlinear near-field noise sources to the farfield. The nonlinear near-field noise sources are predicted by the LES and instantaneous flowfield data are stored on a control surface, or acoustic data surface (ADS), that surrounds the nonlinear field. The FWH method is a viable choice due to its advantages and robustness over other methods such as Kirchhoff's, rigid body Ffowcs Williams-Hawkings and more traditional Lighthill's acoustic analogy [5]. Although both the Kirchhoff's and FWH methods require only computation of surface integrals for the noise projection from the ADS, Kirchhoff's approach is very sensitive to the placement of the ADS making it less effective than the FWH method. Methods like rigid body Ffowcs Williams-Hawkings and Lighthill's acoustic analogy require computation of volume integrals and second derivatives for the evaluation of acoustic sources present in the flowfield, making them more difficult and expensive than the FWH method. The FWH formulation details are presented next.

2.6.1 The porus Ffowcs Williams-Hawkings Method

The pressure disturbance, $p'(\vec{x},t)$, at the far field can be computed using the FWH formulation [5, 7] as

$$p'(\vec{x},t) = p'_T(\vec{x},t) + p'_L(\vec{x},t) + p'_Q(\vec{x},t), \tag{2.39}$$

in which p'_T, p'_L and p'_Q are the thickness, loading and quadrupole noises respectively. The coordinates $(\vec{x},t)$ are the observer location and time. Here, the values of the pressure terms are relative to the ambient pressure, p_∞. The thickness and loading noises, p'_T and p'_L are given as

$$4\pi p'_T(\vec{x},t) = \int_S \left[\frac{\rho_\infty \dot{U}_n}{r}\right]_{ret} dS, \tag{2.40}$$

$$4\pi p'_L(\vec{x},t) = \frac{1}{c_\infty}\int_S \left[\frac{\dot{L}_r}{r}\right]_{ret} dS + \int_S \left[\frac{L_r}{r^2}\right]_{ret} dS, \tag{2.41}$$

respectively, where

$$U_i = \frac{\rho u_i}{\rho_\infty}, \tag{2.42}$$

$$L_i = (p - p_\infty)\delta_{ij} n_j + \rho u_i u_n. \tag{2.43}$$

In the above expressions, the subscripts r and n represent the dot product of the vector with the unit vector in the radiation and normal directions respectively. The ambient conditions are represented by ∞. The dot on top of the variables in equations 2.40 and 2.41 represent the time derivative. The surface integrals for the computation of thickness and loading noise pressure are carried out using a second order mid-panel surface quadrature method coupled with quadratic interpolation of the integrand to retarded times (subscript ret), $\tau = t - r/c_\infty$. Here, r is the distance from the source on the surface to the observer and c_∞ is the ambient speed of sound.

The computation of the quadrupole noise pressure, p'_Q, requires a volume integral from the ADS to the farfield location and is neglected due to the costs involved, which is compensated for by choosing the ADS such that it encloses all of the sound-producing regions of the flowfield. The complete details of the FWH implementation can be found in reference [46].

2.6.2 End-Cap Treatment

In jet noise simulations, while performing the surface integration using FWH, closing the FWH surfaces with a downstream ADS (end-cap) has been a debatable question [4]. Vortices passing through the end-cap can lead to spurious predictions of noise at upstream observer angles, affecting a wide range of frequencies. Excluding an end-cap, however, can introduce high-magnitude spurious noise at low frequencies [95,96]. Different treatments with and without use of end-cap, end-cap averaging [95] and the end-cap formulation by Ikeda et al. [97, 98] were tested using the modular LES code by Aikens [45] and Aikens et al. [52]. These studies showed the use of end-cap averaging and the end-cap formulation by Ikeda et al. mitigate some of the spurious effects that are associated with and without the use of an end-cap. But unlike the end-cap averaging method, which requires multiple end-caps over which data is to be collected, data need to be collected only on one end-cap surface when using Ikeda's method. This helps in reducing the file Input/Output (I/O) as the instantaneous flowfield data need to be sampled and stored after every few time-steps. Additionally, Ikeda's method was also found to be insensitive to the placement of the end-cap. Due to these reasons, Ikeda's method is used in the computation of acoustics in the current work.

Ikeda's method [97–99] modifies the FWH formulation and proposes an alternative to the quadrupole noise pressure, p'_Q. Including the contributions of the quadrupole term dampen the spurious noise that usually arises when turbulent motions pass through the end-cap. However, due to the expensive volumetric integrals involved with it, the quadrupole term is usually neglected in jet noise studies. Based on the assumption that the vortices passing through the end-cap decay very slowly (frozen turbulence), and without producing any noise, a surface integral equivalent to the volumetric integral of p'_Q is formulated by Ikeda et al. [97, 98]. It is given as

$$p'_Q = \frac{1}{4\pi c_\infty^2} \int_S \left[\frac{1}{|1 - M_r^d|} \frac{\dot{T}_{ij} \hat{r}_i \hat{r}_j}{r|1 - M_r|^2} \right]_{ret} \left(\vec{U_c} \cdot \hat{n} \right) dS, \tag{2.44}$$

where

$$\dot{T}_{ij} = \frac{\partial}{\partial t}\left[\rho(u_i - U_i)(u_j - U_j) + \left((p - p_\infty) - c_\infty^2(\rho - \rho_\infty)\right)\delta_{ij}\right]. \tag{2.45}$$

In the above expressions, M_r and M_r^d are the Mach numbers associated with the freestream velocity, $\vec{U}_\infty$ and deficit velocity $\vec{U}_d$ respectively. The deficit velocity is defined as $\vec{U}_d = \vec{U}_c - \vec{U}_\infty$, where $\vec{U}_c$ is the eddy convection velocity. c_∞ is the ambient speed of sound and $\hat{r}$ is the radial unit vector. As the simulations performed here do not involve forward flight, the freestream velocity can be neglected and equation 2.44 is simplified further as

$$p'_Q = \frac{1}{4\pi c_\infty^2}\int_S \left[\frac{\dot{T}_{ij}\hat{r}_i\hat{r}_j}{r|1 - \vec{U}_c \cdot \hat{r}/c_\infty|}\right]_{ret} \left(\vec{U}_c \cdot \hat{n}\right) dS. \tag{2.46}$$

The complete formulation details can be found in references [97–99] and the implementation details can be found in reference [45].

2.6.3 Noise Computation

Depending on the range of frequencies over which the noise is to be computed, N samples of the flow data are collected on the ADS after every few timesteps, Δt_{record}. The length of the record sample is then $T_{record} = N * \Delta t_{record}$. Using N and Δt_{record}, the lower and upper frequency bounds in terms nondimensional Strouhal number are given as

$$St_{min} = \frac{2}{N\Delta t_{record}}, \tag{2.47}$$

$$St_{max} = \frac{1}{\Delta t_{record}}, \tag{2.48}$$

respectively. The Strouhal number in terms of dimensional quantities for nozzle flows is represented as

$$St = \frac{f^* D_j^*}{U_j^*}, \tag{2.49}$$

where f^* is the frequency, D_j^* and U_j^* are the diameter and velocity at the nozzle exit.

The following approach is followed to compute the sound pressure levels at the observer locations. First, using the FWH method, the pressure history is computed at

the farfield observer locations. Either the entire pressure history is used to compute the spectra, or the acoustic pressure signal is split into multiple records to average the spectra. The mean of each record is computed and subtracted from the acoustic pressure signal. A windowing function similar to Freund [100] is used and multiplied with the pressure history. The pressure history in the time domain is then converted into the frequency domain using a Fast Fourier Transform (FFT). The $1/3^{rd}$ Octave band is usually used for reporting. Therefore, the narrowband spectra obtained using the FFT are binned to compute $1/3^{rd}$ Octave band spectra between the cutoff frequencies which are determined by St_{min} and St_{max}. But, it should also be noted that grid resolution dictates the maximum Strouhal number that can be resolved. This cutoff Strouhal number, $St_{g,max}$, can be approximated using [45]

$$St_{g,max} \approx \frac{2}{N\Delta M_j}\sqrt{\frac{T_\infty}{T_j}} \tag{2.50}$$

where N is the minimum number of grid intervals required for resolving a given wavelength, Δ is the maximum of the grid space size in the radial and axial directions near the FWH surface, M_j and T_j are the Mach number and temperature at the jet exit respectively, and T_∞ is the ambient temperature. The quantity N is dependent on the underlying numerical scheme utilized in the simulations. For the sixth-order compact finite-difference scheme used here, its value is between 4 and 6. [75]. Finally, the overall sound pressure level (OASPL) is computed at an observer location by integrating the spectra over the individual frequencies at a given observer location. In jet noise studies, it is a usual practice to compute the spectra at multiple azimuthal locations and average it, which is also followed in the noise computations of the current simulations.

3. WALL MODELS

This chapter describes the various wall-model boundary conditions used in the current work. Both the formulation and implementations details are provided. The main purpose of a wall-model is to approximate the near wall flow physics without actually resolving the near-wall region. A multi-step approach is used in which the wall-model first takes the information from the outer LES and approximates the shear stress and heat flux required for the calculation of fluxes to be specified at the wall. Finally, these fluxes are used as boundary conditions during the time-advancement of the Navier-Stokes equations. This process is illustrated in figure 3.1. The use of wall-models will prevent the incorrect computation of shear stress and heat flux that could arise since the slope of the velocity profile is not computed correctly when coarse grids are used in the simulation of high Reynolds number flows.

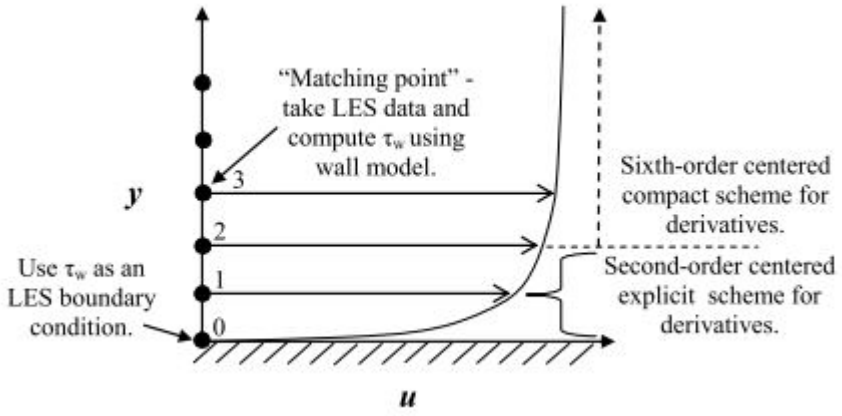

Figure 3.1. Depiction of the Wall Model [45]

Given the above advantage of using a wall-model, Aikens [45] implemented an equilibrium wall-model into the modular-LES solver. The formulation details of the equilibrium wall-model are presented in section 3.1. It is followed by the formulation

details of three new wall-models that are implemented as part of this work. They are the generalized equilibrium wall-model of Spalding [29], generalized non-equilibrium wall model by Shih [33, 60] and integral wall-model of Yang et al. [61]. The details of the new wall-models are given in subsequent sections starting from 3.2. Finally, the implementation details of the wall-models in the modular-LES code are presented in section 3.5.

3.1 Equilibrium Wall Model

The equilibrium stress wall-model (EWM) utilizes the log-law [3], which is valid outside the viscous sublayer ($30 < y^+ < 0.3\delta^+$), to model the turbulent fluxes between the no-slip solid wall and the matching point (MP), as shown in figure 3.1. The matching point is the grid point located above the wall where the LES resolves the flow. The wall-model utilizes the flow data from the matching point as an input. The log-law for an incompressible turbulent boundary layer is

$$u^+ = \frac{1}{\kappa}\log\left(y^+\right) + B, \tag{3.1}$$

where u^+ and y^+ are given as

$$u^+ = \frac{U_{||}}{u_\tau}, \tag{3.2}$$

$$y^+ = \frac{y u_\tau \rho}{\mu} Re_{ref}, \tag{3.3}$$

where $U_{||}$ is the wall-parallel velocity, ρ is the density, Re_{ref} is the Reynolds number based on the quantities at the chosen reference location of a simulation, μ is the dynamic viscosity, u_τ is the unknown friction velocity that is appropriate in the near-wall region, $\kappa = 0.41$ and $B = 5$. $U_{||}$, ρ and μ in equations 3.2 and 3.3 are obtained from the LES solution at the chosen matching point location. The matching point is usually chosen such that its height is between $50 < y^+ < 0.1\delta^+$. Kawai and Larsson [21] suggest this range for use in equilibrium stress wall-models. In the expression, δ^+ is the local boundary layer thickness in wall units. It should be noted

that the nondimensional units of y^+ are referred to as wall units. Newton's method is used iteratively to solve equation 3.1 for u_τ.

3.2 Generalized Equilibrium Wall Model

As described earlier, the EWM which relies on the standard log-law needs the placement of the first grid point from the wall to be in a range of $50 < y^+ < 0.1\delta^+$. It is challenging to design grids that satisfy this condition over the entire length of the flow domain. Not meeting this criterion results in the computation of incorrect wall shear stresses. The local refinement of the grid in the wall-normal direction is also restricted due to the requirement to place the first grid point in the prescribed range. To overcome this shortcoming, Spalding [29] proposed a model which is valid in the viscous sublayer, buffer layer and log-law region of an equilibrium boundary layer. The advantage of using such a unified profile is that the grid point from which the LES data are sampled can be located anywhere within or below the log-law region. Spalding's law is given by

$$y^+ = u^+ + \exp(-\kappa B)\left[\exp(\kappa u^+) - 1 - \kappa u^+ - \frac{(\kappa u^+)^2}{2} - \frac{(\kappa u^+)^3}{6}\right], \tag{3.4}$$

Nondimensionalizing equation 3.4 with respect to the chosen reference variables (denoted using a subscript "ref") produces

$$\left(\frac{\rho u_\tau y}{\mu} Re_{ref}\right) = \frac{U_{||}}{u_\tau} + \exp(-\kappa B)\left[\exp(\kappa\frac{U_{||}}{u_\tau}) - 1 - \kappa\frac{U_{||}}{u_\tau} - \frac{1}{2}\left(\kappa\frac{U_{||}}{u_\tau}\right)^2 - \frac{1}{6}\left(\kappa\frac{U_{||}}{u_\tau}\right)^3\right]. \tag{3.5}$$

For a time-averaged flowfield, this equation is approximately satisfied for $y^+ < 0.3\delta^+$ [3]. Unlike the EWM, the current wall model methodology is still valid if used in a range for $y^+ < 50$. The equation 3.5 can be solved using Newton's method to obtain the wall shear stress by making use of the parameters at the matching point. The advantage of such a model is the flexibility in designing a grid without having any restriction in the placement of the matching point location. This model will be referred to as GEWM hereafter.

3.3 Generalized Non-Equilibrium Wall Model

The generalized non-equilibrium wall model (GNEWM) developed by Shih et al. [33, 60] is described in this section. Equilibrium stress models like EWM and GEWM have been applied to a variety of flows, despite them being valid only for turbulent boundary layers. But flows encountered in engineering applications, such as the nozzle flows simulated in the current jet noise studies could re-laminarize. This leads to the deviation of a boundary layer from turbulent state, where the equilibrium stress models are not applicable. The GNEWM is formulated such that it accounts for the effects of pressure gradient by utilizing an asymptotic solution given by Tennekes and Lumley [101] for turbulent boundary layers with strong adverse pressure gradients and zero wall stress. It also uses the standard log-law in the log-law region. The use of the two scaling laws makes the GNEWM valid for flows involving non-zero pressure gradient turbulent boundary layers, making it applicable to complex wall-bounded flows with acceleration, deceleration, and recirculation.

The GNEWM formulation is based on the multivariate asymptotic technique of Tennekes [102] in which the flowfield is decomposed into two parts. The first part is dependent on the wall shear stress, whereas the second part of the decomposition is dependent on the pressure gradient. Following the decomposition, the wall parallel velocity, $U_{||}$, at the matching point location can be decomposed into two parts, U_1 and U_2. The friction velocity u_τ characterizes the first part and can be computed using GEWM given by equation 3.4 as

$$y_\tau^+ = U_1^+ + \exp(-\kappa B)\left[\exp(\kappa U_1^+) - 1 - \kappa U_1^+ - \frac{(\kappa U_1^+)^2}{2} - \frac{(\kappa U_1^+)^3}{6}\right], \tag{3.6}$$

where

$$y_\tau^+ = \frac{\rho u_\tau y}{\mu} Re_{ref}, \tag{3.7}$$

$$U_1^+ = \frac{U_1}{u_\tau}. \tag{3.8}$$

Similarly, the second part can be characterized using the velocity scale u_p, which is defined by the wall tangential pressure gradient as

$$u_p = \left[\frac{\mu}{\rho^2}\left|\frac{dp_w}{dx}\right|\frac{1}{Re_{ref}}\right]^{1/3}. \tag{3.9}$$

Using u_p and the asymptotic solution of Tennekes and Lumley [101] for flows with large adverse pressure gradients and zero wall stress, U_2 can be calculated. In inertial sublayer of a boundary layer, the turbulent stresses dominate the viscous stress. The nondimensional form of the asymptotic solution of Tennekes and Lumley [101] in the inertial sublayer is given as

$$u_2^+ = \alpha \ln\left(y_p^+\right) + \beta, \tag{3.10}$$

in which $\alpha = 5$, $\beta = 8$. As with the GEWM, an analytical expression that is valid in all the wall regions of flows with zero-wall stress is formulated by Shih et al. [60] based on equation 3.10. It is

$$(y_p^+)^2 = U_2^+ + \exp\left(\frac{-2\beta}{\alpha}\right)\left[\exp\left(\frac{U_2^+}{\alpha}\right) - 1 - \frac{U_2^+}{\alpha}\right]. \tag{3.11}$$

In equation 3.11, y_p^+ and U_2^+ are given as

$$y_p^+ = \frac{u_p y \rho}{\mu} Re_{ref}, \tag{3.12}$$

$$U_2^+ = 2\frac{|dp_w/dx|}{dp_w/dx}\frac{U_2}{u_p}. \tag{3.13}$$

The scaling laws given by equations 3.6 and 3.11 are blended as

$$\frac{U_{||}}{u_c} = \frac{u_\tau}{u_c}\frac{U_1}{u_\tau} + \frac{\mu}{\rho^2}\frac{1}{Re_{ref}}\frac{\partial p_w/\partial x}{u_c^3}\frac{U_2}{u_c}, \tag{3.14}$$

where u_c is a hybrid velocity scale defined as

$$u_c = u_\tau + u_p. \tag{3.15}$$

In the original implementation by Shih et al. [33], curve fits of the form $f(y_\tau^+)$ and $f(y_p^+)$ were obtained from the scaling equations 3.6 and 3.11 to form a single analytical inverse equation that can be used as a wall model. But here, the following equation

$$\frac{U_{||}}{u_c} = \frac{u_\tau}{u_c}\frac{U_1}{u_\tau} + \frac{\mu}{\rho^2}\frac{1}{Re_{ref}}\frac{\partial p_w/\partial x}{u_c^3} f(y_c^+) \tag{3.16}$$

is solved numerically using Newton's method along with equation 3.6 to compute u_c. In equation 3.16, y_c^+ is given by

$$y_c^+ = \frac{u_c y \rho}{\mu} Re_{ref}, \tag{3.17}$$

and the curve fit of $f(y_c^+)$ is defined as

$$f\left(y_c^+\right) = \begin{cases} a_2 \left(y_c^+\right)^2 + a_3 \left(y_c^+\right)^3 & y_c^+ < 4; \\ b_0 + b_1 y_c^+ + b_2 \left(y_c^+\right)^2 + b_3 \left(y_c^+\right)^3 + b_4 \left(y_c^+\right)^4 & 4 \leq y_c^+ < 15; \\ c_0 + c_1 y_c^+ + c_2 \left(y_c^+\right)^2 + c_3 \left(y_c^+\right)^3 + c_4 \left(y_c^+\right)^4 & 15 \leq y_c^+ \leq 30; \\ \alpha \ln\left(y_c^+\right) + B & y_c^+ > 30. \end{cases} \tag{3.18}$$

Table 3.1. The coefficients in $f\left(y_c^+\right)$

a_2	a_3			
0.50000	-0.00731			
b_0	b_1	b_2	b_3	b_4
-15.13800	8.46880	-0.81776	0.37292E-1	-0.63866E-4
c_0	c_1	c_2	c_3	c_4
11.92500	0.93400	-0.27805E-2	0.46262E-3	-0.31442E-5

The coefficients in $f(y_c^+)$ are given in table 3.1. Finally, u_τ can be obtained using equation 3.15, which is used to calculate the wall shear stress accounting for a pressure gradient.

3.4 Integral Wall Model

The last wall model implemented as part of the current work is the integral wall model (IWM). It was developed by Yang et al. [61]. The IWM is both as economical as an equilibrium stress wall-model and at the same time has the capability of capturing

non-equilibrium effects. Unlike the GNEWM which relies on an empirical relation to account for pressure gradient effects, the IWM is based on the classical integral method of von Karman and Pohlhausen (VKP) [103] and accounts for inertial and pressure gradient effects. The momentum integral required for VKP is obtained by vertical integration of the boundary layer momentum equation. VKP utilizes a parameterized velocity profile which satisfies the momentum integral along with some boundary conditions to determine the properties of a boundary layer. The formulation by Yang et al. [61] models the effects of surface roughness as well. But in the current implementation, surface roughness is not accounted for, as the nozzles used in jet noise cases have relatively smooth walls. The IWM formulation used in the current work is presented below.

The IWM assumes a parameterized velocity profile that contains both the viscous sub-layer and a modified version of the log-law. An additional linear term is added to the log-law which accounts for non-equilibrium effects. The assumed profile is

$$U_{||} = \begin{cases} \frac{u_\tau y}{\delta_\nu} Re_{ref}, & 0 \leq y \leq \delta_i, \\ u_\tau \left[C + \frac{1}{\kappa} \ln \frac{y}{\Delta_y} \right] + u_\tau A \frac{y}{\Delta_y}, & \delta_i < y \leq \Delta_y, \end{cases} \tag{3.19}$$

where δ_i is the height of the viscous sub-layer, Δ_y is the height of the matching point, δ_ν is the length scale associated with the inner layer. C is the log-law coefficient and A represents the contribution of non-equilibrium effects. Five unknowns describe the assumed velocity profile that ought to be determined from the local flow conditions at the matching point location. The unknowns are δ_i, δ_ν, C, A and u_τ. The momentum integral along with four other consistency conditions form a system of coupled algebraic expressions that are solved using Newton's method to determine the unknowns. The five relations are the following:

1. At the matching point height ($y = \Delta_y$), the second condition in equation 3.19 reduces to

$$u_\tau (C + A) = U_{||}. \tag{3.20}$$

2. The velocity profiles in equation 3.19 are equated at δ_i to enforce continuity between them, i.e.,

$$\frac{\delta_i}{\delta_\nu} = \left[C + \frac{1}{\kappa} \ln \frac{\delta_i}{\Delta_y} + A \frac{\delta_i}{\Delta_y} \right]. \tag{3.21}$$

Using equation 3.20, equation 3.21 can be rearranged as

$$A = \left(\frac{U_{||}}{u_\tau} + \frac{1}{\kappa} \ln \frac{\delta_i}{\Delta_y} - \frac{\delta_i}{\delta_v} \right) \left(1 - \frac{\delta_i}{\Delta_y} \right)^{-1}. \tag{3.22}$$

3. The scale separating the two layers is defined as

$$\delta_i = \min \left[11 \frac{\mu}{\rho u_\tau} \frac{1}{Re_{ref}},\ \Delta_y \right], \tag{3.23}$$

where the first term on the right-hand side is the intercept between the linear profile and log-law profile.

4. The inner layer length scale δ_ν, is defined as

$$\delta_\nu = \frac{\mu}{\rho u_\tau} \frac{1}{Re_{ref}}. \tag{3.24}$$

5. Finally, to close the system of equations, using the parameterized velocity profile given by equation 3.19, the vertically integrated momentum equation is used. It is provided as

$$\frac{\partial L_x}{\partial t} + M_x = \tau_{\Delta y} - \tau_w, \tag{3.25}$$

where L_x and M_x contain the vertically integrated convective and pressure gradient terms. The term M_x is defined as

$$M_x = \frac{1}{\rho} \frac{\partial p_w}{\partial x} \Delta_y + \left[\frac{\partial L_{xx}}{\partial x} - U_{||} \frac{\partial L_x}{\partial x} \right]. \tag{3.26}$$

The expressions for L_x and L_{xx} are

$$L_x = \int_0^{\Delta y} U_{||} dy, \tag{3.27}$$

$$L_{xx} = \int_0^{\Delta y} U_{||}^2 dy. \tag{3.28}$$

The above integrals can be expanded using the parameterized velocity profile as

$$L_x = \frac{1}{2}u_\tau \frac{\delta_i^2}{\delta_\nu} + u_\tau \Delta_y \left[\frac{1}{2}A\left(1-\frac{\delta_i^2}{\Delta_y^2}\right) + C\left(1-\frac{\delta_i}{\Delta_y}\right) - \frac{1}{\kappa}\left(1-\frac{\delta_i}{\Delta_y}+\frac{\delta_i}{\Delta_y}\ln\frac{\delta_i}{\Delta_y}\right)\right], \tag{3.29}$$

$$L_{xx} = \frac{1}{3}u_\tau^2 \frac{\delta_i^3}{\delta_\nu^2} + u_\tau^2 \Delta_y \left[\left(C-\frac{1}{\kappa}\right)^2 - \frac{\delta_i}{\Delta y}\left(C-\frac{1}{\kappa}+\frac{1}{\kappa}\ln\frac{\delta_i}{\Delta_y}\right)^2 + \frac{1}{\kappa^2}\left(1-\frac{\delta_i}{\Delta_y}\right)\right] + u_\tau^2 \Delta_y \left[A\left(C-\frac{1}{2\kappa}\right)\left(1-\frac{\delta_i^2}{\Delta_y^2}\right) - \frac{A}{\kappa}\frac{\delta_i^2}{\Delta_y^2}\ln\frac{\delta_i}{\Delta_y} + \frac{1}{3}A^2\left(1-\frac{\delta_i^3}{\Delta_y^3}\right)\right]. \tag{3.30}$$

In equation 3.26, the momentum loss due to the shear stress at the matching point is given using

$$\tau_{\Delta y} = \frac{1}{Re_{ref}}(\mu/\rho + \nu_T|_{y=\Delta y})\left.\frac{\partial U_{||}}{\partial y}\right|_{y=\Delta y}, \tag{3.31}$$

where $\nu_T|_{y=\Delta y}$ is the eddy viscosity at the matching point, defined using the classical mixing-length formulation as

$$\nu_T|_{y=\Delta y} = Re_{ref} l_m^2 \left|\left.\frac{\partial U_{||}}{\partial y}\right|_{y=\Delta y}\right|, \tag{3.32}$$

where the mixing length parameter, $l_m = \kappa y$ for $y > \delta_i$. The derivative of the parameterized velocity in equations 3.31 and 3.32 is

$$\left.\frac{\partial U_{||}}{\partial y}\right|_{y=\Delta_y} = \begin{cases} \frac{u_\tau}{\delta_\nu} Re_{ref}, & 0 \le y \le \delta_i, \\ \left(\frac{1}{\kappa}+A\right)\frac{u_\tau}{\Delta_y}, & \delta_i < y \le \Delta_y. \end{cases} \tag{3.33}$$

Forward Euler differentiation is used to find the time-derivative of L_x in equation 3.25. Equation 3.25 is then written as

$$L_x^n = \delta t\left(-M_x^{n-1} + \tau_{\Delta y}^{n-1} - \tau_w^{n-1}\right) + L_x^{n-1}, \tag{3.34}$$

where n represents the current time-step and δt is the time-step size used during the time advancement of the above equation. Since the time-advancement scheme of the LES consists of four stages, only one-fourth of the actual LES time-step size is used while taking the time derivative of the L_x term. Similarly to Yang et al. [61], the flow variables at the matching point are time-filtered using a one-sided exponential filter before being used in the IWM. For example, the wall-parallel velocity, $U_{||}$ is filtered as

$$U_{||}(t) = \epsilon u_{||}(t - \delta t) + (1 - \epsilon)U_{||}(t - \delta t), \tag{3.35}$$

where $U_{||}(t)$ is the time-filtered velocity and $u_{||}(t-\delta_t)$ is the instantaneous wall parallel velocity at the previous time-step. Similarly, other flow variables are also time-filtered. The parameter ϵ in equation 3.35 is

$$\epsilon = \frac{\delta t}{T_{wall}} \tag{3.36}$$

where T_{wall} is the diffusion time-scale of the fluctuations to traverse between the wall and the matching point. It is given as

$$T_{wall} = \frac{\Delta_y}{\kappa u_\tau} \tag{3.37}$$

The time-filtering is done for stability purposes as the IWM formulation which relies on the RANS equations can only model the slowest time-scales. The time-filtered variables are then used to determine the five unknowns in the IWM and compute the wall shear stress. Before solving the system of equations using the IWM, δ_i is computed using equation 3.23. If $\delta_i = \Delta_y$, then the IWM formulation is switched just to solve for the linear profile which is valid in the viscous sub-layer. The complete formulation details of the IWM can be found in Yang et al. [61] for further reference.

3.5 Implementation of the Wall-Models in the Modular-LES Code

So far in this chapter, the wall-model formulations have been discussed. This section presents the implementation procedure of the wall-models in the modular-LES code. The wall-models described so far in the above sections are only valid for

incompressible flows. To extend the wall-models to compressible flows, $U_{||}$ is replaced by the van Driest velocity [104] u_{eff} given as

$$u_{eff} = \int_0^{u_{mp}} \sqrt{\frac{\rho}{\rho_w}} du, \tag{3.38}$$

where u_{mp} is the velocity at the wall model matching point and ρ_w is the density at the wall. This equation was simplified and rewritten to be a function of Mach number at the matching point, M_{mp}, and the specific heat ratio, γ. It is given as

$$u_{eff} = u_{mp} \frac{\sin^{-1}(A)}{A}, \tag{3.39}$$

where

$$A = \sqrt{\frac{\frac{\gamma-1}{2} M_{mp}^2}{1 + \frac{\gamma-1}{2} M_{mp}^2}}. \tag{3.40}$$

The flow variables at the matching point along with the van Driest velocity given by equation 3.38 are then used to compute the friction velocity utilizing a wall-model. The compressible wall shear stress is then calculated using

$$\tau_w = \rho_w u_\tau^2. \tag{3.41}$$

But the above approach is only valid for geometries in which the boundary conforms to a Cartesian mesh. Curvilinear meshes are needed for practical nozzle geometries. On curvilinear meshes, the shear stress, τ_w computed using equation 3.41 acts parallel to the wall in the $\xi - \zeta$ plane (assuming the wall is located at a constant value in η direction). The computation of the stress tensor that is present in the governing equations requires the shear stress in Cartesian coordinates. But τ_w computed in $\xi - \zeta$ plane using the wall-model is not the same in Cartesian coordinates. To retrieve the Cartesian stress components, the methodology developed by Sondak and Pletcher [105] is used. It extends the application of wall-models to curvilinear meshes by performing generalized curvilinear coordinate transformations. First, the physical wall-parallel velocity is computed using

$$U_{||} = |u_\alpha^p \vec{e}_\alpha + u_\beta^p \vec{e}_\beta|, \tag{3.42}$$

in which u_α^p is the physical velocity component in generalized coordinates given by

$$u_\alpha^p = U_\alpha \sqrt{g_{\alpha\alpha}}, \tag{3.43}$$

where U_α and $g_{\alpha\alpha}$ represent the contravariant velocity in generalized coordinates and metric tensor respectively and are given as

$$U_\alpha = \frac{\partial \xi_\alpha}{\partial x_i} u_i, \tag{3.44}$$

$$g_{\alpha\beta} = \frac{\partial x_i}{\partial \xi_\alpha} \frac{\partial x_i}{\partial \xi_\beta}. \tag{3.45}$$

The vector $\vec{e}$ in equation 3.42 is the covariant basis vector

$$\vec{e}_\alpha = \frac{\partial x_i}{\partial \xi_\alpha} \Bigg/ \left| \frac{\partial x_i}{\partial \xi_\alpha} \right|. \tag{3.46}$$

The physical wall-parallel velocity (equation 3.42) is then used in the wall-model to obtain the wall shear stress. For a wall at a constant value of the wall-normal coordinate η, the wall tangential physical velocity components at the matching point in generalized coordinates, u_ξ^p and u_ζ^p, can be used to break down the wall shear stress into curvilinear physical shear stresses in the tangential direction, $\tau_{\xi\eta}^p$ and $\tau_{\zeta\eta}^p$, respectively. They are given by

$$\tau_{\xi\eta}^p = \frac{u_\xi^p}{U_{||}} \Bigg| \tau_w, \tag{3.47}$$

$$\tau_{\zeta\eta}^p = \frac{u_\zeta^p}{U_{||}} \Bigg| \tau_w. \tag{3.48}$$

The symmetric nature of the stress tensor yields

$$\tau_{\eta\xi}^p = \tau_{\xi\eta}^p, \tag{3.49}$$

$$\tau_{\eta\zeta}^p = \tau_{\zeta\eta}^p. \tag{3.50}$$

The other components of the curvilinear physical shear stress are set to zero. They can be arranged in a matrix form as

$$P = \begin{bmatrix} 0 & \tau_{\xi\eta}^p & 0 \\ \tau_{\eta\xi}^p & 0 & \tau_{\eta\zeta}^p \\ 0 & \tau_{\zeta\eta}^p & 0 \end{bmatrix}. \tag{3.51}$$

Following Sondak and Pletcher [105], the stress components in generalized coordinates (non-physical) can be obtained by using the transformation

$$T = S^{-1} P \left[(S^{-1} G)^T \right]^{-1}, \tag{3.52}$$

in which matrices G and S are defined as

$$G = \begin{bmatrix} g_{11} & g_{12} & g_{13} \\ g_{21} & g_{22} & g_{23} \\ g_{31} & g_{32} & g_{33} \end{bmatrix}, \tag{3.53}$$

$$S = \begin{bmatrix} \sqrt{g_{11}} & 0 & 0 \\ 0 & \sqrt{g_{22}} & 0 \\ 0 & 0 & \sqrt{g_{33}} \end{bmatrix}. \tag{3.54}$$

Finally, the correct stresses in Cartesian coordinates can be computed using

$$\tau_{ij} = \frac{\partial x_i}{\partial \xi_\alpha} \frac{\partial x_j}{\partial \xi_\beta} T_{\alpha\beta}. \tag{3.55}$$

The implementation to apply a wall-model for curvilinear meshes by Aikens [45] in the modular LES code was limited only to grids that are orthogonal in the wall-normal direction. For simulations that were simulated earlier using the modular-LES code, the meshes were designed such that they are orthogonal in the wall-normal direction. To overcome this limitation, following Sondak and Pletcher [105], the metric transformations have been implemented in the current work. The metric transformations require defining a new coordinate, γ, that is perpendicular to the wall. Assuming a wall to be located in the $\xi - \zeta$ plane at a constant value of η, the new coordinate system is then (ξ, γ, ζ). Similar coordinate systems can be constructed for a wall that is located in the other two planes. The γ metrics of the new coordinate system are calculated using

$$x_\gamma = b\eta_x, \tag{3.56}$$

$$y_\gamma = b\eta_y, \tag{3.57}$$

$$z_\gamma = b\eta_z, \tag{3.58}$$

where b is the proportionality factor given as

$$b = \frac{J^{-1}}{x_\xi(\eta_y z_\zeta - \eta_z y_\zeta) + y_\xi(\eta_z x_\zeta - \eta_x z_\zeta) + z_\xi(\eta_x y_\zeta - \eta_y x_\zeta)}. \tag{3.59}$$

Here, J is the Jacobian given by equation 2.13 and the metric terms in the original coordinate system are given by equation 2.12. Using the newly defined γ metrics, all the remaining metric terms in the new coordinate system are then defined as

$$\begin{bmatrix} \xi_x & \xi_y & \xi_z \\ \gamma_x & \gamma_y & \gamma_z \\ \zeta_x & \zeta_y & \zeta_z \end{bmatrix} = J \begin{bmatrix} y_\gamma z_\zeta - z_\gamma y_\zeta & x_\zeta z_\gamma - x_\gamma z_\zeta & x_\gamma y_\zeta - y_\gamma x_\zeta \\ y_\zeta z_\xi - z_\zeta y_\xi & x_\xi z_\zeta - x_\zeta z_\xi & x_\zeta y_\xi - y_\zeta x_\xi \\ y_\xi z_\gamma - z_\xi y_\gamma & x_\gamma z_\xi - x_\xi z_\gamma & x_\xi y_\gamma - y_\xi x_\gamma \end{bmatrix}. \tag{3.60}$$

For handling non-orthogonal meshes, the newly defined coordinate system, and mesh metrics are only used in the computation of the Cartesian stress components given by equation 3.55. They are not used elsewhere in the LES.

The stresses yielded by equation 3.55 are then used to specify the flux boundary condition at the wall in the governing Navier-Stokes equation (equation 2.3) during time advancement. It is a usual practice to choose the first point off the wall as the matching point from which LES data is sampled. But for equilibrium stress wall-models, Kawai and Larsson [21] suggest using a grid point higher than the first grid point for the matching point. This is because of the numerical Nyquist criterion, which requires the need of at least two grid points for proper resolution of a wavelength. When the first grid point from the wall is chosen, this criterion is violated, and the wall model is fed inaccurate information, as the eddies in the log-layer are not well resolved. So, a point higher than the first point off the wall is chosen as the matching point when using any of the wall-models.

When using the wall-model boundary condition, the walls are treated as adiabatic. Therefore, the heat flux on the wall is set to zero. The governing equations are then time-advanced for the points away from the wall. The wall pressure is obtained from the exterior LES solution using a fourth-order extrapolation that approximates

$$\left.\frac{\partial \langle p \rangle}{\partial y}\right|_w = 0. \tag{3.61}$$

The density at the wall is specified by assuming the wall temperature to be equal to the total temperature at the matching point, $T_w = T_{0mp}$, and calculated as

$$\frac{\rho_w}{\rho_{mp}} = \frac{p_w}{p_{mp}} \left(1 + \frac{\gamma - 1}{2} M_{mp}^2\right)^{-1}. \tag{3.62}$$

As the flow is not adequately resolved near the wall due to the use of a coarser grid when wall-models are used, the numerical schemes in the wall-normal direction are modified based on the recommendation of Kawai and Larsson [21]. Here, an explicit second-order central difference scheme is used at the first point away from the wall. The schemes described in section 2.2 are still employed at other locations. This is also shown in figure 3.1. Doing this removes the dependency between the resolved (away from the wall) and unresolved (closer to the wall) flowfields, which are otherwise coupled due to the use of implicit compact schemes for flux derivatives.

4. PRELIMINARY ANALYSIS OF JETS FROM SMC000 NOZZLE

This chapter discusses the preliminary simulations that were performed of flow through the short metal chevron (SMC) baseline nozzle designated as SMC000. As described in section 1.1, differences exist between the results of the wall-resolved [48] and wall-modeled [45] cases that were simulated using the modular-LES code for a Mach 0.9 isothermal jet through an SMC000 nozzle operating at a Reynolds number of 10^5. Both flowfield and acoustic results varied between the two cases. The noise levels of the wall-modeled case are found to be lower than the wall-resolved case. The behavior of mean turbulence statistics at the nozzle exit affected the noise levels. The mean turbulence statistics are higher for the wall-modeled case in comparison with the wall-resolved case leading to lower noise levels in the flowfield.

A total of seven wall-modeled cases were simulated to understand the cause of differences between the reference wall-resolved and wall-modeled simulations. The simulation settings of the current cases are modified from the reference wall-modeled case to examine the response of the flow to their changes. The analysis aims to focus on the flow development at the nozzle exit and not to compute acoustics. So, a shorter domain length is used in the current simulations. The domain length is limited to $5R_j$, unlike $80R_j$ used by Aikens [45]. The resolution of the grid used in most of the current simulations is kept to be the same as the one used by Aikens [45]. However, for one case, the grid is refined in the wall-normal direction near the inner nozzle wall.

Moving forward, the wall-resolved case of Dhamankar [48] will be referred to as *WR* and the wall-modeled case of Aikens [45] as *WM*. Table 4.1 lists all the cases simulated here and the parameters that are different from the *WM* case. The first simulation performed here is the case *SS_12_TEST*. It was simulated using identical

settings of *WM* for validation. Case *SS_12_WRLS* was simulated by using the turbulent length scales at the inlet similar to what is used in the *WR* case. The other simulation settings are left to be the same as that of the *WM* case. As mentioned earlier, there are minor differences between the turbulent length scales used at the inlet boundary between the *WR* and *WM* simulations. The case *SS_12_WRLS* will help in understanding the impact of turbulent length scales on the flowfield developing downstream. All the subsequent simulations that are carried out use the *WR* case's turbulent length scales at the inflow.

Table 4.1. Simulation parameters different from the wall-modeled case of Aikens [45].

Case Name	**Differences**
SS_12_TEST	None
SS_12_WRLS	Length scales
SS_12_GEWM	Length scales and wall model
SS_12_TURB_0.5	Length scales, wall model and velocity fluctuations (reduced by 50%)
SS_12_TURB_0.35	Length scales, wall model and velocity fluctuations (reduced by 65%)
SS_12_TURB_0.25	Length scales, wall model and velocity fluctuations (reduced by 75%)
SS_12_REFINED	Length scales, wall model and grid (refined in wall normal direction)

Since $y^+ < 50$ at the matching point of the *WM* case, the case *SS_12_GEWM* was simulated using the GEWM wall-model. The GEWM is valid even for $y^+ < 50$. The remaining simulations described below uses the GEWM due to its robustness. Three cases were simulated by reducing the density and velocity fluctuations added

to the mean flow at the inlet. The fluctuation levels are reduced by 50%, 65%, and 75% in comparison with the *SS_12_GEWM* case. These cases are designated as *SS_12_TURB_0.5*, *SS_12_TURB_0.35*, and *SS_12_TURB_0.25*, respectively. Finally, the case *SS_12_REFINED* is simulated using a finer grid.

The following sections present more details of the simulations along with the results. First, the details about the nozzle and operating conditions used are described in section 4.1. The domain lengths, grid sizes and various settings used in the simulations are mentioned in section 4.2. Finally, the results are discussed in 4.3.

Figure 4.1. SMC000 nozzle mounted on a base (center) along with a collection of chevron nozzles [17].

4.1 Nozzle Description and Operating Conditions

The SMC000 nozzle is one of the eleven nozzles belonging to a parametric family of chevron nozzles studied experimentally by Bridges and Brown [8]. The nozzles are designed to explore how chevron geometric parameters like chevron count, penetration, length, and symmetry enhance the mixing process and influence flowfield and acoustic results. The SMC000 nozzle does not have any chevrons and is used as the baseline case. It is also one of the nozzle designs used for the development and

validation of the small hot jet aeroacoustic rig (SHJAR) at NASA Glenn Research Center [17,106] to test various noise reduction concepts. The nozzle is shown in figure 4.1. It is a converging nozzle with a final contraction of 5° and has an exit diameter of 51.0mm (or 2 inches). The lip thickness is 6% of the nozzle exit radius R_j. The converging angle of the outer wall is about 12.3°. The SMC000 nozzle is mounted upstream to a pipe which has a contraction. The pipe is about $7R_j$ long and has an inlet diameter of $6R_j$. The pipe contracts sharply with a converging angle of 27° to achieve the final taper near the exit. A drawing of the SMC000 nozzle is shown in figure 4.2.

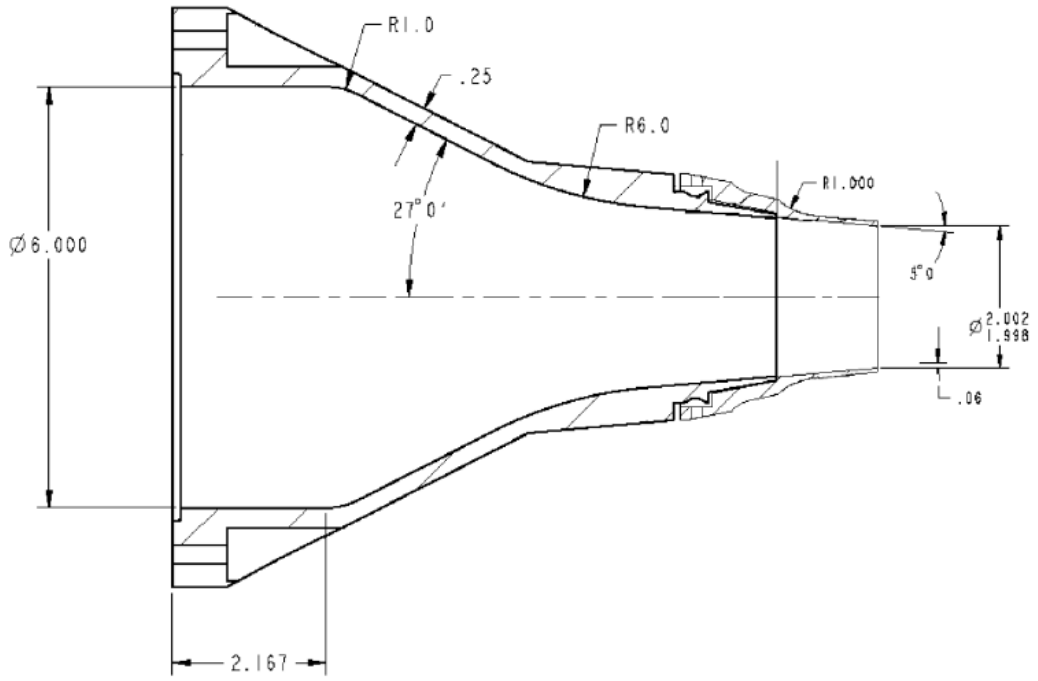

Figure 4.2. SMC000 nozzle drawing from reference [106].

Similarly to the *WR* and *WM* cases, the current cases are simulated at operating conditions designated as SP12 by Tanna et al. [56]. The SP12 conditions correspond to an isothermal jet operating at a Mach number of 0.9. The Reynolds number based on diameter, Re_{D_j} is 10^5 and the dimensional ambient temperature is assumed to be $T^*_\infty = 286$K. The operating conditions are tabulated in table 4.2.

Table 4.2. SP12 Operating conditions used for preliminary SMC000 nozzle simulations.

Parameter	**Value**
Acoustic Mach number at nozzle exit ($M_a = U_J/c_\infty$)	0.90
Mach number at nozzle exit ($M_J = U_J/c_J$)	0.90
Nozzle exit to ambient static temperature ratio (T_J/T_∞)	1 (Isothermal)
Dimensional ambient temperature(T^*_∞)	286 K
Nozzle temperature ratio (TTR $= T_0/T_\infty$)	1.16
Nozzle pressure ratio (NPR $= p_0/p_\infty$)	1.69
Reynolds number at nozzle exit ($Re_{D_J} = \rho_J U_J D_J/\mu_J$)	10^5

4.2 Simulation Setup

4.2.1 Details of the Computational Domain

As with the reference *WR* and *WM* simulations, the current simulations use only the final $1R_j$ long section of the nozzle which has a contraction angle of 5°. The nozzle is affixed with an upstream straight section of length $1R_j$. The straight section acts as a redevelopment region allowing the artificial turbulence imposed at the inflow to turn into physically realistic turbulence. Above the nozzle outer wall, the domain boundary starts at $1.4R_j$ upstream of the nozzle exit. The cylindrical domain extends $5R_j$ in the streamwise direction downstream of the nozzle exit and about $3R_j$ in the radial direction. This is unlike the $80R_j$ and $20R_j$ extents in the streamwise and radial directions, respectively, used in the *WR* and *WM* simulations. Five non-overlapping superblocks are used to construct the entire domain which are represented by numbers in figure 4.3.

The boundary conditions used in the current simulations are shown in figure 4.3. On the farfield boundaries, the non-reflecting radiation boundary condition by

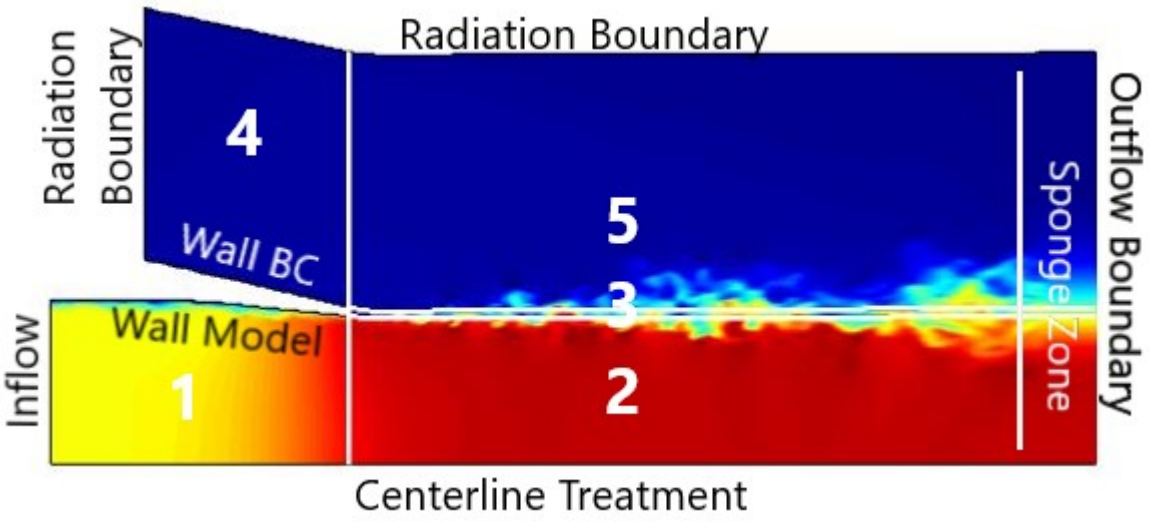

Figure 4.3. Domain details for preliminary SMC000 nozzle simulations.

Dong [107] is used. The EWM wall-model has been applied to the interior wall for the *SS_12_TEST* and *SS_12_WRLS* cases, whereas the GEWM wall-model has been employed for the remaining cases. The fifth grid point from the wall is chosen as the matching point for the *SS_12_REFINED* case, whereas the second point from the wall is selected for the other cases. On the outer nozzle walls, an isothermal hard wall boundary condition by Liu [108] is applied. Because of the low velocities in this region, the outer nozzle wall is treated as a wall-resolved boundary. At the downstream end of the domain, Tam and Dong's [85, 86] outflow boundary condition is specified. A sponge zone method proposed by Colonius *et al.* [87] is used starting from $x = 4.61R_j$ until the end of the domain. The sponge zone damps out strong vortices that convect and pass through the outflow boundary so that the numerical reflections are reduced. At the inflow boundary, a digital filter-based turbulent boundary condition [16] is specified to achieve realistic turbulent flow conditions inside the nozzle. Reichardt's velocity profile with Cole's law of the wake is used to define the mean turbulent velocity profile at the inlet. It is given as

$$u^+ = \frac{1}{\kappa}\log(1+0.4y^+)+7.8\left[1-\exp\left(-\frac{y^+}{11}\right)-\frac{y^+}{11}\exp(-0.33y^+)\right]+\frac{2\Pi}{\kappa}\sin\left(\frac{2\pi y}{\delta_{99}}\right)^2, \tag{4.1}$$

where $\Pi = 0.45$. The boundary layer thickness specified at the inlet is $\delta_{99,i} = 0.0674R_j$ and is similar to what is used in the *WR* and *WM* cases. The constant-area straight section added in front of the nozzle has a length of $14.8\delta_{99,i}$. This length satisfies the requirement of having a redevelopment region of at least $x = 11.5\delta_{99,i}$ for realistic flow turbulence to develop [16]. The integral length scales (shown in table 1.2) and Reynolds stress profiles taken from Spalart's DNS [109] for $Re_\theta = 300$ are used in the current simulations. For the *SS_12_TEST* case, the integral length scales of the *WM* case are used, whereas the other cases use the integral length scales of the *WR* case. The integral length scales and stresses aid in producing correlated fluctuations. As suggested by Dhamankar [16], a sponge zone is used inside the nozzle to damp out spurious modes in the redevelopment region generated due to the reflection of acoustic waves from the constant pressure inflow boundary. It is placed at the inflow and extends downstream $0.65R_j$ in the streamwise direction. In the radial direction, it extends between $0 \leq r/R_j \leq (R_i - 1.5\delta_{99i})/R_j$. This gap between the nozzle wall and sponge zone leaves the boundary layer development unaffected. Apart from these, to handle edges between two faces, such as the edge of the nozzle lip, a series of edge boundary conditions are also used along with the centerline treatment. The centerline treatment precludes the specification of a grid point on the centerline. So, care is taken in the design of grids to satisfy the requirement as mentioned earlier.

4.2.2 Grid Information

The commercial grid generation software Pointwise is used to design the two grids used in the current simulations. In order to make a direct comparison with the *WM* case, one of the grids maintains the same resolution as the grid used by the *WM* case. This grid is referred to as the coarse mesh. All cases utilize the coarse mesh except for

the *SS_12_REFINED* case. The grid used in the *SS_12_REFINED* case is a refined version of the coarse grid. The fine grid is refined only in the wall-normal direction near the inner nozzle wall. The fine grid consists of approximately 37.8 million grid points, whereas the coarse grid is made up of 36.5 million grid points. The difference between the two grid sizes is small because the fine grid consists of only an additional five grid points in the wall-normal direction compared to the coarse grid. The grid details are tabulated in table 4.3. Figure 4.4 shows a streamwise slice of the fine grid used in the current simulations.

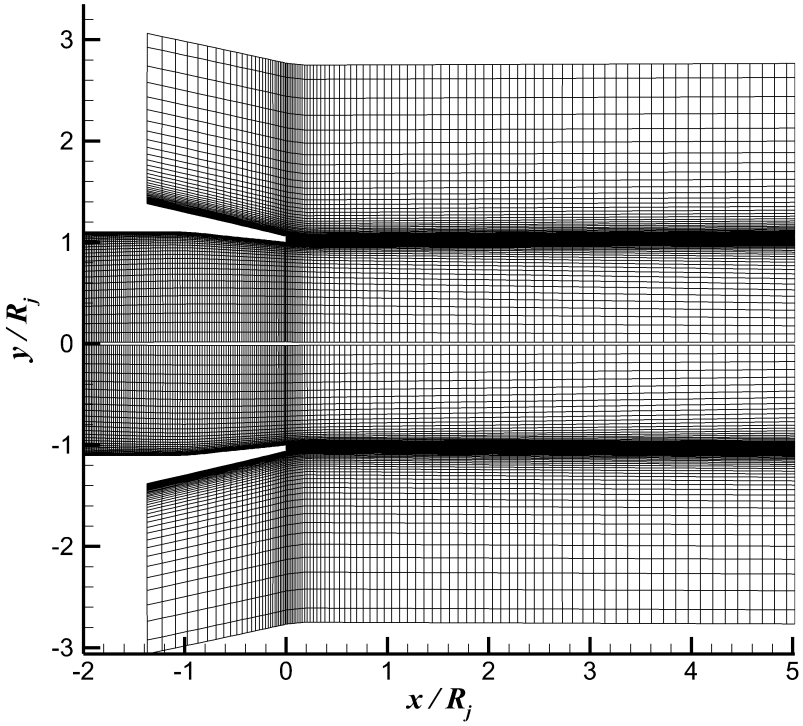

Figure 4.4. A streamwise slice of the fine grid used for preliminary SMC000 simulations. Every fourth point is shown.

Inside the nozzle, the coarse grid consists of 16 grid points in the radial direction at the nozzle inlet to resolve the boundary layer. At the inlet, the first grid point away from the wall is located at $\Delta r_w = 5 \times 10^{-2} \delta_{99,i} = 3.4 \times 10^{-3} R_j$ and the matching point is located at a distance of about $\Delta r_{mp} = 1 \times 10^{-1} \delta_{99,i} = 6.9 \times 10^{-3} R_j$. At the

Table 4.3. Domain and grid information for the preliminary SMC000 simulations.

Superblock	**Description**	N_x	N_r	N_θ
1	Nozzle	288	75 (Coarse) 80 (Fine)	512
2	Downstream of nozzle exit	201	75 (Coarse) 80 (Fine)	512
3	Downstream of nozzle exit along the nozzle lip	201	30	512
4	Above the nozzle and upstream of its exit	80	102	512
5	Downstream of Superblock 4	201	102	512

nozzle exit, the first grid point away from the wall is located at $\Delta r_w = 1.7 \times 10^{-3} R_j$. The wall-normal spacing is reduced from the inlet to exit to accommodate thinning of the boundary layer as the flow accelerates inside the nozzle. The matching point is located at a distance of about $\Delta r_{mp} = 4.6 \times 10^{-3} R_j$ from the nozzle wall at the exit. Towards the centerline, the grid spacing is increased smoothly in the radial direction. The grid stretching ratio in the radial direction inside the nozzle is limited to 1.06, with the average value being 1.033. The maximum aspect ratio in the $x - r$ plane is 5.84. A constant grid spacing of $5 \times 10^{-3} R_j$ is used in the axial direction. The axial grid spacing satisfies the requirement to have a grid spacing of at most $0.105\delta_{99}$ [51]. In the azimuthal direction, the gird is discretized using 512 points similarly to the *WR* and *WM* cases. This corresponds to $r\Delta\theta = 1.4 \times 10^{-3} R_j$ and $r\Delta\theta = 1.2 \times 10^{-3} R_j$ at the nozzle inlet and exit respectively. These grid spacings used at the nozzle inlet and exit are also reported in table 4.4. The table also lists the grid-spacing in wall units as well. For the fine grid, the spacing in the wall-normal direction is halved near

the wall and increased gradually. The spacing in the other two directions is similar to what is used for the coarse grid.

Outside the nozzle, the grid spacing is maintained to be very fine along the nozzle lip and in the region close to nozzle exit. This is evident from the grid plotted in figure 4.4. The fine spacing is required to capture the small-scale turbulence generated in the jet shear layer. The maximum grid stretching ratio in the axial direction downstream of the nozzle is below 1.04. Above the nozzle, the grid is stretched smoothly in the radial direction and has a maximum grid stretching ratio of 1.044. Since the fine grid is refined only in the boundary layer region inside the nozzle, outside the nozzle, both the fine and coarse grids have mostly the same quality expect in the shear layer.

4.2.3 Additional Simulation Settings

The table 4.5 shows the additional settings used in the simulations. FTC in the table refers to flow-through-cycle. It is the time required for a particle moving at the jet exit velocity to travel the streamwise extent of the domain once. The times shown in the table are in terms of the reference time $T = R_j/U_j$. The simulations were run in two phases. First, the transients phase, during which the starting transients are removed, and the turbulent jet is allowed to become fully established. Subsequently, the simulations were continued to collect statistics and acoustic data during the statistics phase. The flowfield solution from the reference wall-modeled LES is used as an initial solution for the current runs, because of which the transient time is cut down. Initially, a few cases were run for a total period of $184T$. But the results showed converged statistics even when using a shorter statistics gathering period. So for later cases, the simulations were completed using a total period of $80T$ only. The machine details and computational costs for running these simulations are also specified in table 4.5. Simulations were completed using both the Rice supercomputer of Rosen Center for Advanced Computing (RCAC) and Stampede supercomputer of the Texas Advanced Computing Center (TACC).

Table 4.4. Grid spacings used in the nozzle grid of the preliminary SMC000 simulations.

Grid	**Location**	$\boldsymbol{\Delta x}$	$\boldsymbol{\Delta r_w}$	$\boldsymbol{\Delta r_{mp}}$	$\boldsymbol{r\Delta\theta}$	$\boldsymbol{\Delta x^+}$	$\boldsymbol{\Delta r_w^+}$	$\boldsymbol{\Delta r_{mp}^+}$	$\boldsymbol{r\Delta\theta^+}$
Coarse	Inlet	$5.0 \times 10^{-3} R_j$ $7.4 \times 10^{-2} \delta_{99}$	$3.4 \times 10^{-3} R_j$ $5.0 \times 10^{-2} \delta_{99}$	$6.9 \times 10^{-3} R_j$ $1.0 \times 10^{-1} \delta_{99}$	$1.4 \times 10^{-2} R_j$ $2.0 \times 10^{-1} \delta_{99}$	9	6	12	24
Coarse	Exit	$5.0 \times 10^{-3} R_j$	$1.7 \times 10^{-3} R_j$	$3.5 \times 10^{-3} R_j$	$1.2 \times 10^{-2} R_j$	15	5	10	34
Fine	Inlet	$5.0 \times 10^{-3} R_j$ $7.4 \times 10^{-2} \delta_{99}$	$1.7 \times 10^{-3} R_j$ $2.5 \times 10^{-2} \delta_{99}$	$9.4 \times 10^{-3} R_j$ $1.4 \times 10^{-1} \delta_{99}$	$1.4 \times 10^{-2} R_j$ $2.0 \times 10^{-1} \delta_{99}$	9	3	17	25
Fine	Exit	$5.0 \times 10^{-3} R_j$	$8.0 \times 10^{-4} R_j$	$4.6 \times 10^{-3} R_j$	$1.2 \times 10^{-2} R_j$	15	2	13	36

Table 4.5. Remaining simulation settings used in the preliminary SMC000 simulations.

Time Details			
Case Name	*SS_12_TEST* *SS_12_WRLS* *SS_12_GEWM*	*SS_12_TURB_0.5* *SS_12_TURB_0.35* *SS_12_TURB_0.25*	*SS_12_REFINED*
Time step size, Δt (T)	8×10^{-4}	8×10^{-4}	4×10^{-4}
Transient period (T)	40 (6 FTC)	40 (6 FTC)	40 (6 FTC)
Transient time steps	50,000	50,000	100,000
Statistics gathering period (T)	144 (21 FTC)	40 (6 FTC)	40 (6 FTC)
Statistics gathering period time steps	180,000	50,000	100,000
Max CFL Numbers (x, r, θ)	(0.34, 0.92, 0.70)	(0.34, 0.92, 0.70)	(0.17, 0.8, 0.33)
Machine Details			
Machine	RCAC Rice	TACC Stampede	RCAC Rice
Cores	152	1008	360
Cost per simulation (core-hours)	17,000	5,000	12,000

4.3 Discussion of the Results

This section discusses the results of the preliminary SMC000 nozzle simulations. The results are compared with the numerical results of Dhamanakar [48] and Aikens [45]. As mentioned previously, Dhamanakar's wall-resolved simulation and Aikens's wall-modeled simulation will be referred to as the WR and WM cases respectively. All the statistical quantities presented are averaged both in time and in the azimuthal direction. The *SS_12_TEST* case was simulated to validate the results with the *WM* case which uses a longer domain. The use of a shorter domain only has a minimal impact on the current results at the nozzle exit as can be observed from the mean velocity and turbulent kinetic energy plotted in figure 4.5. The nondimensional turbulent kinetic energy, k is computed using

$$k = \frac{(u'_x)^2_{rms} + (u'_r)^2_{rms} + (u'_\theta)^2_{rms}}{2}. \tag{4.2}$$

Since no major differences are found between the *SS_12_TEST* and *WM* cases, the results of the *SS_12_TEST* case are omitted from the following discussion for brevity.

Figure 4.6 shows the comparison of radial profiles at the nozzle exit between the current simulations and the reference data for both the mean velocity and density. The velocity and density are plotted against the distance from the centerline. Qualitatively, the results between the wall-resolved and wall-modeled cases agree with each other. Comparing with the WR case, the current wall-modeled cases simulated by changing a few parameters did not show any major improvement than their predecessor WM simulation. The boundary layer developing at the nozzle exit is still slightly thicker for the wall-modeled cases in comparison to the *WR* case. The inflow parameters like the integral length scales and varying of velocity fluctuations make only small differences in the results. Lowering of velocity fluctuations added to the mean velocity slightly increases the boundary layer thickness in comparison with the *WM* case. Both Bogey et al. [57] and Bres et al. [110] simulated Mach 0.9 isothermal jets operating at Reynolds numbers of 10^5 and 10^6, respectively, and noticed only minor variations in the mean velocity profiles when varying the velocity fluctuations, which

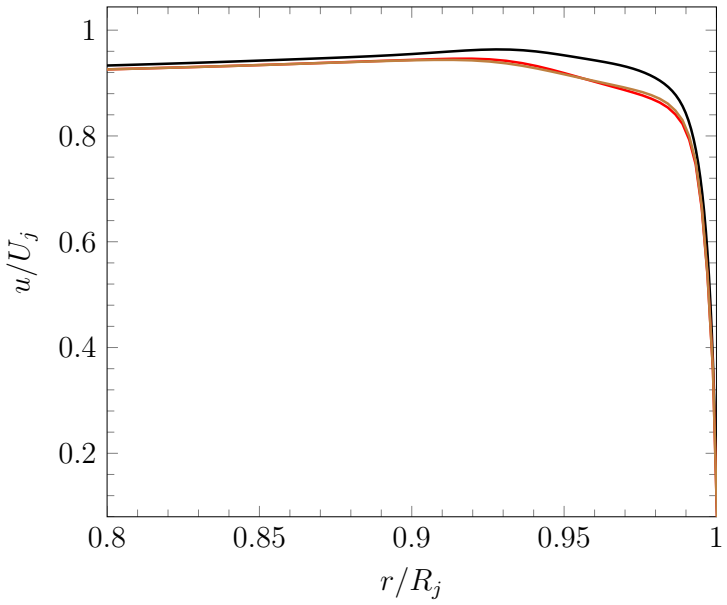

(a) Mean velocity

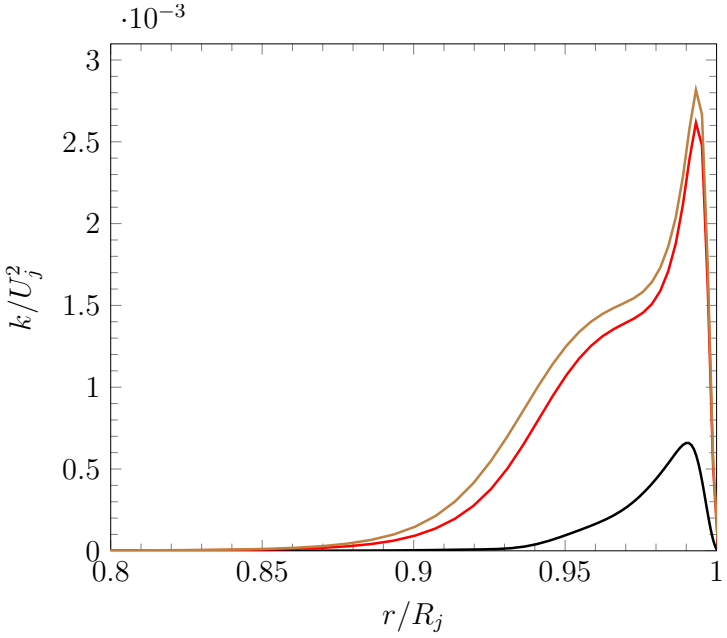

(b) Turbulent kinetic energy

WR *WM* *SS_12_TEST*

Figure 4.5. Comparison of radial profiles at the exit of SMC000 nozzle between the *WR*, *WM* and *SS_12_TEST* cases.

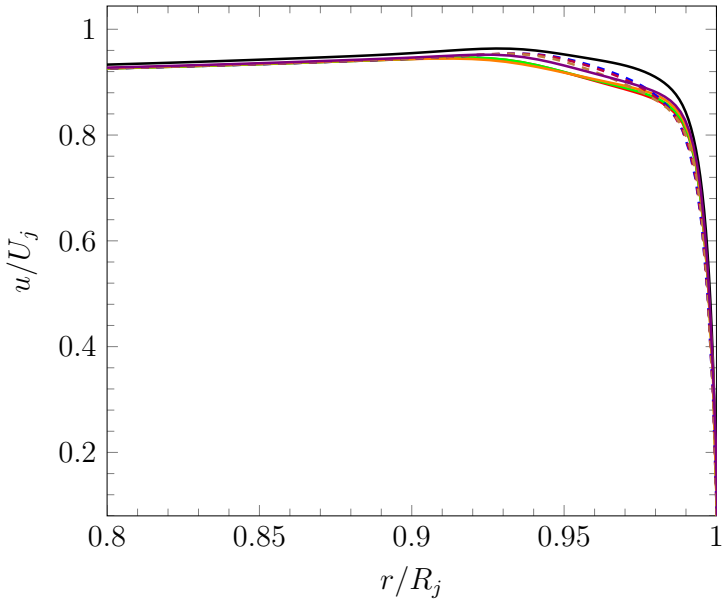

(a) Mean velocity

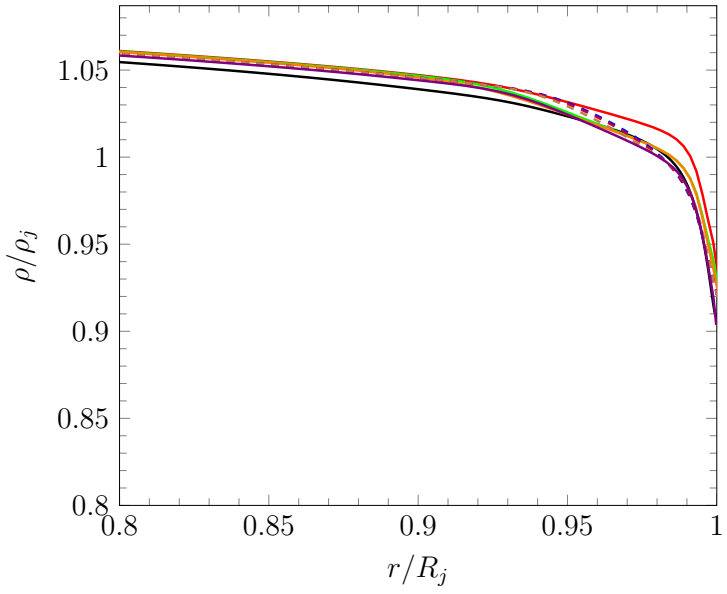

(b) Mean density

WR *WM* *SS_12_WRLS* *SS_12_GEWM*
SS_12_TURB_0.25 *SS_12_TURB_0.35* *SS_12_TURB_0.5* *SS_12_REFINED*

Figure 4.6. Mean radial profiles at the exit of SMC000 nozzle.

is in accordance with the current results seen here. The use of GEWM made very difference as can be noticed by comparing the *SS_12_WRLS* and *SS_12_GEWM* cases. Although, the mean density differences are very minor between the wall-modeled and wall-resolved simulations, closer to the wall, the density profiles of the current wall-modeled cases match better with the *WR* case. Overall, the mean variables at the nozzle exit are influenced neither by the changes introduced at the inlet nor use of the $GEWM$ wall-model.

The turbulent kinetic energy (TKE) and Reynolds shear stress are plotted in figure 4.7. As mentioned earlier, the turbulent kinetic energy for the WM case is higher than that of the *WR* case. The change of turbulent length scales and use of the GEWM wall-model have a very minimal impact on the results. In comparison with the *WM* case, the TKE of *SS_12_WRLS* case peaks slightly lower when the length scales are varied to match with the *WR* case, whereas the TKE of the *SS_12_GEWM* case is higher which uses the GEWM wall-model. But the results of both the *SS_12_WRLS* and *SS_12_GEWM* cases still overpredict the *WR* case. Significant differences are noticed in the TKE levels when the velocity fluctuations specified at the inflow are reduced. Lowering the velocity fluctuations at the inflow reduces the TKE at the exit. The velocity fluctuations are varied using a trial and error approach to match the *WR* case. The results of the *SS_12_TURB_0.35* case tend to collapse onto the results of the *WR* case. Refining the grid in the wall-normal direction also impacts the results considerably. The turbulence levels for the *SS_12_REFINED* case peak lower than the *WM* case. The individual components that make up the TKE: rms fluctuating velocities in the axial, radial and azimuthal directions are shown in figure 4.8. Similar trends are noticed for each of the individual components between the simulations. In all the cases, the peak magnitude of the rms fluctuating velocity is highest in the axial direction, followed by the azimuthal and radial components. This trend is similar to that noticed by Klebanoff [111] based on the flat plate boundary layer results. Klebanoff [111] estimated the ratio of relative magnitudes as 4:2:3 for the axial, radial, and azimuthal components. Figure 4.7 also shows the Reynolds

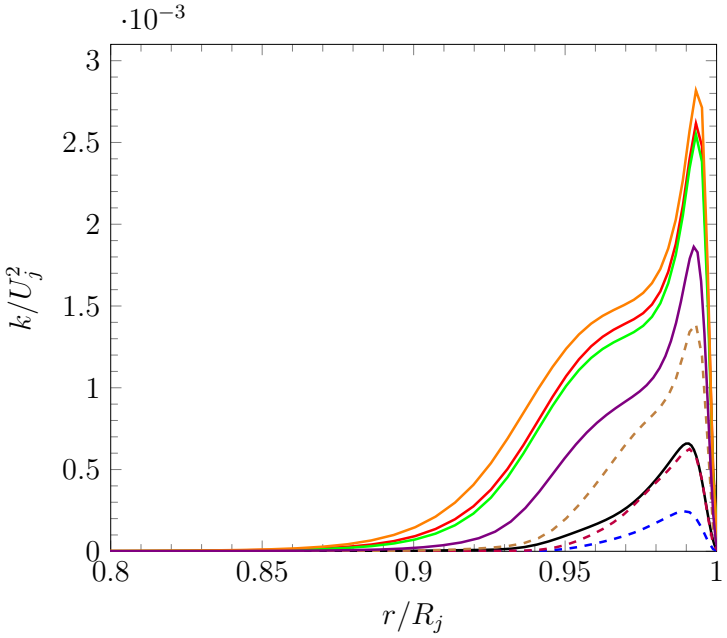

(a) Turbulent kinetic energy

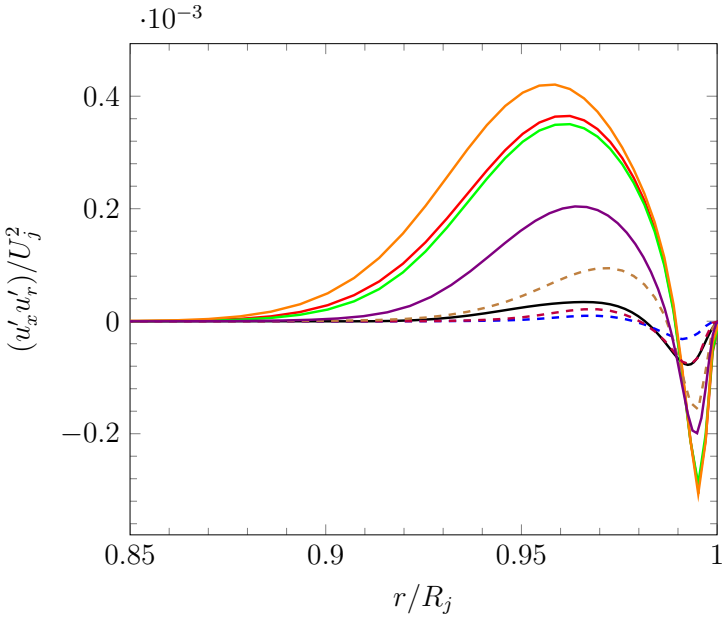

(b) Reynolds shear stress

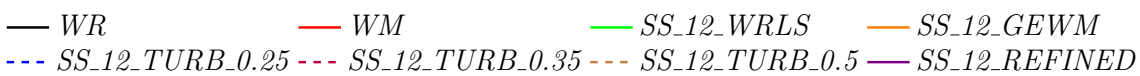

Figure 4.7. Radial profiles of turbulent quantities at the exit of SMC000 nozzle.

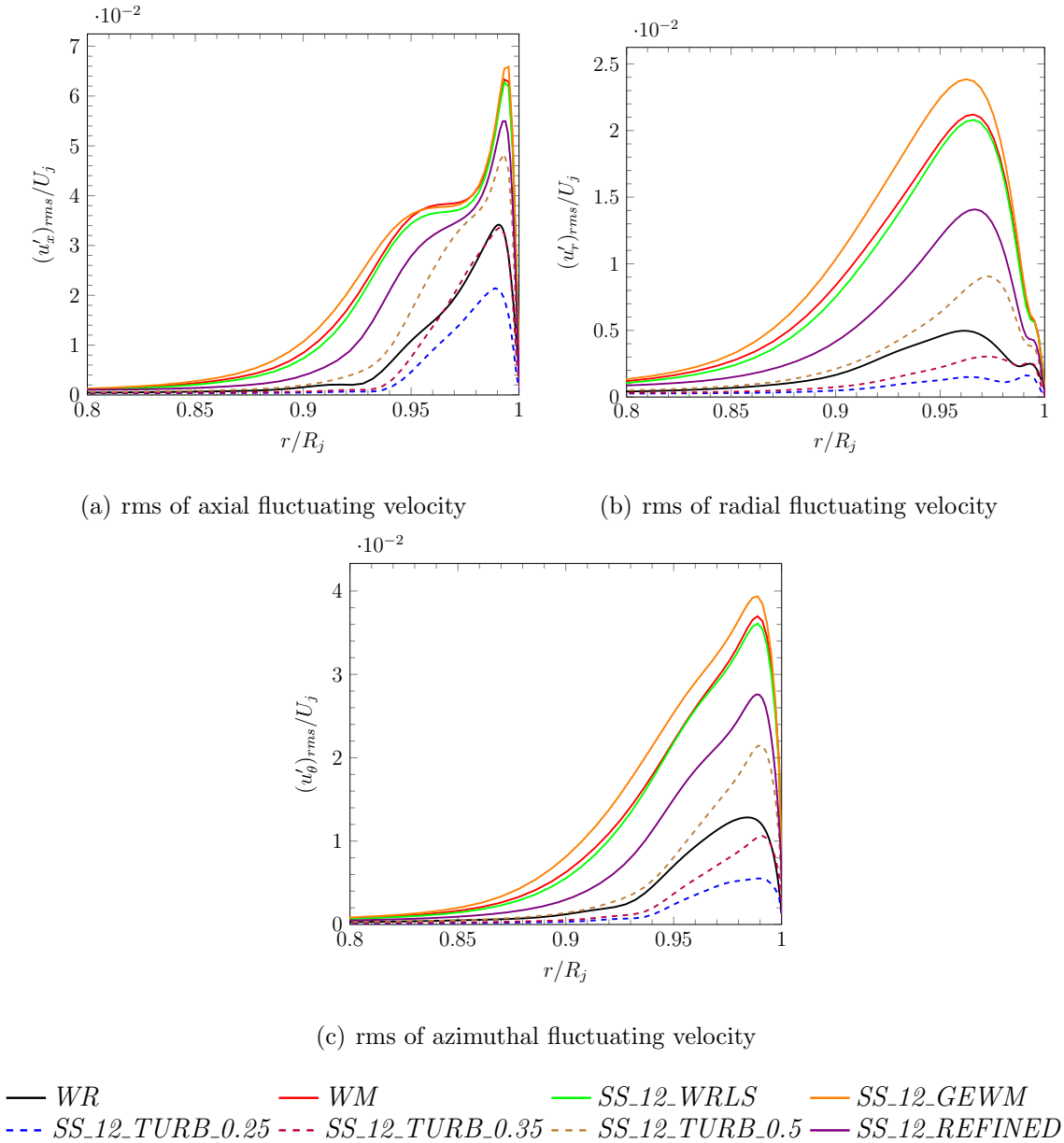

(a) rms of axial fluctuating velocity

(b) rms of radial fluctuating velocity

(c) rms of azimuthal fluctuating velocity

Figure 4.8. Radial profiles of rms fluctuating velocities at the exit of SMC000 nozzle.

shear stress, and it follows the general trends of TKE between the cases simulated here.

The impact of the changes made to the simulations on the results downstream of the nozzle is now examined. The mean velocity and rms fluctuations in the axial direction are plotted along the centerline and lipline from the nozzle exit up to $4R_j$ and shown in figures 4.9 and 4.10, respectively. Due to the use of a short-domain in the current simulations, the impact of the changes on the potential core length and turbulence levels in the shear layer are not fully known. Figure 4.9(a) depicts the mean axial velocity along the centerline and the results are close to each other. Again, the use of the GEWM wall-model and different length scales have a minimal impact on the results. As the inflow velocity fluctuations are reduced, noticeable changes can be observed, and the results of the wall-modeled cases approach those of the *WR* case. Similar changes are observed with the *SS_12_REFINED* case as well. The rms velocity fluctuations in the axial direction along the centerline are shown in figure 4.9(b). The magnitude of the fluctuations reaching the centerline is very low as the shear layer is just starting to develop near the nozzle exit. From the full domain simulations, peak levels were noticed after $20R_j$ from the nozzle exit. That being said, the levels are more or less the same for all the cases, except for the *SS_12_REFINED* case for which the fluctuation levels are some what higher.

In figure 4.10(a), the mean axial velocity along the lipline is shown. The changes made to the simulations have some impact on the development of the shear layer. Considerable differences can be noticed very close to the nozzle exit between the cases. However, as the flow propagates downstream, the mean profiles seem to converge. The rms velocity fluctuations in the axial direction along the lipline are shown in figure 4.10(b). As mentioned earlier, lower levels of fluctuations in the nozzle boundary layer lead to higher fluctuations in the shear layer. This can be noticed clearly for the *SS_12_TURB_0.25* and *SS_12_TURB_0.35* cases which peak close to the *WR* case. The higher fluctuation levels in the boundary layer for the *SS_12_GEWM* case lead to lower fluctuation levels in the shear layer and peaks lower than the *WM* case.

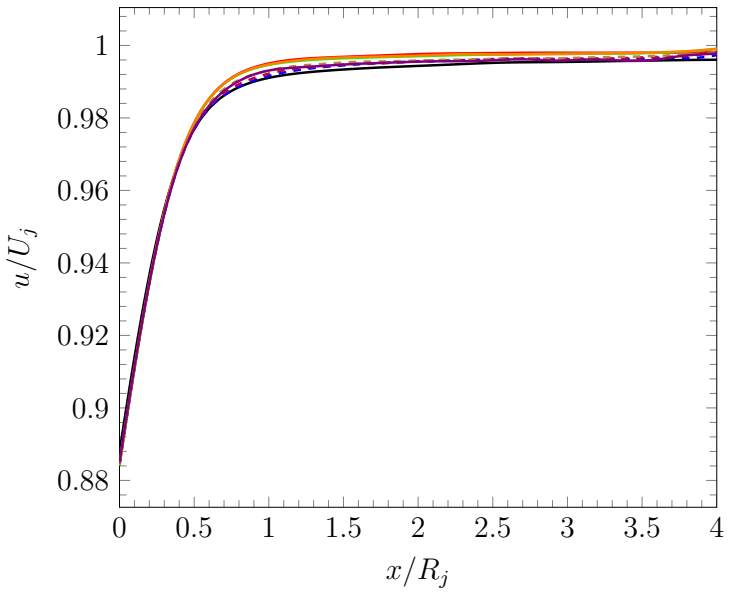

(a) Mean velocity

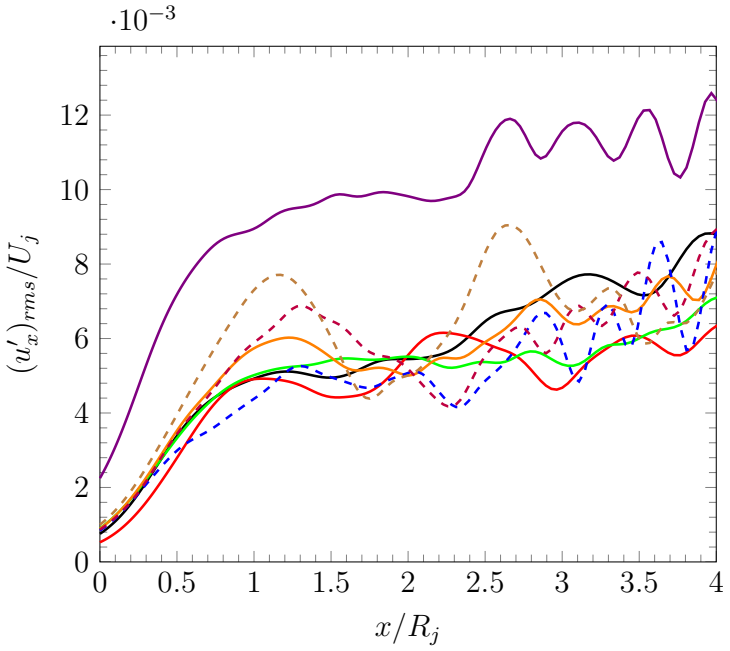

(b) rms of axial velocity fluctuation

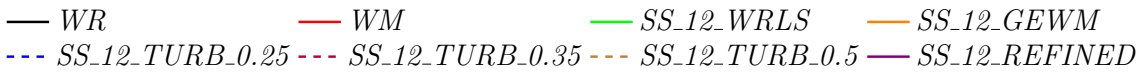

Figure 4.9. Centerline profiles for the SMC000 nozzle.

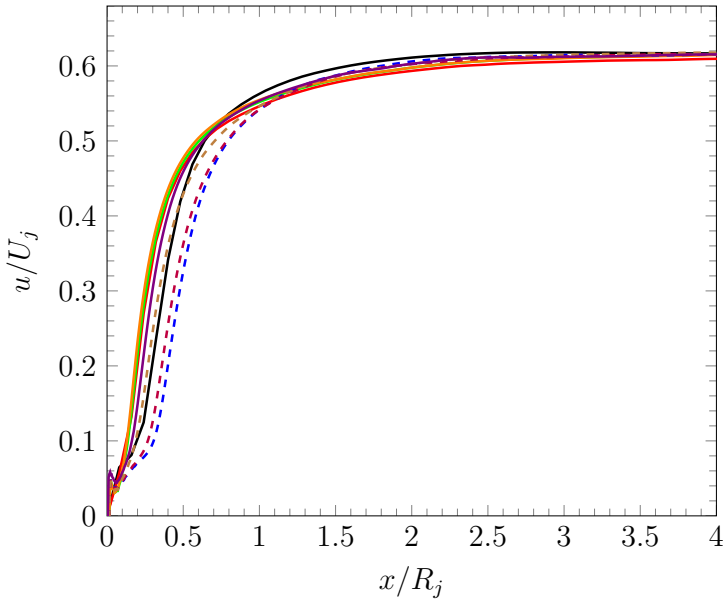

(a) Mean velocity

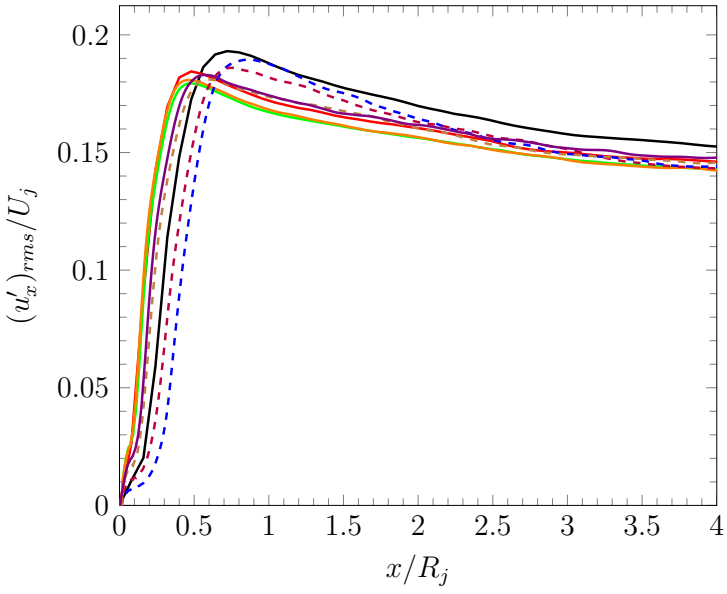

(b) rms of axial velocity fluctuation

WR *WM* *SS_12_WRLS* *SS_12_GEWM*
SS_12_TURB_0.25 *SS_12_TURB_0.35* *SS_12_TURB_0.5* *SS_12_REFINED*

Figure 4.10. Lipline profiles for the SMC000 nozzle.

Although the changes made to the integral length scales for the *SS_12_WRLS* case have minimal impact in comparison with the *WM* case, the fluctuations are slightly lower for the *SS_12_WRLS* case than that of the *WM* case. The reason for this behavior is unclear.

4.4 Summary and Conclusions

In this work, the inflow parameters like integral length scales, velocity fluctuations along with the use of a generalized equilibrium wall model are explored to study their impact on the flowfield. Their influence on the flowfield is used to gain some understanding of the flowfield and acoustic differences noticed between the predecessor wall-resolved and wall-modeled SMC000 simulations. So, multiple wall-modeled LES of the flow through an SMC000 nozzle were carried out using a shorter domain. The changes that are made have only a minor impact on the mean flow statistics. However, the changes made in the current simulations affected the turbulent statistics. The following conclusions are made based on the results obtained in this study.

The integral length scales that characterize the inflow did not affect the results. The length scales are modified only in the axial and azimuthal directions to match with the wall-resolved simulation. Since the differences are minor, the flowfield did not alter much from the reference wall-modeled case. The purpose of this case was primarily to validate that the differences in the length scales used at the inlet for the *WR* and *WM* cases are inconsequential and to then obtain a wall-modeled simulation with length scales that are consistent with the wall-resolved case. The choice of the generalized equilibrium wall-model was guided by the fact that the matching point in the reference wall-modeled simulation is located in the linear-region of the boundary layer. In the linear region, the EWM wall-model is not valid. The use of GEWM wall-model did not improve the results.

The cases simulated by varying the velocity fluctuations at the inflow demonstrated significant changes in the turbulence statistics computed at the nozzle exit.

Lowering of velocity fluctuations at the inflow, decreased the turbulence levels at the nozzle exit and eventually affected the shear flow that is developing downstream of the nozzle exit. Turbulence levels are increased in the shear layer as the velocity fluctuations are decreased at the inflow. This trend is consistent and is noticed by other researchers as well. A good agreement with the wall-resolved case was obtained when the velocity fluctuations are lowered by 65% of the values used in the baseline case. Finally, the grid refinement effects are examined. The grid is refined only in the wall-normal direction. Refining the grid decreased the turbulence levels at the nozzle exit and improved the prediction in comparison with the wall-resolved case, which implies that a finer grid is required to capture the fluctuation levels accurately.

The adjustment of the fluctuations levels at the inflow and grid refinement proved to be useful in producing flowfields similar to that of the wall-resolved simulation. However, controlling the fluctuation levels at the inflow make the wall-modeling no longer predictive. On the other hand, grid refinement defeats the purpose of wall-modeling. The simulations become more expensive due to the use of finer grids. However, there must be a tradeoff in choosing the number of grid points required in the near wall region to correctly resolve the boundary layer. The wall-models used in this chapter are based on the equilibrium stress assumption, which is usually valid for flows having no pressure gradient. So, it is worthwhile to look into more robust wall-models which can incorporate the non-equilibrium effects due to pressure gradients, as nozzle flows are dominated by pressure gradients. In the next chapter, the shortcomings of the equilibrium wall-models will be addressed by implementation of new wall-models that can account for the pressure gradients. Further validation of the old and newly implemented wall-models will be done by simulating flows subjected to pressure gradients.

5. ANALYSIS AND VALIDATION OF THE WALL-MODELS

In this chapter, the newly implemented wall-models, the generalized equilibrium wall-model (GEWM) [29], generalized non-equilibrium wall-model (GNEWM) [33, 60] and integral wall-model (IWM) [61] are analyzed and validated through the simulations of two test cases. Along with the new wall-models, simulations are also performed using the equilibrium wall-model (EWM) to understand its behavior for flows subjected to acceleration. So, several simulations were carried out to test the four wall-models.

The two test cases chosen are an accelerating boundary layer developing over a flat plate and flow through a converging-diverging channel. The simplicity in setting up the computational domains, having relevant flow dynamics, and most importantly, the availability of experimental or DNS data weight in the choice of these test cases. The first case considered here has an accelerating region followed by a recovery region in which the acceleration is cut-off. However, flow through the converging-diverging channel has an accelerating region followed by a decelerating region and finally a short recovery region where the flow tends to stabilize again. The channel flow shows a slight separation region on the lower wall and is on the verge of separation on the upper wall. Due to the multitude of physics involved, these flows are considered indispensable to understand the potential of the various wall-models used in this work.

Section 5.1 presents the accelerating boundary layer flow, whereas section 5.2 is devoted to the converging-diverging channel flow. The accelerating boundary layer case description and computational setup are described in section 5.1.1 followed by the discussion of results in section 5.1.2. Whereas for the converging-diverging channel flow, they are discussed in sections 5.2.1 and 5.2.2, respectively.

5.1 Spatially Developing, Accelerating Boundary Layers

5.1.1 Case Description and Setup

The chosen simulation is a quasi-incompressible flow with a Mach number of 0.1 and a Reynold number based on boundary layer thickness, $Re_{\delta_i} = 5990$. This Re_{δ_i} corresponds to a Reynold number based on the momentum thickness at the inlet, $Re_{\theta_i} = 737$, to match the simulations of Piomelli and Yuan [112] and experiments of Warnack and Fernholz [113]. The flow is subjected to acceleration such that the acceleration parameter, K defined as

$$K = \frac{1}{Re_{ref}} \frac{\nu}{U_\infty^2} \frac{dU_\infty}{dx}, \tag{5.1}$$

is over the critical value of 3×10^{-6} for an extended region. For $K > 2 - 3 \times 10^{-6}$, the flow begins to relaminarize and eventually the turbulence is damped out [114–116]. Under these conditions, the mean velocity profile and skin friction approach laminar values.

A single superblock resembling a parallelepiped is used to construct the domain. The reference parameters used in the simulations for length and velocity scaling are as follows: the boundary layer thickness, $\delta_{99,i}$ and freestream velocity, U_∞ at the inlet. The domain lengths used are given in table 5.1. Three different grids are used to test the current case and the domain used for the coarse grid extends slightly longer in the streamwise direction than that of the other two grids. The reason for having different lengths is explained shortly. The redevelopment region extends $12\delta_{99,i}$ from the inflow and is chosen as the reference location in the current simulations during the post-processing of results. This is done to scale the present results with the simulation and experimental data that are available. A sponge zone extending for $2.5\delta_{99,i}$ is also specified near the outflow. The grids utilize a uniform spacing in the streamwise and spanwise directions which are same in all three grids. The uniform spacing used follows the recommendation of Aikens [45]. It prescribes a grid spacing of at least $0.1\delta_{99}$ in the streamwise and spanwise directions for wall-modeled

Table 5.1. Grid information for various grids used in the accelerating boundary layer simulations.

Grid	**Domain Size** $(\delta_{99,i})$	$N_x \times N_y \times N_z$	$\Delta x = \Delta z$ $(\delta_{99,i})$	Δy $(\delta_{99,i})$	$\Delta x^+ = \Delta z^+$	Δy^+
Coarse	$113 \times 4 \times 4$	$2235 \times 60 \times 80$	0.05	0.05	14-42	14 - 42 43-126 (MP)
Moderate	$108 \times 4 \times 4$	$2135 \times 120 \times 80$	0.05	0.025	14-42	7 - 21 43-128 (MP)
Fine	$108 \times 4 \times 4$	$2135 \times 180 \times 80$	0.05	0.01	14 - 41	3 - 8 43 - 115 (MP)

LES. The grid spacing used in the streamwise direction is also slightly finer than the streamwise spacing used in the wall-resolved LES of Piomelli and Yuan [112]. This is to ensure that the coarse grid has an aspect ratio close to 1 in the entire domain. The grids are refined only in the wall-normal direction to test the sensitivity of the wall-models to the wall-normal spacing. The wall-normal grid refinement studies help to reduce numerical and subgrid modeling errors and thereby improve results of the wall-modeled LES [38]. Such studies are carried out either by fixing the matching point height and refining the grid in the wall-normal direction or by fixing the grid size and increasing the matching point height. The grid spacing is kept uniform in the boundary layer at the inlet and stretched out smoothly thereafter. The total grid size (in millions) comes out to be 10.7, 20.4 and 30.7 for the coarse, moderate, and fine grids respectively. Table 5.1 also shows the number of grid points, grid spacing near the wall, and grid spacing in wall units at the beginning and end of the domain in all three directions. The grid spacing in wall units at the matching point location is also given in the table. The matching point values correspond to the third, sixth, and fifteenth grid point from the wall for the coarse, moderate, and fine grids respectively.

The boundary conditions utilized are as follows. At the inflow, the digital filter-based turbulent boundary condition [16] is used with the velocity profile represented by equation 4.1. The normal Reynolds stresses and Reynolds shear stress from Spalarat's DNS data for $Re_\theta = 670$ [109] are also used at the inflow. It should be noted that for the initial cases simulated using the EWM wall-model, Townsend's laws [117] for normal Reynolds stresses, and Reynolds shear stress from Spalarat's DNS data for $Re_\theta = 300$ [109] are used. Since no data are available regarding the integral length scales at the current simulation Reynolds number, following Dhamankar [48] and Dhamankar et al. [16], the integral length scales in the streamwise direction are set to approximately $0.8\delta_{99,i}$, whereas $0.2\delta_{99,i}$ is used in both the spanwise and wall-normal directions. Although the specified length scales are not physical for the current flow conditions, earlier studies [16, 48] of a quasi-incompressible flat plate boundary layer showed that the length scales specified at the inlet have a negligible impact on the

downstream flow when the Reynolds number is high ($Re_\theta > 1000$). For the current simulations, the Reynolds number (Re_θ) is close to 1000 near the inflow. Therefore, the length scales are chosen as in the references [16,48]. Periodic boundary conditions are used in the spanwise direction. Tam and Dong's [85,86] outflow boundary condition is specified at the downstream end of the domain, and a wall-model is applied to the bottom wall.

Following Piomelli et al. [118], at the top surface, a variable freestream velocity is imposed as

$$U_{des} = 1 + \frac{\beta}{4}\left[1 + \tanh[\alpha(x - x_0)]\right]. \tag{5.2}$$

The values of the parameters α, β and x_0 used in the LES simulations of Piomelli and Yuan [112] are not provided. The parameters x and x_0 are scaled with the displacement thickness at the reference location used in their simulations. For the current simulations, the parameters α, β and x_0 were altered using a trial and error approach to match the freestream velocity profile given in [112]. But to do that, first, the displacement thickness, δ^*_{dev} at the end of the redevelopment region $x = 12\delta_{99i}$ from the current simulations is needed. The parameter δ^*_{dev} is required in order to scale x in equation 5.2, which can then be used for the trial and error process. This way, the velocity profile imposed on the top boundary can be matched with that used by Piomelli and Yuan [112] in their simulations. Therefore, a separate set of numerical simulations were carried out to determine the displacement thickness at the end of the redevelopment region, which is used to find the unknown parameters in equation 5.2. The displacement thickness obtained at the end of redevelopment region varies with the grid resolution used. So, a total of three precursor simulations were carried out to estimate the parameters α, β and x_0 in equation 5.2. Table 5.2 shows the values of the parameters used for each grid type. The precursor simulations ran using the moderate and fine grids produced the same δ^*_{dev}. Therefore, the values of the parameters in equation 5.2 are identical for both the moderate and fine grids.

Table 5.2. Value of parameters in equation 5.2 used for various grids in the accelerating boundary layer simulations.

Grid	$\boldsymbol{\alpha}$	$\boldsymbol{\beta}$	$\boldsymbol{\delta^*_{dev}}$	$\boldsymbol{x_0}$
Coarse	0.0165	3.75	0.2282	302
Moderate	0.0165	3.75	0.2155	305
Fine	0.0165	3.75	0.2155	305

Along with the streamwise velocity given by equation 5.2, the integrated mass conservation equation proposed by Lund [81] is used to specify the wall-normal velocity component, which is given as

$$V_\infty(x) = U_{des}\frac{d\delta^*}{dx} + (\delta^* - h)\frac{dU_{des}}{dx}, \tag{5.3}$$

where h is the domain height and δ^* is the local displacement thickness. The vertical velocity component provides the added mass required to accelerate the fluid in the streamwise direction. Initially, the compact schemes described in section 2.2.1 were used for computing the derivative of the displacement thickness. But the compact schemes were found to produce huge oscillations in the calculated wall-normal velocity component and caused the simulations to fail. So, the derivative scheme of the displacement thickness was modified to use an explicit second-order central scheme, which produces stable results.

Time settings that are used in the simulations are shown in table 5.3. The times shown in the table are in terms of the reference time $T = \delta_{99,i}/U_\infty$. After the initial transient period, the simulations were run for an additional $500T$ to collect the flow statistics. The simulations were performed on both the Rice supercomputer of RCAC and Stampede supercomputer of TACC.

A total of eight accelerating boundary layer simulations were carried out by varying the grid resolution, wall-model and location of the matching point used by the wall-model. The details of the cases are given in table 5.4. The wall-normal grid

Table 5.3. Time settings used in the accelerating boundary layer simulations.

Grid	**Coarse**	**Moderate**	**Fine**
Time step size, Δt (T)	3.5×10^{-3}	2×10^{-3}	1×10^{-3}
Transient period (T)	620	600	350
Transient time steps	177,000	300,000	350,000
Statistics gathering period (T)	500	500	500
Statistics gathering period time steps	143,000	250,000	500,000
Max CFL numbers (x, y, z)	(0.93, 0.78, 0.8)	(0.53, 0.87, 0.45)	(0.26, 1.07, 0.22)

refinement studies are completed by simulating three cases (*A_C_EWM*, *A_M_EWM*, and *A_F_EWM*) using the grids with different resolutions, but all using the EWM wall-model. The matching point is chosen such that its height from the wall is approximately the same in all the three cases. Next, the newly implemented wall-models are tested using the grid with moderate resolution. These cases are referred as *A_M_GEWM*, *A_M_GNEWM* and *A_M_IWM*. As with the *A_M_EWM* case, the sixth point from the wall is chosen as the matching point location when testing cases with the new wall-models. Finally, to test the impact of the matching point location that is chosen, an additional two cases similar to the *A_M_GEWM* case were performed (*A_M_GEWM_3MP* and *A_M_GEWM_4MP*) that use the third and fourth point from the wall as the matching point, respectively.

5.1.2 Discussion of the Results

This section presents the results obtained using the current wall-modeled simulations and comparisons are made with the reference data. The wall-resolved LES

Table 5.4. Simulation settings for various accelerating boundary layer cases.

Case Name	**Grid**	**Wall Model**	**Matching Point Location**
A_C_EWM	Coarse	EWM	3
A_M_EWM	Moderate	EWM	6
A_F_EWM	Fine	EWM	15
A_M_GEWM	Moderate	GEWM	6
A_M_GNEWM	Moderate	GNEWM	6
A_M_IWM	Moderate	IWM	6
A_M_GEWM_3MP	Moderate	GEWM	3
A_M_GEWM_4MP	Moderate	GEWM	4

simulations of Piomelli and Yuan [112] and experiments of Warnack and Fernholz [113] are used as the reference data for validation of the current wall-modeled simulations of the accelerating boundary layer. First, a wall-normal grid independence study is performed by comparing the results of the *A_C_EWM*, *A_M_EWM* and *A_F_EWM* cases with the reference data. It is then followed by the assessment of the wall-models by comparing the *A_M_EWM*, *A_M_GEWM*, *A_M_GNEWM* and *A_M_IWM* cases with the reference data. Finally, the reference data are compared with *A_M_GEWM_3MP*, *A_M_GEWM_4MP*, and *A_M_GEWM* to analyze the impact of the location of the matching point.

The flow quantities presented in this section are both time-averaged, as well as averaged in the spanwise direction, z. The streamwise velocity profile imposed on the top boundary for all the cases simulated here is plotted in figure 5.1. The velocity increases almost by three times towards the end of the domain. Figures 5.2 and 5.3 show the contours of mean streamwise and wall-normal velocity components in part of the domain. The boundary condition imposed on the top surface accelerates the flow in the streamwise direction with a relatively low wall-normal velocity. The

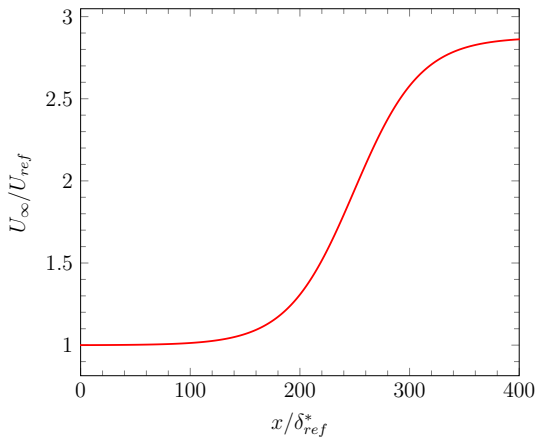

Figure 5.1. Free stream velocity imposed on the top boundary for the accelerating boundary layer simulations.

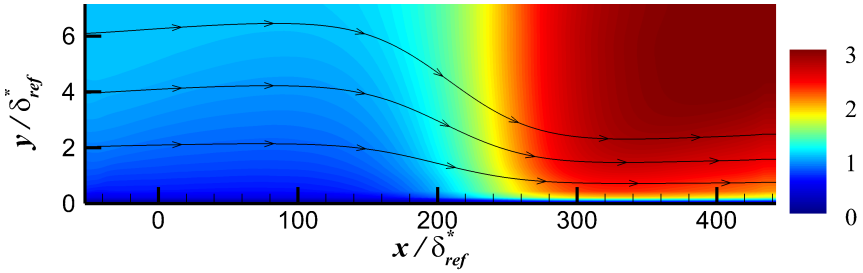

Figure 5.2. Streamwise velocity contour for the accelerating boundary layer (Case *A_C_EWM*).

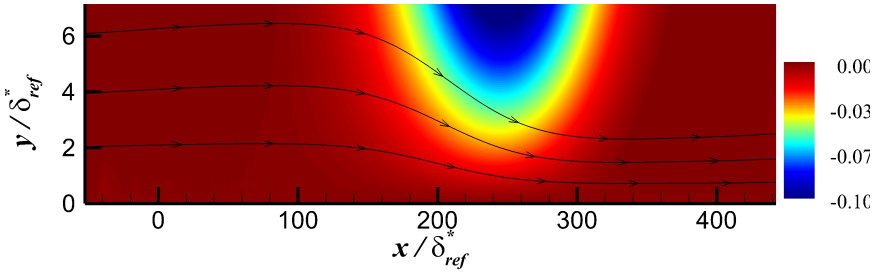

Figure 5.3. Wall-normal velocity contour for the accelerating boundary layer (Case *A_C_EWM*).

streamlines shown in the contour show the thinning of the boundary layer as the flow accelerates downstream.

Assessment of the Wall-Normal Grid Resolution

Various boundary layer parameters are shown in figure 5.4. The current results are compared with the matching wall-resolved LES [112] and experiment [119]. The acceleration parameter, K exceeds the critical value 3×10^{-6} for an extended length near the middle of the domain until the acceleration is reduced towards the end of the domain, where the velocity becomes constant again. Near the peak of the acceleration parameter, the results of the A_C_EWM case varies slightly when compared with the other two cases simulated here. Otherwise, all the grids utilized produce similar values of the acceleration parameter and the results compare well with the reference data. It can be concluded that the grid resolution has very little influence on the acceleration parameter.

The Reynolds number based on momentum thickness, Re_θ, shown in figure 5.4(b), first increases and begins to decrease as the value of K increases. Re_θ then attains the lowest value at a location somewhat downstream of where K reaches its peak value. There is a lag effect where it takes time for Re_θ to respond to the changes in K. As the value of K decreases, the Re_θ value begins to increase again. It should be noted that at all the downstream locations ($x/\delta^*_{ref} > 0$), the wall-resolved simulation of Piomelli and Yuan [112] underpredicts Re_θ in comparison with the experiment. At the reference location ($x/\delta^*_{ref} = 0$), the values of Re_θ for all the cases match well with the available data. But as the flow develops downstream, Re_θ is overpredicted when utilizing the coarse or moderate grid. In fact, the results predicted when utilizing the coarser mesh are much higher than the moderate grid results. Re_θ obtained for the fine grid case compares fairly well with the experimental data. Overall, Re_θ is very sensitive to the grid resolution that is used and the quality of results increases with grid resolution. Re_θ responds quickly to the changes occurring in the outer layer, here driven by the pressure gradient.

The response of the skin friction coefficient, $C_f = \tau_w / \frac{1}{2}\rho U_\infty^2$, is slower than the Re_θ. It is plotted in figure 5.4(c). For the current wall-modeled simulations, C_f is

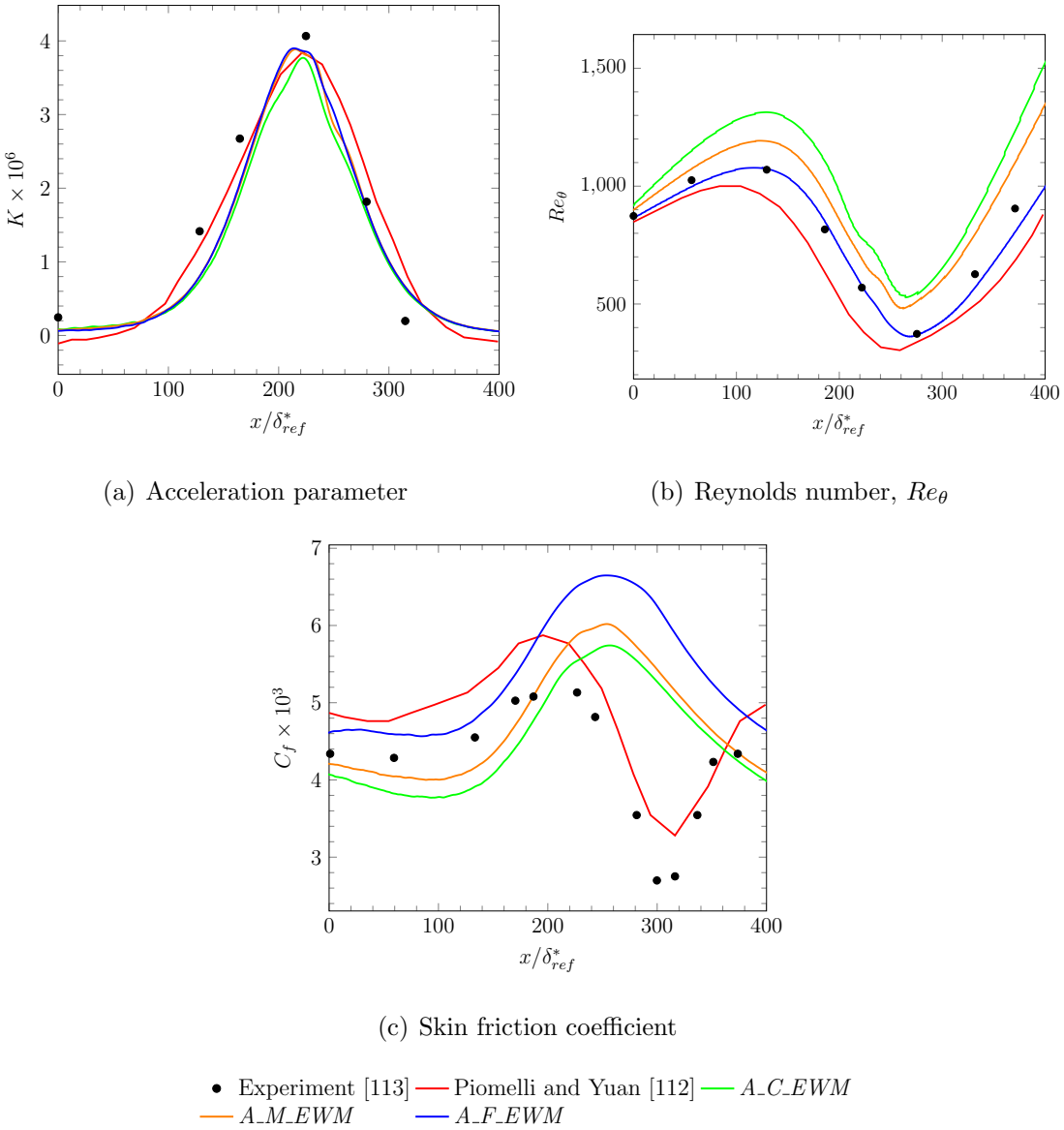

(a) Acceleration parameter

(b) Reynolds number, Re_θ

(c) Skin friction coefficient

Figure 5.4. Comparison of boundary layer parameters of the wall-modeled accelerating boundary layer simulations using three grid resolutions with data from the experiment of Warnack and Fernholz [113] and the wall-resolved LES simulation of Piomelli and Yuan [112]. The EWM wall-model is used in all three wall-modeled cases compared here.

computed using the value of u_τ obtained by solving the equations corresponding to the wall-models. The experimental data show that C_f does not decreases until K reaches its peak. C_f then beings to decrease until the freestream velocity becomes constant, at which point, C_f attains its minimum value before recovering. The wall-resolved simulation of Piomelli and Yuan also follows the trend seen in the experiment. However, this trend is not observed in the current wall-modeled simulations. In comparison with the experiments, the wall-resolved simulation of Piomelli and Yuan overpredicts the skin friction at most locations. For $x \leq 200\delta^*_{ref}$, the skin friction is underpredicted for the cases utilizing the coarse or moderate grid, but overpredicted for the case utilizing the fine grid. For $x > 200\delta^*_{ref}$, all the grids produce overpredicted results when comparing with the experimental data, especially near the region where the experimental data has the lowest value of C_f. Although there are some discrepancies in C_f between the current simulations and the reference data in the region where the pressure gradient is zero, the results of the current simulations become worse in the acceleration region. It appears that the EWM utilized here does not respond well to the outer layer changes as the formulation does not account for pressure gradients. Like Re_θ, the skin friction is very sensitive to the utilized grid resolution. But it can be noticed that the values of Re_θ are overpredicted when a coarse grid is used and become better with grid resolution, whereas the skin friction trends are reversed.

Next, the mean velocity profiles in wall units are shown in figure 5.5 at various cross-sections. In the figure, the streamwise location increases from bottom to top. The profiles on top are shifted up by 20 units from the bottom ones for clarity. The reference data, current simulations results along with the logarithmic law are plotted. The logarithmic law is given as $u^+ = \frac{1}{0.41} \ln y^+ + 5$. The current simulations follow the logarithmic law from the inflow until the end of the domain, whereas the reference data follows the logarithmic law in the region where the flow is not accelerating, i.e., for $x/\delta^*_{ref} = 0$, 166 and 371. The EWM forces the mean velocity profile to match the logarithmic law at the matching point. This could be the cause for the mean velocity profiles of cases using the EWM not matching the reference data. In the

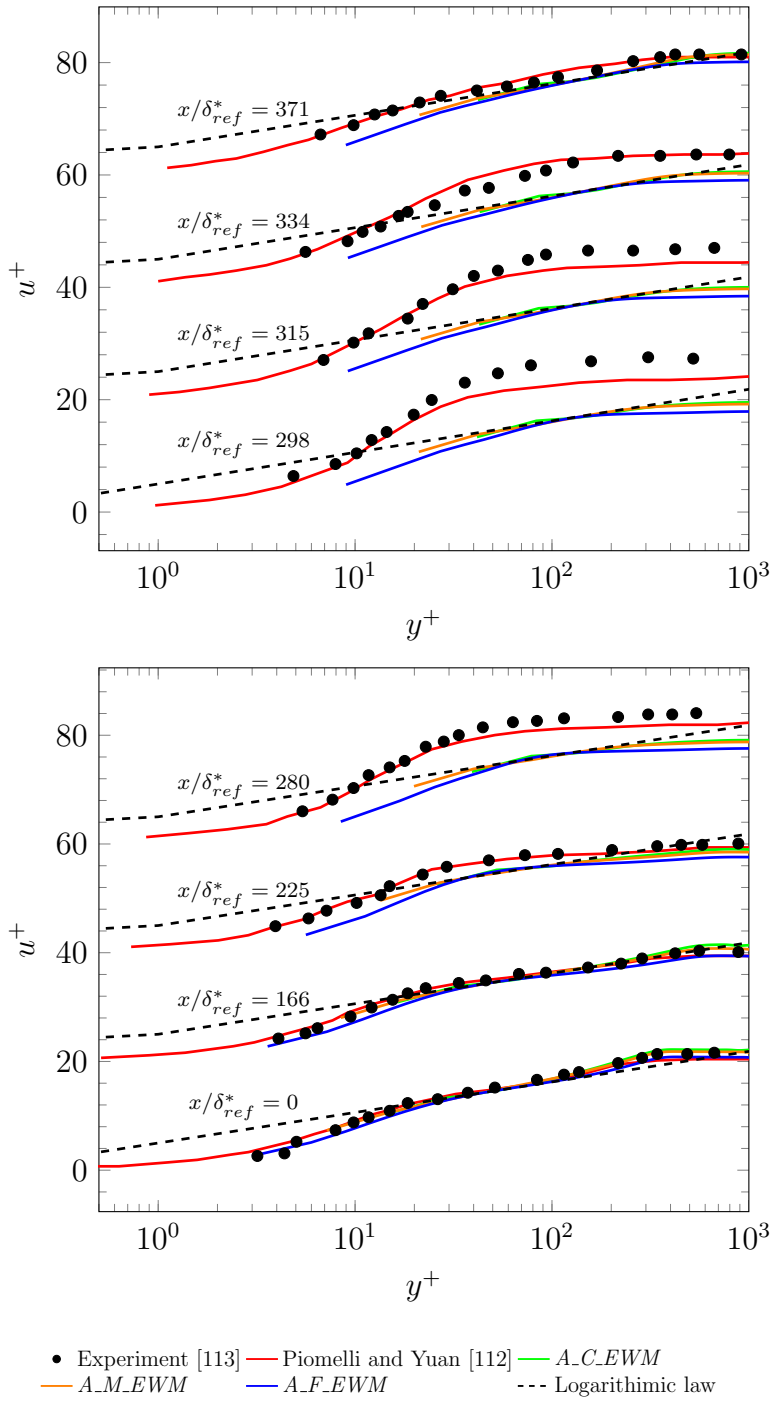

Figure 5.5. Comparison of mean velocity profiles in wall units at various streamwise locations of the wall-modeled accelerating boundary layer simulations using three grid resolutions with data from the experiment of Warnack and Fernholz [113] and the wall-resolved LES simulation of Piomelli and Yuan [112]. The EWM is used in all the three wall-modeled cases compared here.

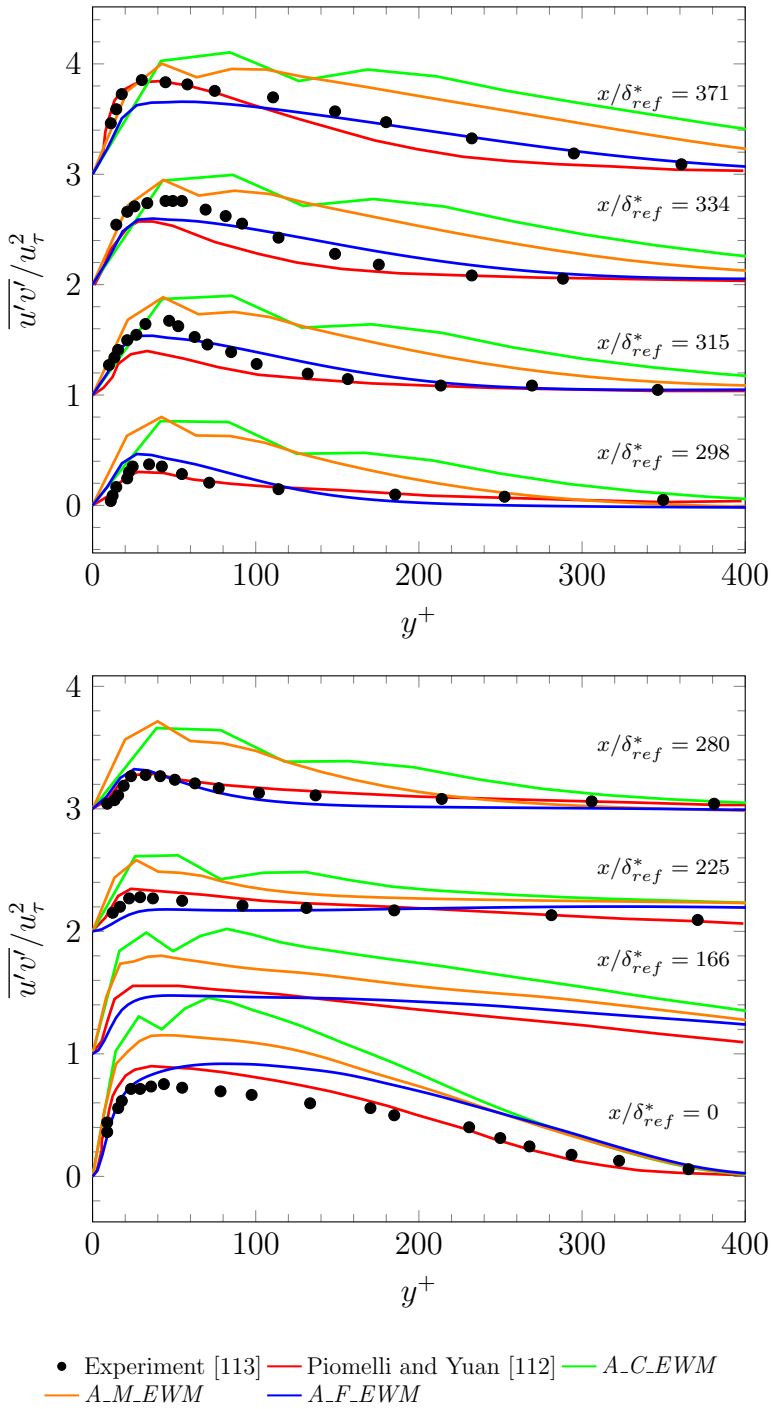

Figure 5.6. Comparison of shear stress profiles in wall units at various streamwise locations of the wall-modeled accelerating boundary layer simulations using three grid resolutions with data from the experiment of Warnack and Fernholz [113] and the wall-resolved LES simulation of Piomelli and Yuan [112]. The EWM is used in all the three wall-modeled cases compared here.

acceleration region, the reference data show a laminar-like behavior with an extended linear region and profiles above the logarithmic law. The reference data deviate from the logarithmic law at $x/\delta^*_{ref} = 225$, where K peaks and is greater than the critical value of 3×10^{-6}. Before $x/\delta^*_{ref} = 225$, the value of K is already greater than the critical value for some distance before the mean velocity of the reference data deviates from the log law. The mean velocity profiles do not come back down to the log law until $x/\delta^*_{ref} = 371$, which corresponds to the end of the accelerating region, where $K \approx 0.2 \times 10^{-6}$. Although K drops below the critical value, the flow does not return to the expected turbulent profile until much further downstream. There is a strong non-equilibrium effect where it takes a long time for the turbulent boundary layer to recover from the effects of the acceleration. This history effect is not captured by the wall models. The discrepancies noticed in the mean velocity profiles reflect the behavior of the skin-friction noticed in figure 5.4(c) for the current wall-modeled simulations. The high skin-friction predicted by the wall-model in the current simulations causes the u^+ values to fall below the reference data. The mean velocity results did not show any significant changes with the grid resolutions used in the current study.

Similarly to the mean velocity profiles, the shear stress profiles in wall units are also plotted in figure 5.6 at various cross-stream locations. The profiles on top are shifted up by 1 unit from the bottom ones for clarity. The reference data show that the shear stress, initially high at $x = 0$, decreases in the region of acceleration before recovering to the initial levels towards the end of the domain. Qualitatively, the current wall-modeled simulations show these trends as well. But the results are overpredicted for cases utilizing a coarse or moderate grid. The *A_F_EWM* case utilizing the fine grid compares reasonably well with the experiments. As can be seen in the results, it appears that a good grid resolution is required to capture the shear stress accurately. The results become better with increasing grid resolution. The Reynolds stresses specified at the inflow could also be a factor for the higher levels of shear stress noticed here. As mentioned earlier, Townsend's laws [117] and Reynolds

shear stress from Spalarat's DNS data for $Re_\theta = 300$ [109] are used at the inflow for the EWM cases discussed here. To check its impact on the results, cases using a wall-model other than the EWM are simulated by utilizing the Reynolds stresses at $Re_{\theta_i} = 670$ available from the literature [109]. This Reynolds number is close to the Reynolds number used in the current simulations. The results of cases using the Reynolds stresses at $Re_{\theta_i} = 670$ are discussed in the next section.

Using the skin-friction coefficient, which is a crucial boundary layer parameter, the following conclusions can be drawn in assessing the grid quality. The results are susceptible to the refinement of the grid in the wall-normal direction. Although differences exist with the reference data, the current wall-modeled simulations utilizing any of the three grids show similar behavior. Refining the grid did not improve the mean velocity prediction as the wall-model is unable to impose the right boundary conditions taking the pressure gradient effects into consideration. Although the fine grid does a better job of capturing the shear stress, the moderate grid also seems to capture the trend reasonably well and is more economical than the fine grid. Therefore, the moderate grid will be used to limit the number of simulations while testing different wall-models for determining their performance in the accelerating region. It is unclear why the skin-friction increases in the wall-modeled cases with grid refinement and further analysis would be needed to better understand this behavior. The effect of the Reynolds stresses specified at the inflow is revisited for further analysis in the next section. The results of wall-modeled simulations utilizing different wall-models on a moderate grid are presented next.

Assessment of the Wall Models

This section deals with the impact of the various wall models used in the simulations of the accelerating boundary layer. For this purpose, similar to the previous section, the boundary layer parameters along with the mean velocity and shear stress profiles at various cross-sections are analyzed by comparing the *A_M_EWM*,

A_M_GEWM, *A_M_GNEWM* and *A_M_IWM* cases with the reference data. The moderate grid is used in all the current cases compared here.

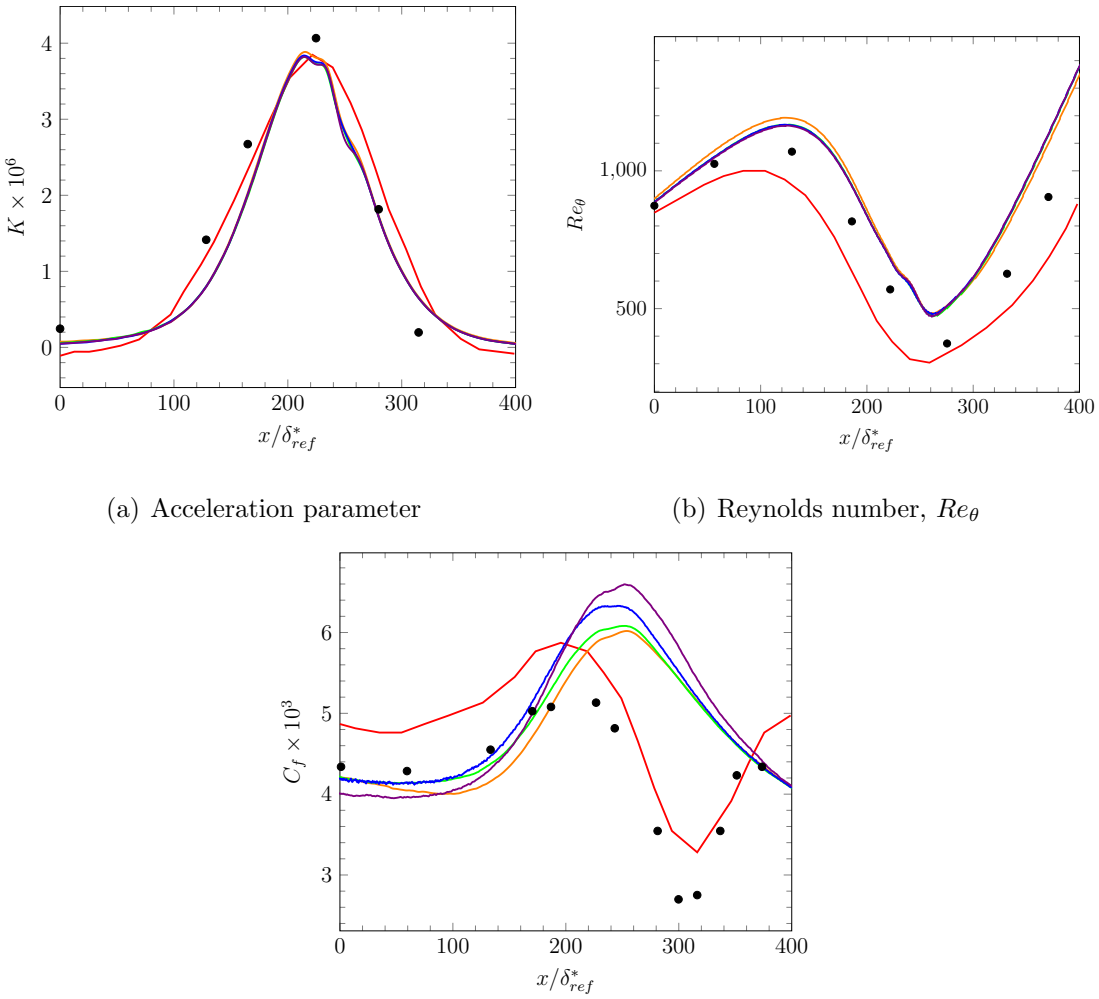

(a) Acceleration parameter

(b) Reynolds number, Re_θ

(c) Skin friction coefficient

Figure 5.7. Comparison of boundary layer parameters of the wall-modeled accelerating boundary layer simulations using four wall-models with data from the experiment of Warnack and Fernholz [113] and the wall-resolved simulation of Piomelli and Yuan [112]. The moderate grid is used in all four wall-modeled cases compared here.

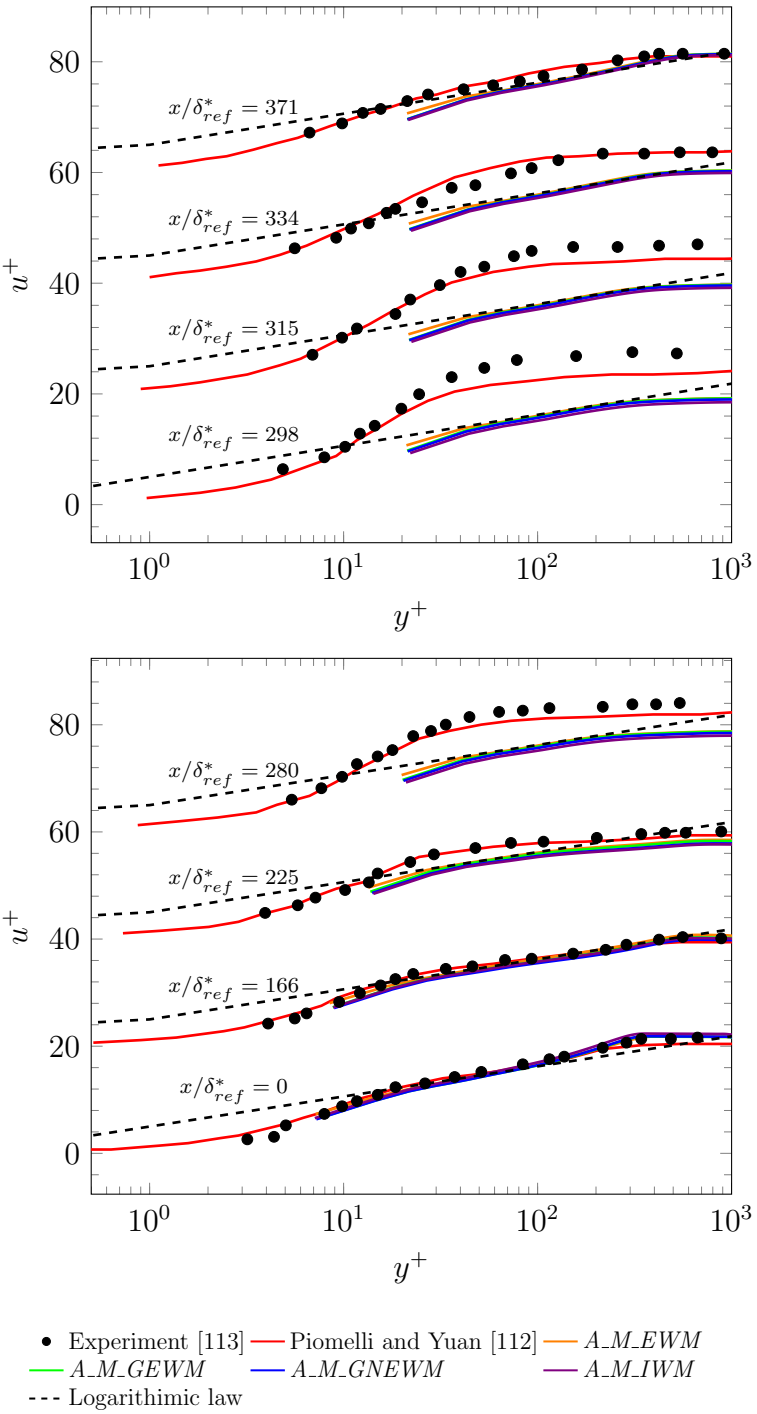

Figure 5.8. Comparison of mean velocity profiles in wall units at various streamwise locations of the wall-modeled accelerating boundary layer simulations using four wall-models with data from the experiment of Warnack and Fernholz [113] and the wall-resolved simulation of Piomelli and Yuan [112]. The moderate grid is used in all four wall-modeled cases compared here.

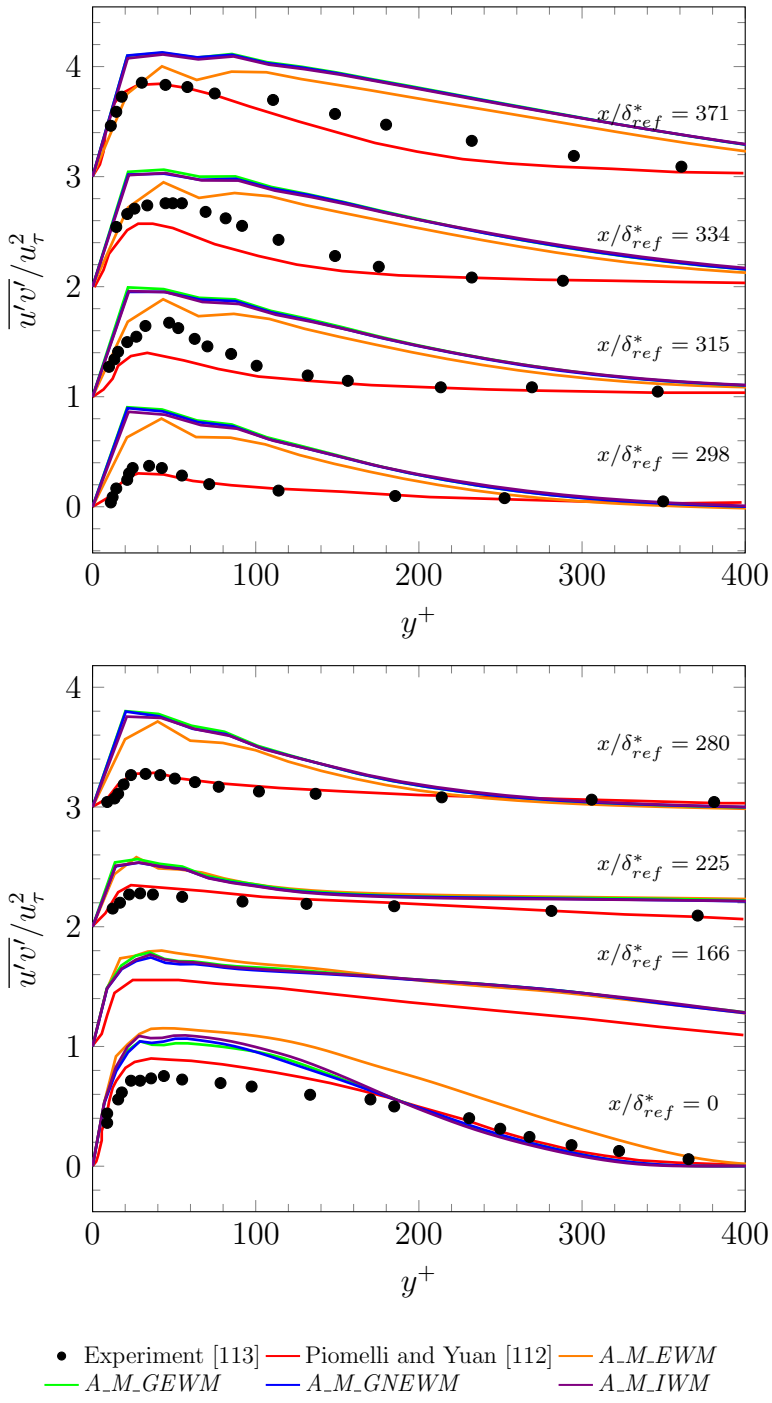

Figure 5.9. Comparison of shear stress profiles in wall units at various streamwise locations of the wall-modeled accelerating boundary layer simulations using four wall-models with data from the experiment of Warnack and Fernholz [113] and the wall-resolved simulation of Piomelli and Yuan [112]. The moderate grid is used in all four wall-modeled cases compared here.

The boundary layer parameters of the current cases plotted in figure 5.7 follow similar trends as discussed in the previous section. The wall-models utilized have very little impact on the results. The only parameter that is affected is the skin-friction coefficient plotted in figure 5.7(c). When utilizing a wall-model other than the IWM, the skin-friction is computed using the time and spanwise averaged flow quantities sampled at the matching point. Whereas for the IWM, the skin-friction is computed using the friction velocity, u_τ gathered during each time-step of the simulation's statistics phase. Nevertheless, the new wall-models are not able to capture the trend (drop in C_f) noticed in the acceleration region of the reference data. Although the wall-model formulation is similar for both EWM and GEWM, the cases *A_M_EWM* and *A_M_GEWM* utilizing those models show some differences in the results of C_f. The moderate grid used has the matching point in the log-layer. Since both EWM and GEWM follow the same mean velocity profile in the log-layer, the boundary conditions imposed by these two wall-models are the same. Therefore, the wall-model used could not be the reason for the differences noticed in C_f between the *A_M_EWM* and *A_M_GEWM* cases. The case *A_M_GEWM* was simulated using an updated version of the code that extends the transformations of Sondak and Pletcher [105] to handle non-orthogonal grids. However, the grids used in the current simulations are orthogonal in the wall-normal direction. So, the changes made to the tensor transformations are expected not to have any impact on the results. Therefore, the only possible cause for the differences noticed in C_f between the two cases could be due to the use of different Reynolds stresses that are imposed at the inflow. The Reynolds shear stress and normal Reynolds stresses from Spalarat's DNS data for $Re_\theta = 670$ [109] are used for the case using the GEWM wall-model. The cases *A_M_GNEWM* and *A_M_IWM* also use similar settings and the same version of the code as used by the *A_M_GEWM* case. The C_f of the *A_M_GNEWM* case matches well with the *A_M_GEWM* case in the region where the flow is not accelerating (for $x \leq 100\delta^*_{ref}$ and $x \geq 300\delta^*_{ref}$). In the accelerating region, the *A_M_GNEWM* slightly deviates from the results of the *A_M_GEWM* case. This is because of the non-equilibrium

effects that are embedded into the formulation of the GNEWM. However, the C_f of the *A_M_GNEWM* case still do not follow the trend as seen in the reference data. Moreover, in comparison with the reference data, the results of the *A_M_GNEWM* case deteriorate further than the *A_M_GEWM* case. For the case utilizing the IWM, the skin friction is underpredicted for $x \leq 200\delta^*_{ref}$ and overpredicted after that in comparison with the case utilizing GEWM wall-model.

With only minor differences noticed in C_f, it is expected that the results of the mean velocity and Reynolds shear stress will not be varied much. These profiles are plotted in figures 5.8 and 5.9 respectively. Again, the trends for the current cases are similar to what was discussed in the previous section. Hardly any difference can be noticed in the profiles of the mean velocity. But the Reynolds shear stress varies slightly for the case using EWM in comparison with the other cases simulated here. This could be due to the differences in stresses imposed at the inflow as mentioned earlier. The imposed stresses did not help in making the results better for cases utilizing GEWM, GNEWM, and IWM wall-models. These cases show higher levels of shear stress in comparison with the case utilizing EWM as the flow propagates downstream.

From the results in this section, it can be concluded that the more complex wall-models which account for non-equilibrium effects are not competent enough to capture the correct trends. It could be possible that the relatively low Reynolds number of the flow might have constrained the contribution of the non-equilibrium effects in the GNEWM and IWM wall-models. However, among the wall-models used, the GEWM seems to predict the results better.

Assessment of the Matching Point Location

Unlike the traditional practice of choosing the first grid point off the wall from which the LES data are sampled to be used by the wall-model, as mentioned earlier, the LES data are sampled from a point higher than the first grid point. During the

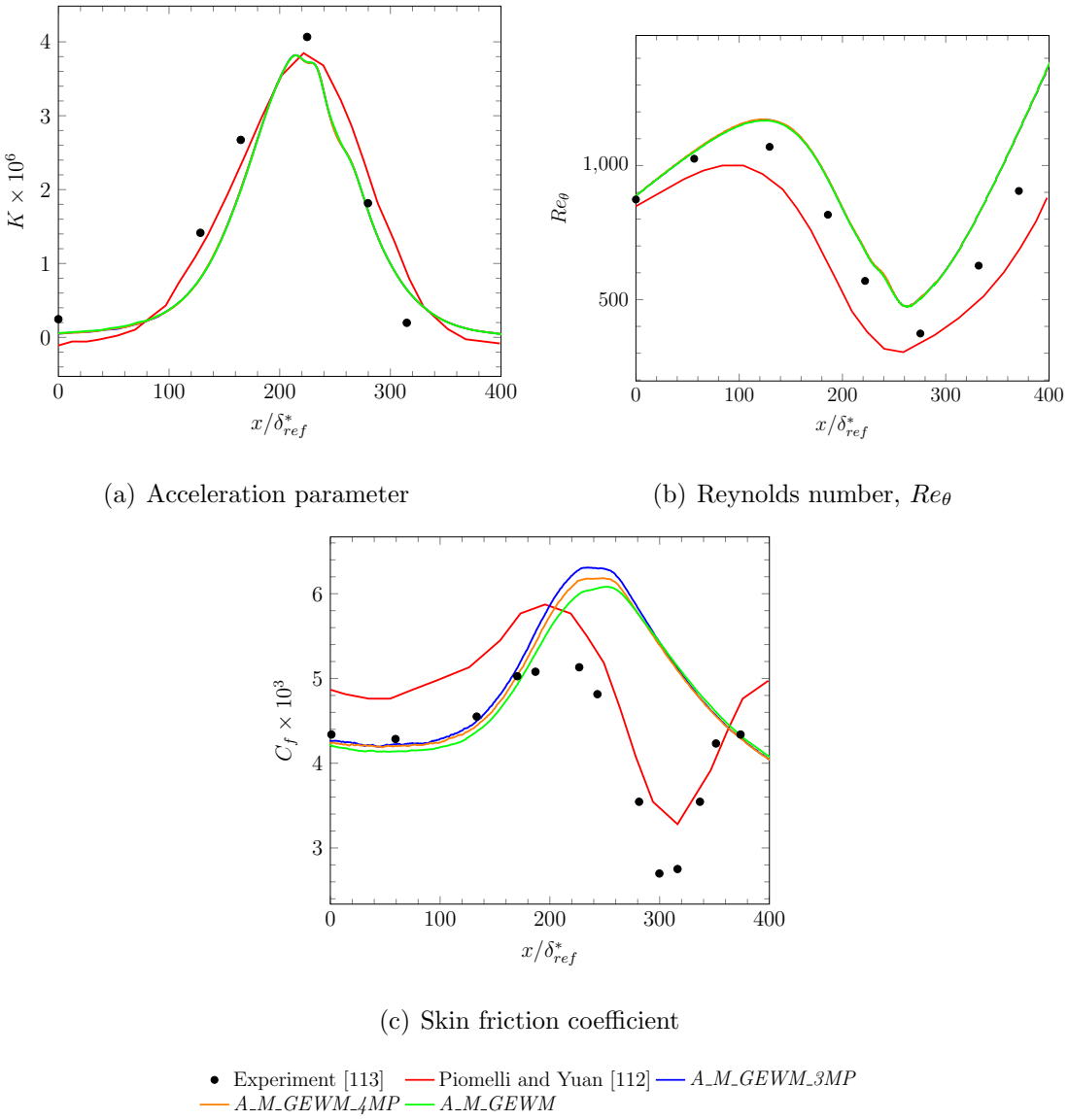

(a) Acceleration parameter

(b) Reynolds number, Re_θ

(c) Skin friction coefficient

Figure 5.10. Comparison of boundary layer parameters of the wall-modeled accelerating boundary layer simulations using the GEWM and different matching point locations with data from the experiment of Warnack and Fernholz [113] and the wall-resolved simulation of Piomelli and Yuan [112].

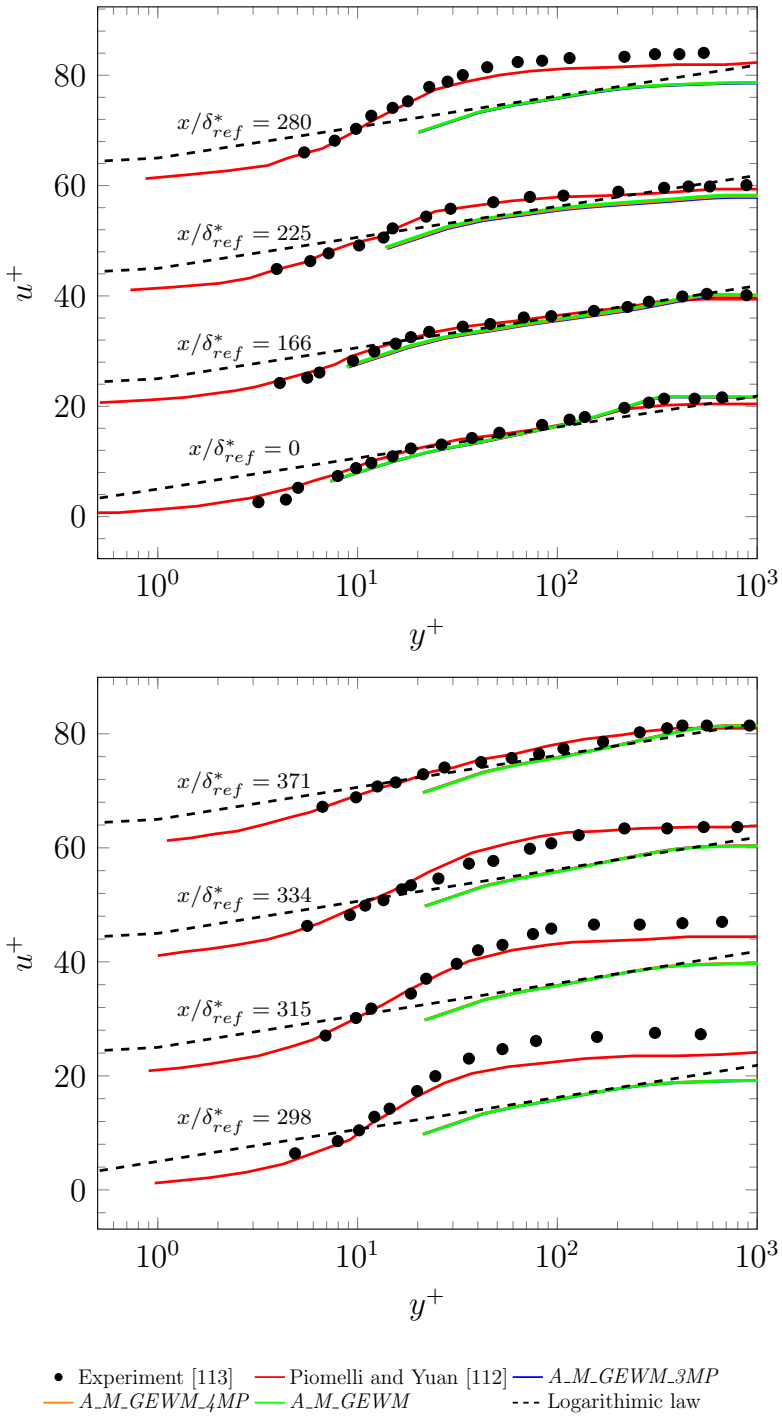

Figure 5.11. Comparison of mean velocity profiles in wall units at various streamwise locations of the wall-modeled accelerating boundary layer simulations using the GEWM and with different matching point locations with data from the experiment of Warnack and Fernholz [113] and the wall-resolved simulation of Piomelli and Yuan [112].

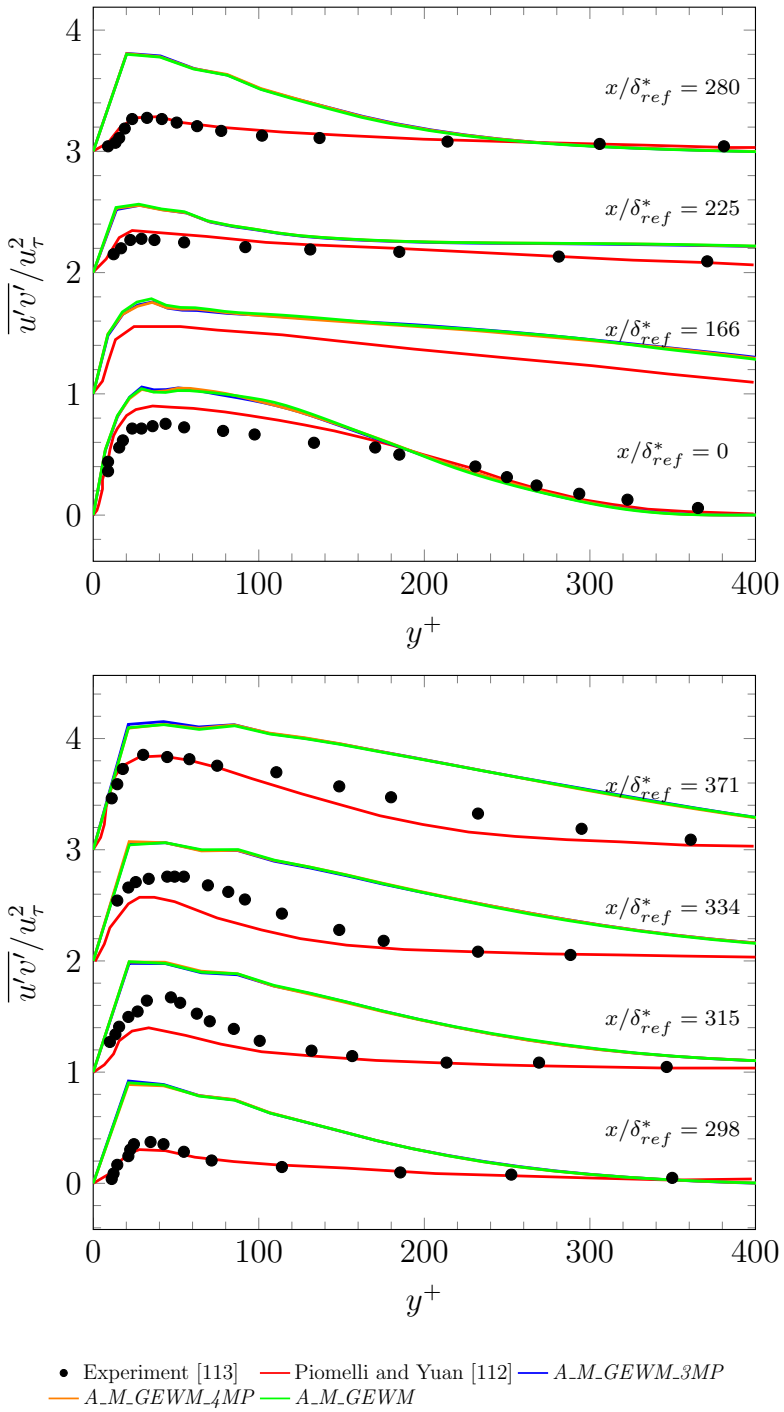

Figure 5.12. Comparison of shear-stress profiles in wall units at various streamwise locations of the wall-modeled accelerating boundary layer simulations using the GEWM and with different matching point locations with data from the experiment of Warnack and Fernholz [113] and the wall-resolved simulation of Piomelli and Yuan [112].

grid refinement study, the matching point is chosen such that its location is approximately the same between the grids used which resulted in selecting the sixth point from the wall as the matching point when using the moderate grid. The matching point is higher than what Aikens [45] has suggested based on the simulations of incompressible and compressible flat plate spatially developing boundary layers. So, it is worthwhile to analyze how the matching point location impacts the current simulations of the accelerating boundary layer. As the GEWM seems to perform better than the other two wall models, it is chosen to study the impact of the matching point. Two additional cases were simulated by selecting the third and fourth point from the wall as the matching point. These cases are referred to as *A_M_GEWM_3MP*, *A_M_GEWM_4MP* respectively and compared with the *A_M_GEWM* case to study the effect of the matching point in this section.

As in the previous sections, similar comparisons are made here and plotted in figures 5.10 to 5.12. Although only small differences are noticed, they are shown here for the sake of completeness. The only considerable difference that can be discerned is for the skin-friction coefficient. But again the differences are so small that it does not affect the mean velocity or shear stress results. So, it can be concluded that the results are independent of the matching point location utilized in the current simulations.

5.1.3 Summary and Conclusions

The simulations of accelerating boundary layers have been completed to validate and analyze the wall-models that were added to the modular-LES code. A total of eight simulations were performed to understand the behavior of the wall-models, grid quality, and matching point location for flow subjected to acceleration. The following conclusions can be drawn from the analyses of the accelerating boundary layer.

The outer region of the flow is more sensitive to the pressure gradient than the inner region. The skin-friction coefficient, which is a parameter in the inner region, is

predicted reasonably well by the wall-models in the non-accelerating region. However, the wall-models do not perform well in the accelerating region. The mean velocity follows the logarithmic law at all the locations contradicting the reference data. The reference data show laminar-like profiles in the acceleration region. The Reynolds shear stress agrees qualitatively with the reference data. Utilizing any of the three grids shows similar observations. The boundary layer parameters and the Reynolds shear stress improve with grid refinement. However, the mean velocity results are not affected by the grid resolution. It is worthwhile to conduct future studies to understand the sensitivity of the solution to various grid resolutions in the other two directions.

All the utilized wall-models predict similar wall shear stress. The wall-models show excellent performance in the non-accelerating region but are unable to capture the flow dynamics in the accelerating region noticed in the experiments and wall-resolved LES simulation. The non-equilibrium contributions in the GNEWM and IWM wall-models may have been suppressed due to the relatively low Reynolds number of the flow making these wall-models ineffective. So, it is worthwhile to test these wall-models for flows having higher Reynolds numbers. The wall-model simulation results are independent of the matching point locations chosen in the current simulations.

5.2 Three-dimensional flow through a Converging-Diverging Channel

5.2.1 Case Description and Setup

The second test case used for the validation of the wall-models is the flow through a converging-diverging channel. This case is developed to experimentally test the behavior of the boundary layer subjected to adverse pressure gradients and on the verge of separation [120]. This kind of flow behavior is usually encountered on the suction side of an airfoil subjected to high angles of attack during takeoff, landing, maneuver, etc. The configuration is of a typical channel flow with a bump located on the lower wall. The bump first generates a favorable pressure gradient causing

the flow to accelerate followed by an adverse pressure gradient causing the flow to decelerate. To further understand the characteristics of turbulent structures subjected to a pressure gradient, DNS of this bump configuration was carried out by Marquillie et al. [121] at a moderate Reynolds number of $Re_\tau = 395$, and by Laval [122] at $Re_\tau = 617$. Here, $Re_\tau = u_\tau h/\nu$ is the Reynolds number based on the friction velocity u_τ, h is the channel half-height and ν is the kinematic viscosity. In both simulations, on the leeward side of the bump, the flow separates from the lower wall, whereas on the upper wall, the flow is on the verge of separation. Strong coherent structures have been generated near the separation point on both the upper and lower walls. On the lower wall, small vortices are generated downstream of the separation point. These vortices convect downstream and interact with the larger vortices that are present in the outer boundary layer. At the point of flow separation, no discernible vortices are formed, and the turbulent kinetic energy is low. To test the wall-models, the simulations were run at $Re_\tau \approx 617$. This Re_τ corresponds to a Reynold number based on half channel height, $Re_h = u_{max}h/\nu = 12,600$ at the inlet, where u_{max} is the maximum velocity at the inlet. This Re_h matches the wall-modeled simulations of Chen [123] for the same case. Moreover, Chen utilized GNEWM for one of the simulations which will also make it a viable choice to validate the GNEWM wall-model formulation implemented in this work. However, Chen utilizes different numerical methods than that used in the current work. A second order finite volume method along with an immersed boundary condition is used in Chen's work. The numerical methods used have a strong effect on the simulations. Therefore, the simulations of Chen are not as useful for validation as would be desired.

A single superblock is used to construct the computational domain, which extends $14h \times 2h \times \pi h$ in the streamwise, vertical and spanwise directions. The bump is located on the lower wall and is approximately $7.82h$ long. It starts at $x \approx 1.83h$ and has a maximum height of $0.67h$ located at $x \approx 5.22h$. The simulations were performed using two grids with spatial resolutions similar to that of the wall-modeled simulations performed by Chen [123]. The coarse grid has a spatial resolution of $102 \times 48 \times 24$,

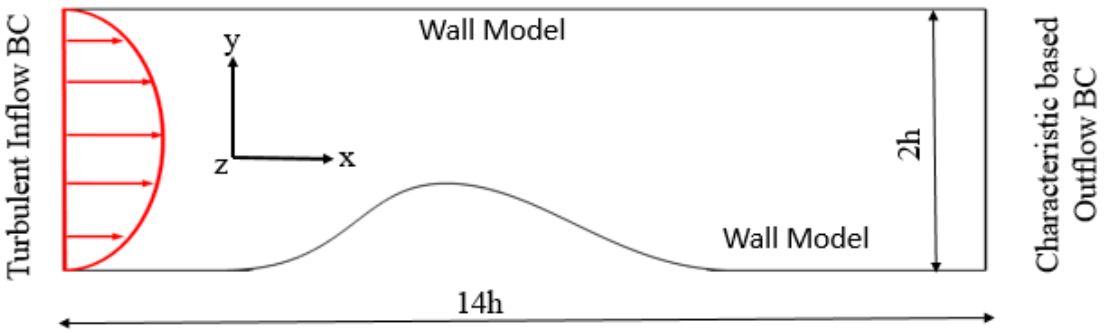

Figure 5.13. Simulation setup of the converging-diverging channel flow for wall-modeled LES.

whereas the fine grid has $200 \times 64 \times 48$. The grids are discretized uniformly in both the vertical and spanwise directions. In the streamwise direction, the spacing is uniform until $x = 12.57h$ and stretched out is smoothly after that. The grid stretching ensures the vortices are dampened out before reaching the outflow boundary. The number of grid points, as well as other simulation parameters used, are given in table 5.5. The grid spacings in wall units at the inlet, computed using the friction velocity from the DNS, are also shown for all three directions along with the wall-normal spacing in wall units at the matching point location. Table 5.5 also lists the wall model and SGS model used in each case.

The boundary conditions utilized are as follows. At the inflow, the digital filter-based turbulent boundary condition [16] is used. The velocity profiles, normal Reynolds stresses and Reynolds shear stress applied at the inflow are taken from the DNS simulation of a plane channel flow run at an equivalent Reynold number by Marquillie et al. [124]. The data are available from an online database available at [125]. Periodic boundary conditions are used in the spanwise direction. A characteristic outflow boundary condition [48] is specified at the downstream end of the domain. A wall-model is applied on both the top and bottom walls.

Table 5.5. Simulation parameters of the different converging-diverging channel flow cases.

Case	N_x	N_y	N_z	Δx^+	Δy^+	$\Delta y^+(MP)$	Δz^+	**Wall Model**	**SGS Model**
B_C_GEWM	102	48	24	82	26	53	84	*GEWM*	ILES
B_C_GNEWM	102	48	24	82	26	53	84	*GNEWM*	ILES
B_C_IWM	102	48	24	82	26	53	84	*IWM*	ILES
B_F_GEWM	200	64	48	41	20	59	41	*GEWM*	ILES
B_F_GNEWM	200	64	48	41	20	59	41	*GNEWM*	ILES
B_F_IWM	200	64	48	41	20	59	41	*IWM*	ILES
B_F_DNS	200	64	48	41	20	59	41	DNS data	ILES
B_C_DSM	102	48	24	82	26	53	84	GEWM	DSM

Table 5.6. Time settings used for the coarse and fine grid cases of the converging-diverging channel flow.

Grid	**Coarse**	**Fine**
Time step size, Δt (T)	3×10^{-3}	2×10^{-3}
Transient period (T)	240	240
Transient time steps	80,000	120,000
Statistics gathering period (T)	210	240
Statistics gathering period time steps	70,000	120,000
Total time steps	150,000	240,000
Max CFL Numbers (x, y, z)	(0.26, 1.09, 0.24)	(0.35, 0.99, 0.33)

The simulation settings, such as the time-step, number of time-steps and CFL numbers, for the converging-diverging channel are tabulated in table 5.6 for both the coarse and fine grids. The initial transients resulting from the unphysical initial conditions are removed by simulating the case for about 17 FTCs. The simulations are then continued to run further for 15 FTCs to gather statistics while using a coarse grid. This period is similar to that in the wall-modeled simulations of Chen [123] who accumulated statistics over a period of 15 FTCs and 10 FTCs on the coarse and fine grids respectively. But in the current simulations performed using the fine grid, a slightly longer period of 17 FTCs is used to gather statistics. The 15 FTCs used for collecting statistics on the coarse grid corresponds to a simulation time of $210h/u_{max}$. This requires the simulation to be run for 70,000 time-steps using a time-step of $\Delta t = 3 \times 10^{-3}$. The time-step resulted in CFL numbers of 0.26, 1.09 and 0.24 in the streamwise, vertical and spanwise directions respectively. On cases simulated using the fine grid, a smaller time-step of $\Delta t = 2 \times 10^{-3}$ is used to avoid the numerical instabilities arising due to the stringent CFL condition. The CFL numbers are 0.35, 0.99 and 0.33 in the streamwise, vertical and spanwise directions respectively, and a

total of 120,000 time-steps are used for the accumulation of statistics while using the fine grid.

5.2.2 Discussion of the Results

This section presents the results obtained using the current wall-model simulations which are compared with the DNS [122] and wall-modeled LES simulations of Chen [123]. First, the results of the coarse mesh cases are compared and analyzed with the reference data followed by the results of fine mesh cases. Next, an LES case utilizing the wall shear-stress from the DNS instead of from a wall-model is presented. Lastly, the influence of the SGS modeling strategy is analyzed by comparing the results of cases using ILES and DSM methodologies.

Coarse Grid Results

The flow quantities along the upper and lower walls are compared in figure 5.14. The skin friction coefficient, $C_f = \tau_w / \frac{1}{2}\rho u_{max}^2$ along the lower wall is shown in figure 5.14(a). The results predicted by the current wall-model cases and Chen's wall-model case differ from the results of the DNS. The major difference that can be noticed is the flow separation predicted by the DNS on the leeward side of the bump on the lower wall. None of the wall-model cases are able to predict the separation. This could be due to the low resolution of the grid, especially in the streamwise and wall-normal directions. Upstream of the bump, the results compare well with the DNS. In all the cases, the C_f attains a maximum value before the summit of the bump is reached. The *B_C_IWM* case predicts a peak value of C_f that agrees well with the DNS, while all the other cases underpredict the peak value. It can also be noticed that all the wall-modeled cases attain a peak value of C_f slightly downstream of the DNS location. Downstream of the bump, the wall-modeled cases are able to recover and attain C_f levels close to the DNS. Comparing the *B_C_GNEWM* case and Chen's wall-model case, which use the same wall-model, the current simulation results show

better prediction capabilities. Along the upper wall, the DNS results show that the flow is on the verge of separation, as can be seen from the C_f plotted along the upper wall in figure 5.14(b). The DNS results show similar trends as seen on the lower wall. The peak C_f occurs at the same location as that on the lower wall. But, the minimum value of C_f on the upper wall occurs slightly downstream on the leeward side of the bump. The C_f of the current wall-modeled cases match well with the DNS results on the windward side of the bump up to a certain point but peak higher and attain their maximum at slightly downstream locations closer to the summit of the bump. Unlike the overprediction seen in the current wall-modeled cases, Chen's LES shows an underprediction of the C_f. Again, the current simulations perform better than Chen's LES following trends closer to the DNS results.

The pressure coefficient, $C_p = (p - p_{h,i})/\frac{1}{2}\rho u_{max}^2$ distribution along the upper and lower walls are shown in figures 5.14(c) and 5.14(d) respectively. Here, $p_{h,i}$ is the inlet pressure at the channel half-height. Qualitatively, all the wall-modeled cases and DNS simulations show similar trends. On the lower wall, the DNS results attain a minimum value of pressure before the summit of the bump, whereas on the upper wall, a minimum pressure is attained at a location after the summit of the bump. These locations are slightly downstream the locations of maximum C_f on both the upper and lower walls. Upstream of the bump, the current wall-modeled cases show a drop in pressure for a small distance. The pressure of the wall-modeled cases recovers and follows the DNS results until the minimum pressure is attained by the DNS. Unlike the pressure recovery seen in the DNS results, the pressure drops further for the current wall-modeled cases. The minimum values of pressure occur after the summit of the bump. Downstream the bump's summit, the pressure is lower for the current wall-modeled cases in comparison with the DNS results except near the re-attachment point of the DNS. Chen's LES results have a better agreement with the DNS before the summit of the bump and in the straight section after the bump. The minimum pressure is not predicted well by Chen's LES, and the results do not quite match up on the leeward side of the bump in comparison with the DNS results. All

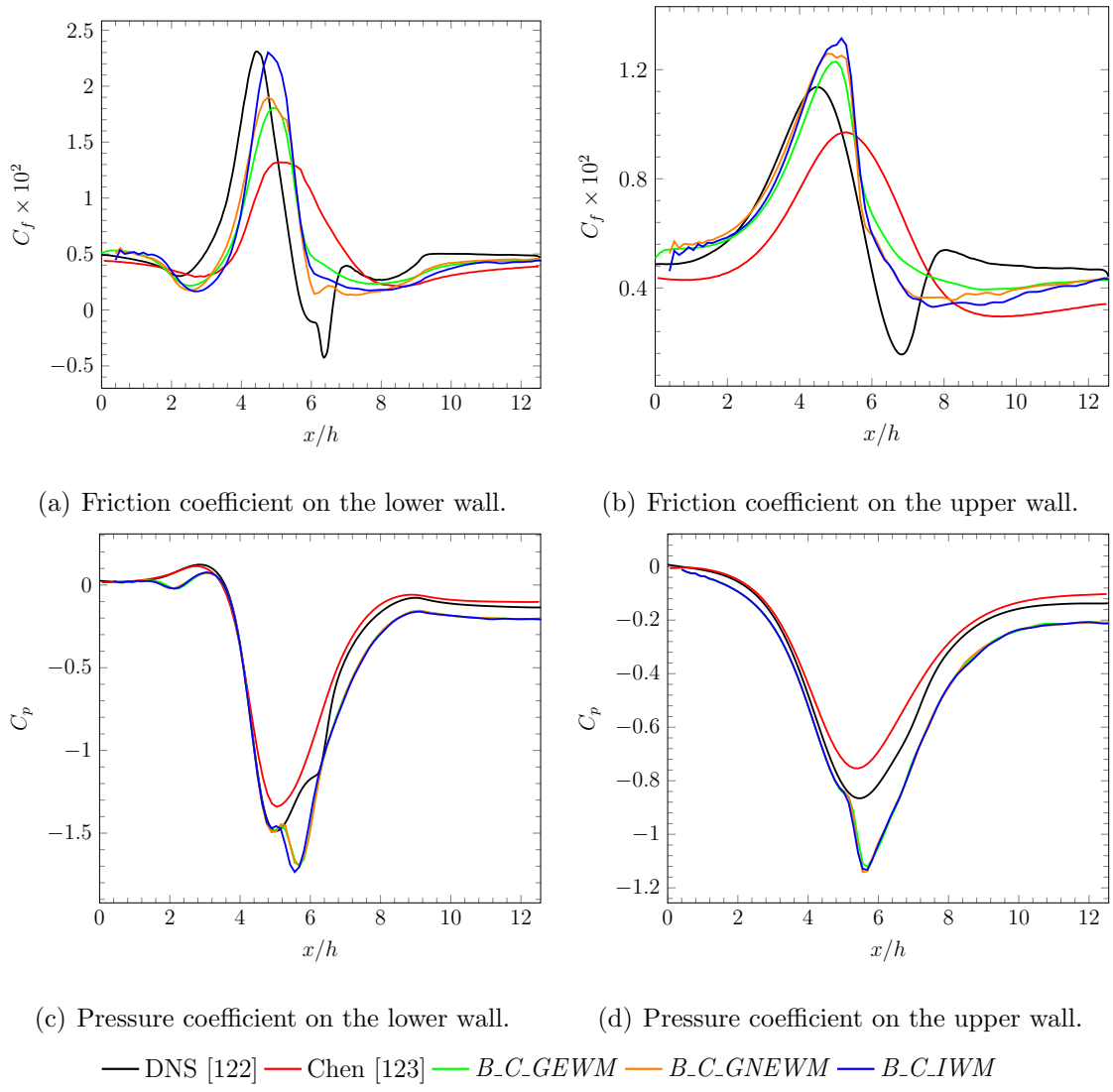

(a) Friction coefficient on the lower wall.

(b) Friction coefficient on the upper wall.

(c) Pressure coefficient on the lower wall.

(d) Pressure coefficient on the upper wall.

Figure 5.14. Flow quantities along the walls. Comparison of three wall-models using the coarse mesh with DNS [122] and Chen's LES using GNEWM on a coarse grid [123].

three wall-models used in the current simulations predicted similar results. The only noticeable difference is near the minimum pressure location for the *B_C_IWM* case. The pressure attains a lower value slightly upstream for the *B_C_IWM* case when compared with the *B_C_GEWM* and *B_C_GNEWM* cases simulated here.

Next, the mean velocity, turbulent kinetic energy (TKE) and Reynolds shear stress are plotted in figures 5.15 and 5.16. The profiles shown are in the wall-normal

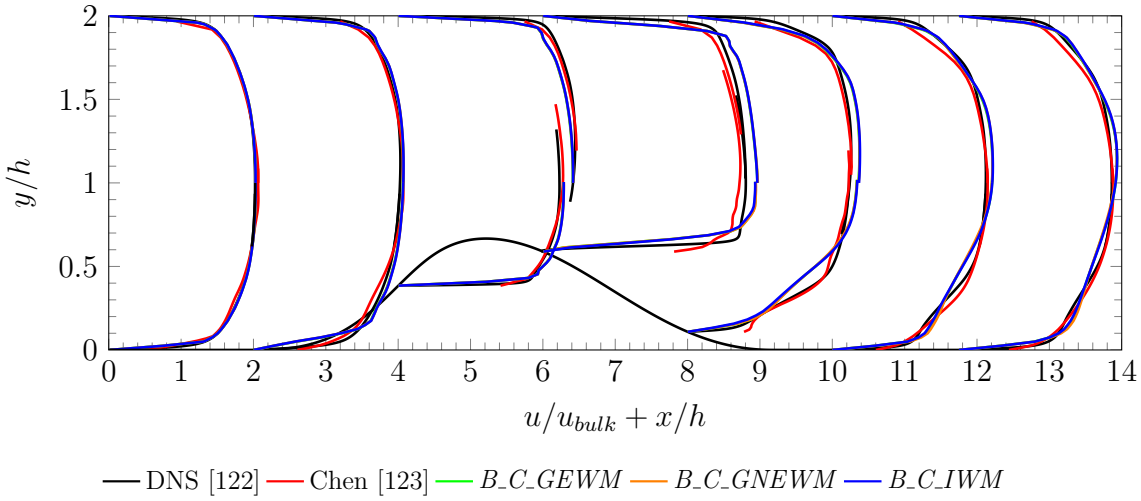

Figure 5.15. Mean velocity profiles at various streamwise locations. Comparison of three wall-models using the coarse mesh with DNS [122] and Chen's LES using GNEWM on a coarse grid [123].

direction, which is not the same as the vertical direction for points on the bump. Similar to Chen [123], using vector projection and tensor transformations, the flow parameters in the local coordinate system are transformed and later interpolated to the wall-normal direction to compare with the DNS and Chen's LES results. The profiles are compared at multiple streamwise locations (x/h = 0, 2, 4, 6, 8, 10 and 12).

The mean velocity profiles compared in figure 5.15 are nondimensionalized using the bulk velocity, u_{bulk} computed at the inlet. The bulk velocity is defined as

$$u_{bulk} = \frac{1}{h}\int_0^h u dy. \tag{5.4}$$

Upstream of the summit of the bump, the velocity profiles of the current wall-modeled simulations agree well with the DNS results. On the leeward side of the bump at x/h=6 and 8, the current wall-modeled cases predict higher velocity and different near wall profiles in comparison with the DNS results. The higher velocity is consistent with the underprediction of pressure noticed in the current wall-modeled simulations. Downstream towards the end of the channel, the velocity decreases and the wall-

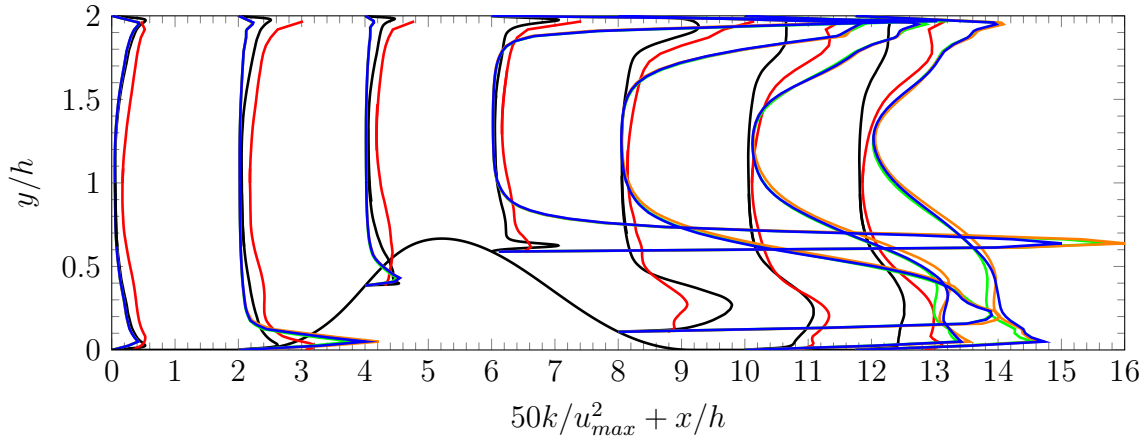

(a) Tubulent kinetic energy

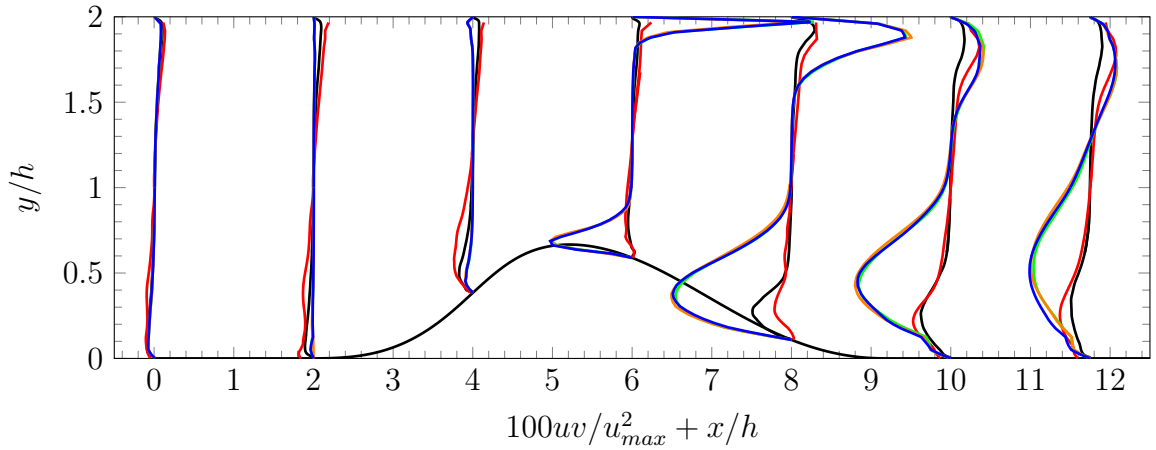

(b) Reynolds shear stress

DNS [122] Chen [123] *B_C_GEWM* *B_C_GNEWM* *B_C_IWM*

Figure 5.16. Turbulent kinetic energy and Reynolds shear stress at various streamwise locations. Comparison of three wall-models using the coarse mesh with DNS [122] and Chen's LES using GNEWM on a coarse grid [123].

modeled cases tend to regain the shape of the DNS velocity profiles. The wall-models do not have any impact on the mean velocity. Chen's LES results match well at most of the locations except at x/h=6.

The turbulent kinetic energy, k, shown in figure 5.16(a) is computed using

$$k = \frac{(u'_{rms})^2 + (v'_{rms})^2 + (w'_{rms})^2}{2}. \tag{5.5}$$

First, the TKE near the lower wall of the current wall-modeled cases is compared with the DNS. The TKE is overpredicted at most of the locations except at x/h=4. On the bump at x/h=4, the TKE has a good agreement. Downstream of the summit of the bump, the TKE is very high, and it then reduces as the flow propagates downstream towards the end of the channel. Now comparing the TKE near the upper wall of the current wall-modeled cases with the DNS, it can be noticed that the TKE is underpredicted upstream of the summit of the bump, whereas it is overpredicted at the downstream locations. Away from the walls, the TKE of the current wall-modeled cases agree well with the DNS but the agreement deteriorates towards the end of the channel. All the wall-models produce similar results. Chen's LES results show overprediction of the TKE at most of the locations except at locations on the leeward side of the bump where TKE is underpredicted near the lower wall.

The Reynolds shear stress is shown in figure 5.16(b). Upstream of the summit of the bump, all the wall-modeled cases compare well with the DNS results. At locations after the summit of the bump, the current wall-modeled cases overpredict the magnitude near the lower wall and the upper wall in comparison with the DNS results. Away from the walls, the behavior is similar to the trends seen in the TKE results.

To summarize, unlike in the simulations of accelerating boundary layers, all the wall-models produced different C_f due to the relatively higher Reynolds number used in the simulations of converging-diverging channel flow. The wall-models are sensitive to the pressure gradient in the acceleration and deceleration regions. Unfortunately, none of the wall-models can capture the flow separation noticed in the DNS. Among the wall-models used, the IWM wall-model produced better C_f, as it captured the peak C_f well on the lower wall. Only minor differences existed between the GEWM and GNEWM wall-models. Although the fluxes imposed by the wall-models are different, it did not affect the results of various flow parameters, which shows that

the imposed boundary condition on the wall only has a weak interaction with the resolved LES. The current simulation using GNEWM performs better than that of Chen's wall-model LES which uses the same wall-model. The current wall-model simulations predict a very high turbulent kinetic energy and Reynolds shear stress. The higher levels could be either due to the use of a grid with coarser resolution or the boundary conditions imposed by the wall-models. These are verified by increasing the grid resolution and by imposing the wall shear-stress from the DNS. Their effect on the turbulent kinetic energy and Reynolds shear stress is discussed in the next subsequent sections.

Fine Grid Results

The results using the fine grid for the converging-diverging channel flow are discussed in this section. The fine grid used in the current set of simulations has almost twice the number of grid points in both the streamwise and spanwise directions. The number of grid points in the vertical direction is also increased but not doubled as in the other two directions. Comparisons similar to those of the coarse grid cases are made for the fine grid results.

The skin-friction coefficient along the lower wall is plotted in figure 5.17(a). Qualitatively, the trends are similar to those of the coarse grid cases. Upstream of the bump, the wall-modeled cases overpredict the skin-friction which is not seen in the cases with the coarse grid resolution. Near the foot of the bump on the windward side, between $x/h = 2.2$ and 3.2, C_f of the current wall-modeled cases does not drop as much as noticed in the coarse grid cases. At the foot of the bump on the windward side, C_f is no longer underpredicted for the current wall-modeled cases. The peak C_f is lowered and occurs slightly downstream when compared to the coarse grid cases, whereas on the upper wall, the peak C_f value is increased and occurs further downstream. The skin-friction coefficient on the upper wall is plotted in figure 5.17(b). Another noticeable difference is the overprediction of C_f on the leeward side of the

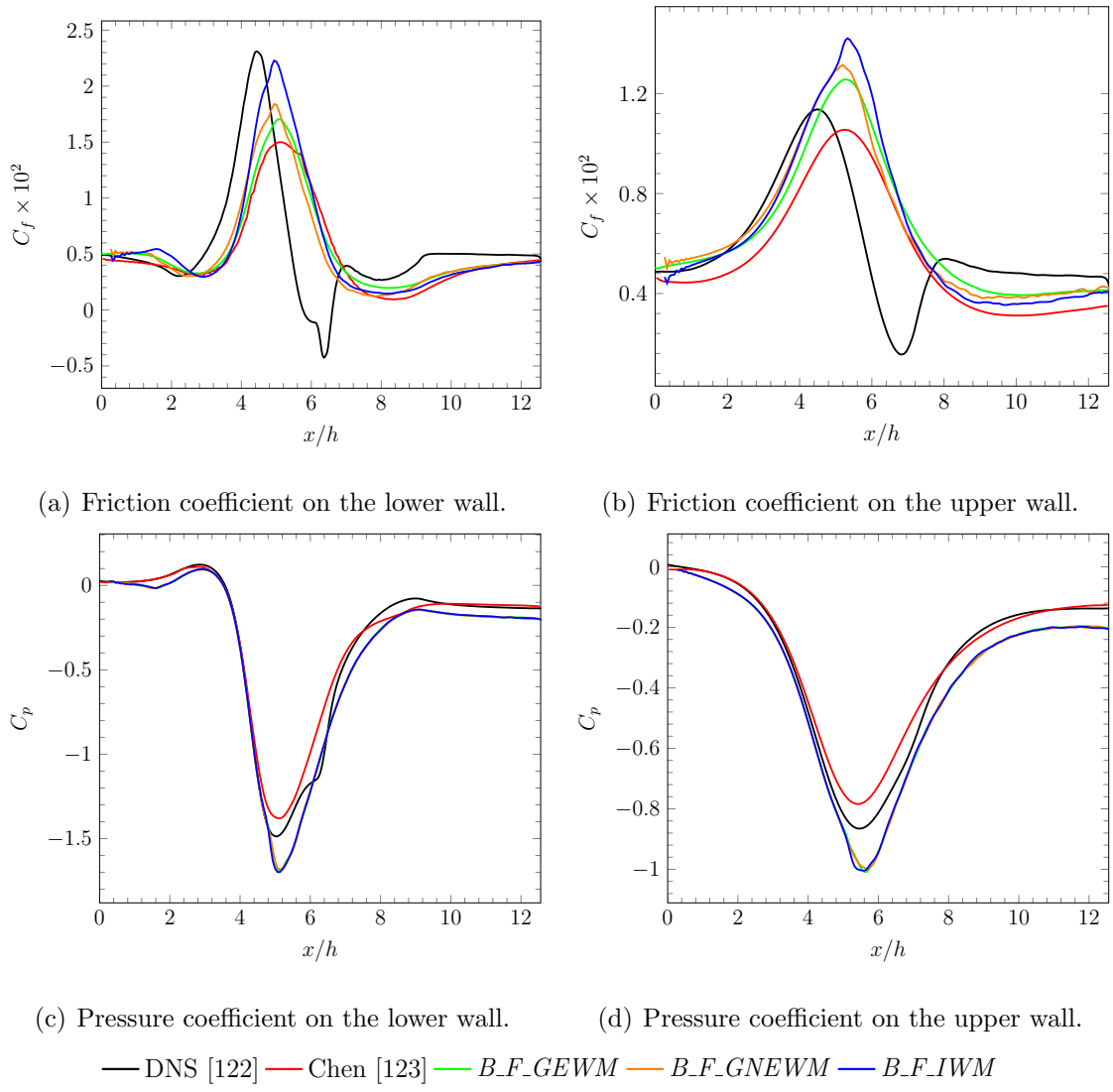

(a) Friction coefficient on the lower wall.

(b) Friction coefficient on the upper wall.

(c) Pressure coefficient on the lower wall.

(d) Pressure coefficient on the upper wall.

Figure 5.17. Flow quantities along the walls. Comparison of three wall-models using the fine mesh with DNS [122] and Chen's LES using GNEWM on a fine grid [123].

bump in comparison with cases utilizing the coarse grid. In the straight section, downstream of the bump, the differences between the wall-modeled cases are reduced and show similar behavior especially on the lower wall.

The grid refinement improves the results of the pressure distribution along the walls as can be seen in figures 5.17(a) and 5.17(b) along the upper and lower walls respectively. On the lower wall, at locations upstream of the bump, the fine grid cases

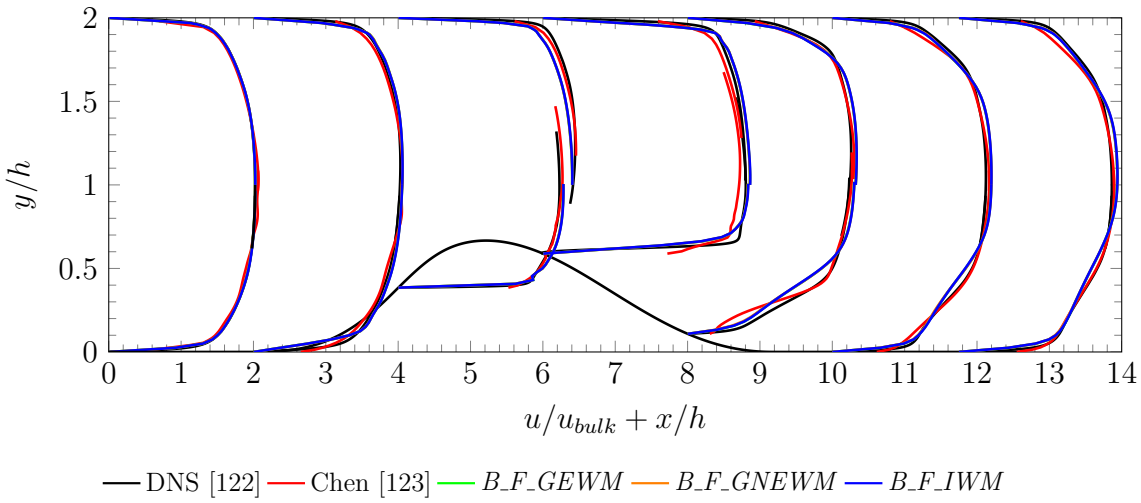

Figure 5.18. Mean velocity profiles at various streamwise locations. Comparison of three wall-models using the fine mesh with DNS [122] and Chen's LES using GNEWM on a fine grid [123].

match better with the DNS than the coarse grid cases. The location and magnitude of the minimum C_p captured by the fine grid cases are also improved on both the upper and lower walls. Downstream of the summit of the bump, the results are improved on both the lower and upper walls.

The mean velocity profiles plotted in figure 5.18 show good agreement with the DNS results compared to the coarse grid cases. On the leeward side of the bump, the flow does not accelerate further as noticed in the coarse grid cases. The use of a fine grid helped in improving the results in the near wall region in the downstream locations towards the end of the domain.

Lastly, the turbulent kinetic energy and Reynolds shear stress obtained for cases utilizing the fine grid are compared in figure 5.19. Upstream of the summit of the bump, the fine grid cases reproduce the TKE better on the upper wall in comparison with the DNS results, whereas the coarse grid cases underpredict the TKE. On the lower wall, except at $x/h = 4$, the TKE levels are lower for the fine grid cases compared to the coarse grid cases but they reach similar levels towards the end of the channel. Away from the walls, TKE is captured better by the fine grid cases in com-

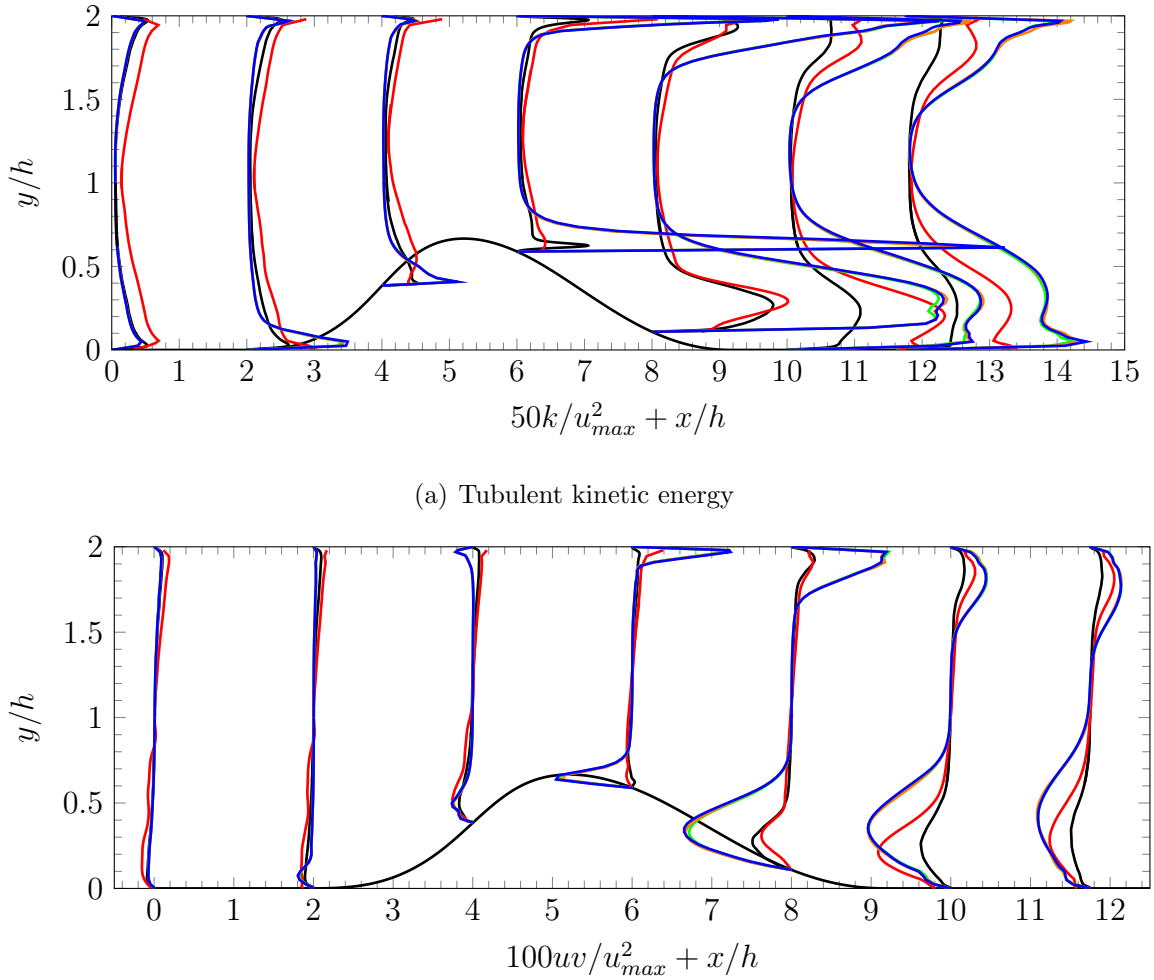

(a) Tubulent kinetic energy

(b) Reynolds shear stress

Figure 5.19. Turbulent kinetic energy and Reynolds shear stress at various streamwise locations. Comparison of three wall-models using the fine mesh with DNS [122] and Chen's LES using GNEWM on a fine grid [123].

parison with the DNS results than the coarse grid cases. The Reynolds shear stress shows similar behavior to that of the TKE when the grid resolution is increased. To get better insight, the TKE contours of the DNS along with the fine and coarse grid wall-modeled cases utilizing GEWM are plotted in figure 5.20. The DNS contours show the highest levels of TKE occur near the wall on the leeward side of the bump

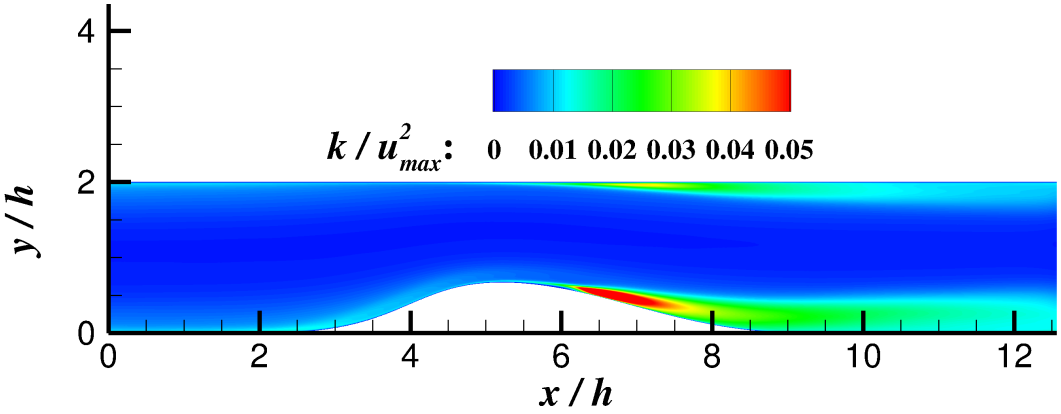

(a) DNS [122]

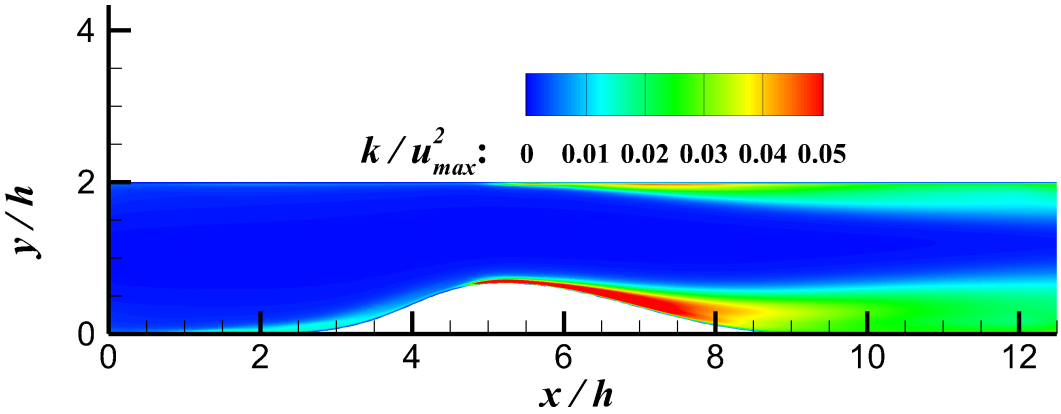

(b) *B_F_GEWM*

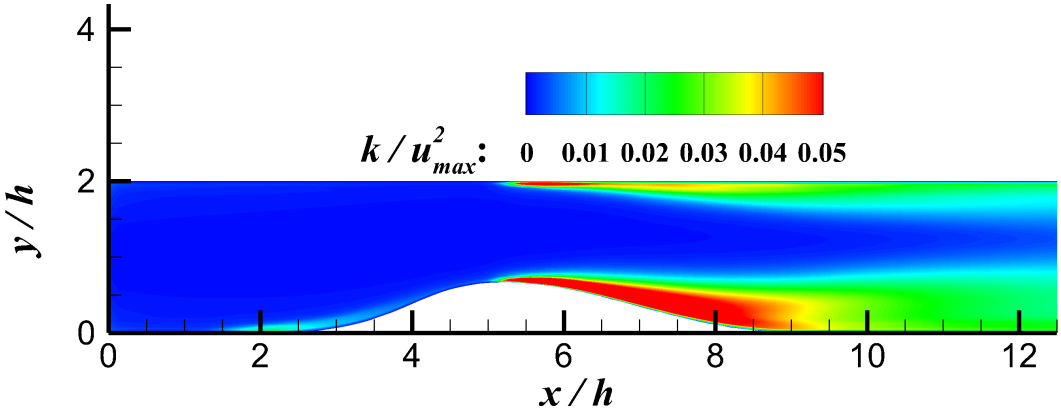

(c) *B_C_GEWM*

Figure 5.20. TKE contours for the DNS [122] and fine and coarse grid wall-modeled cases using GEWM wall model.

where the flow separates. The TKE spreads slowly and dissipates as the flow propagates downstream in the channel. It is apparent that the location at which high TKE production can be noticed is different for the wall-modeled cases compared to the DNS. Unlike the DNS, high levels of TKE can be seen near the summit of the bump for the wall-modeled cases. The TKE then damps out as the flow traveling downstream. When a fine grid is used in the current wall-model simulations, the TKE is confined closer to the wall with limited spreading and is in better agreement with the DNS.

From the above discussion, it can be concluded that an adequate grid resolution is required to capture the flow dynamics. Using a finer grid, reduces the differences between the results of the current wall-modeled simulations and the DNS. Similar to the coarse grid results, all the wall-model cases produce nearly identical results, although the boundary conditions imposed by the wall-models vary. Refining the grid reduces the overprediction of turbulent kinetic energy and Reynolds shear stress. However, the turbulent kinetic energy and Reynolds shear stress of the wall-modeled cases are higher than in the DNS. The cause of high turbulent kinetic energy and Reynolds stress levels in the current wall-modeled simulations is further analyzed in the next section by imposing the wall shear-stress from the DNS.

Wall-Modeling using DNS Wall-Shear Stress

The previous two sections discuss the effects of grid resolution and wall-model on the results. Although the fluxes supplied by the wall-models differ, the mean velocity, turbulent kinetic energy and Reynolds shear stress results are similar in simulations using the same grid. Moreover, the turbulent kinetic energy and Reynolds shear stress are overpredicted in the current simulations. To further analyze how the boundary conditions supplied by a wall-model have an impact on the results, instead of using any of the wall models, a simulation was performed by directly imposing the wall-shear stress from the DNS on both the top and bottom walls. This case is referred to

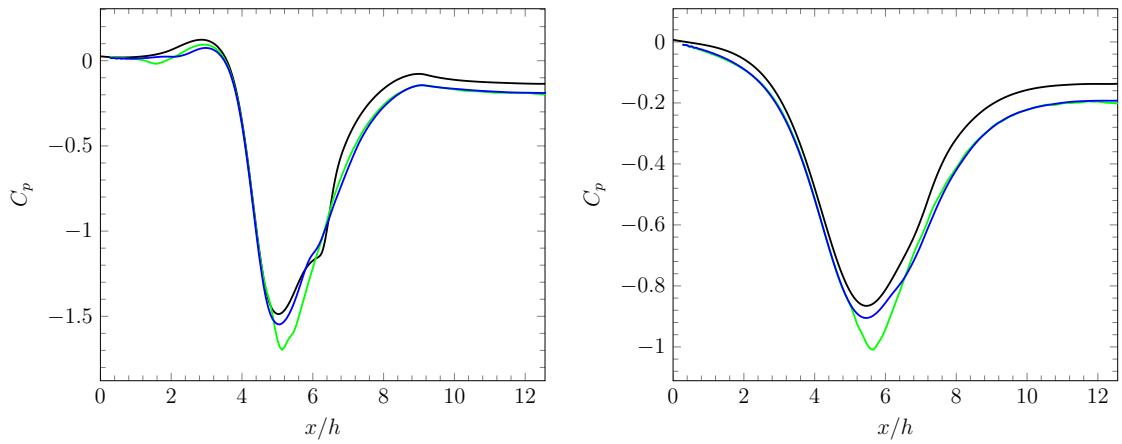

(a) Pressure coefficient on the lower wall. (b) Pressure coefficient on the upper wall.

Figure 5.21. Pressure coefficient along the walls. Comparison of *B_F_GEWM* and *B_F_DNS* with DNS [122].

as *B_F_DNS*. The wall-shear stress from the DNS is interpolated onto the LES grid. The fine grid is used for this test. It should be noted that the wall-shear stress imposed by the wall-models is computed instantaneously on the fly using the instantaneous LES flowfield data during each time-step, whereas here the mean wall-shear stress from the DNS is imposed during the time advancement with no added fluctuations. Next, the results of the *B_F_DNS* case are compared with the DNS and *B_F_GEWM* case.

The pressure distribution plotted in figure 5.21 shows that the *B_F_DNS* case has a better agreement in capturing the minimum pressure of the DNS compared to the *B_F_GEWM* case on both walls. The pressure distributions of the wall-modeled cases are nearly the same at locations downstream the summit of the bump. Since the imposed wall-shear stress of the DNS shows flow separation on the lower wall, the mean streamwise velocity contour is plotted in figure 5.22 to check the occurrence of flow separation on the lower wall for the *B_F_DNS* case. The figure also includes the streamlines traced out by the fluid particles close to the lower wall. Unfortunately,

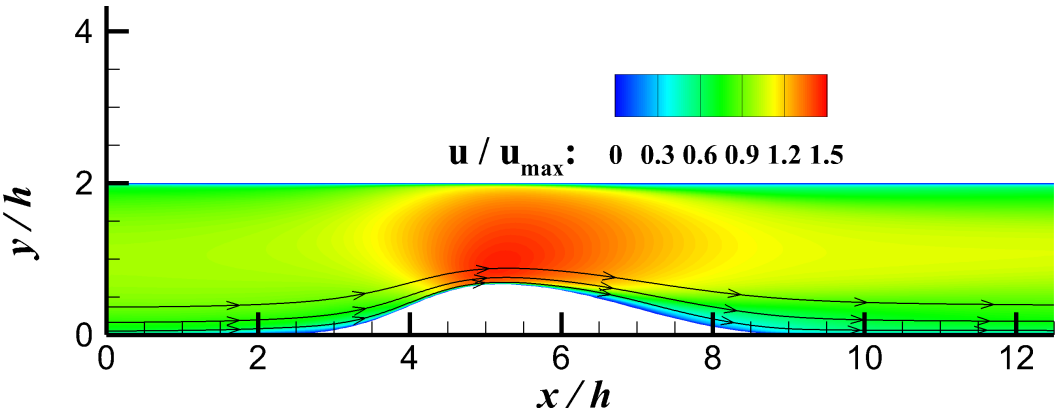

Figure 5.22. Mean velocity contour for the wall-modeled case modeled using wall-shear stress from the DNS [122].

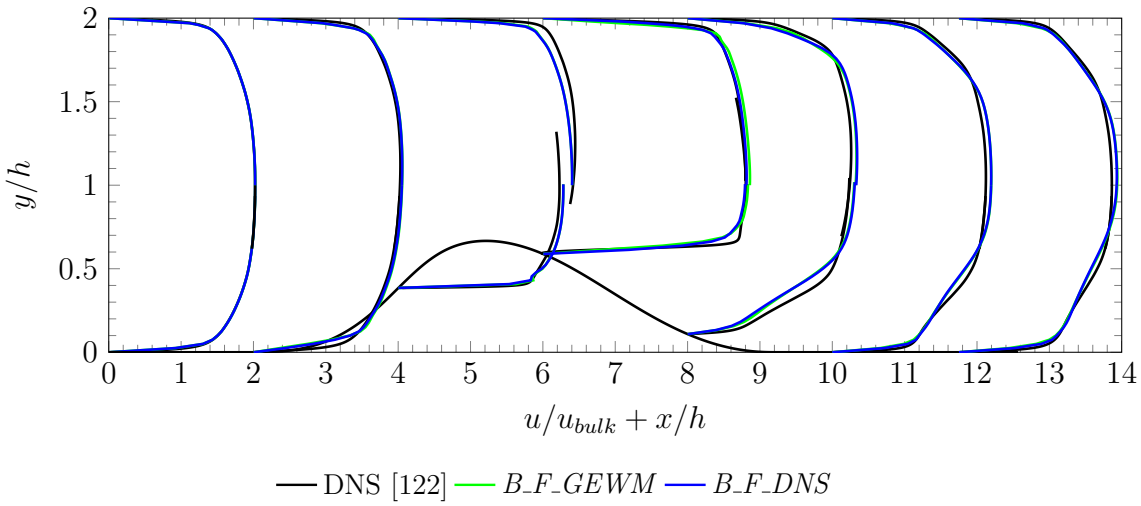

Figure 5.23. Mean velocity profiles at various streamwise locations. Comparison of *B_F_GEWM* and *B_F_DNS* with the DNS [122].

the flow did not separate from the lower wall with the imposed wall-shear stress from the DNS, which includes a region of negative wall shear-stress. This could be due to the use of a grid that is too coarse at the wall in the wall-modeled LES. The grid resolution is unable to resolve the velocity gradients at the wall. Grids used in the wall-modeled LES are designed in such a way that they bypass the cost associated in

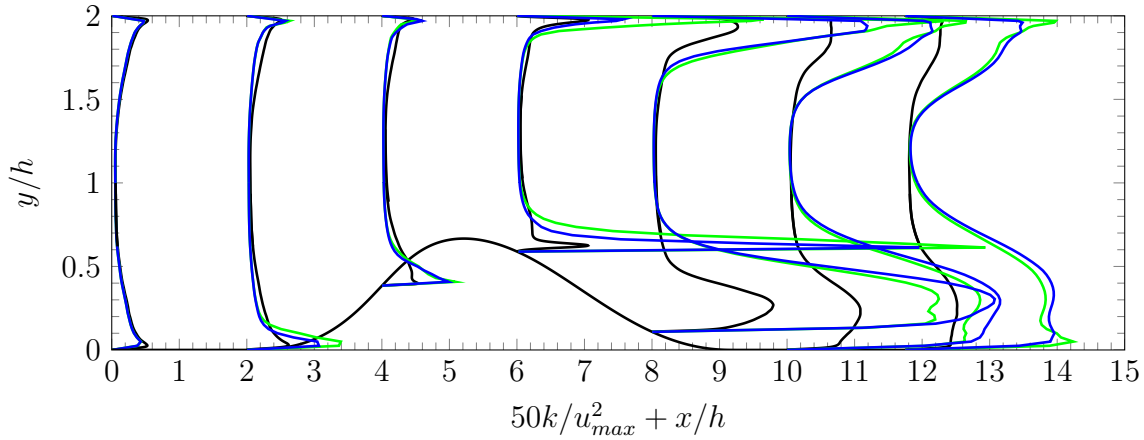

(a) Tubulent kinetic energy

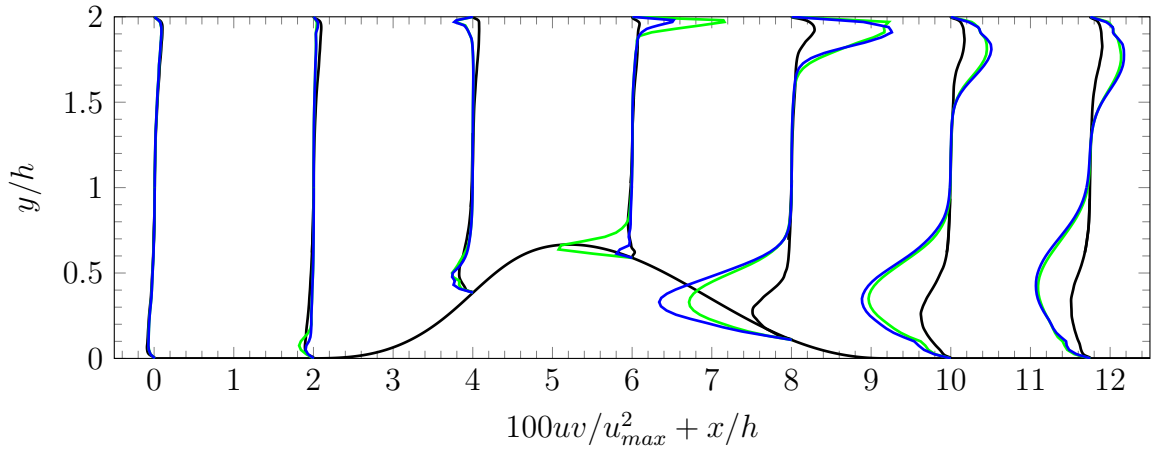

(b) Reynolds shear stress

DNS [122] *B_F_GEWM* *B_F_DNS*

Figure 5.24. Turbulent kinetic energy and Reynolds shear stress at various streamwise locations. Comparison of *B_F_GEWM* and *B_F_DNS* with the DNS [122].

resolving the near wall region. Quantitative comparisons of the mean velocity made in figure 5.23 shows no difference between the wall-modeling strategies used.

Noticeable differences can be seen in the TKE and Reynolds shear stress profiles plotted at various axial locations in figure 5.24. The *B_F_DNS* case shows lower levels of TKE along the upper wall in comparison with the *B_F_GEWM* case. Although the

TKE of the *B_F_DNS* case agrees well with the DNS results before the summit of the bump on the upper wall, the TKE is overpredicted downstream of the summit of the bump. Near the lower wall, the TKE of *B_F_DNS* is still higher at all the locations compared to the DNS. Comparing with the *B_F_GEWM* case, the TKE of *B_F_DNS* case is lower for $x/h \leq 6$ and higher elsewhere. The Reynolds shear stress of the *B_F_DNS* case is lower at $x/h = 6$ but increases downstream reaching the levels of *B_F_GEWM*.

The results in this section show the importance of the wall-model correctly specifying the wall-shear stress. The use of more accurate wall-shear stress values did not fully resolve the differences between the DNS and the wall-modeled simulations. However, the results of the *B_F_DNS* case show improvement over its predecessor simulations. Notably, the pressure distribution and the TKE on the upper wall are impacted by the use of more accurate wall-shear stress values from the DNS. It looks like the minimum skin friction on the upper wall captured by the DNS is vital in controlling the TKE levels up to a certain extent. None of the wall-models obtain the minimum C_f as seen in the DNS in figures 5.17(a) and 5.17(b). However, on the lower wall, the TKE levels are still high even after imposing the more accurate wall-shear stress values. The lack of an SGS model in ILES may result in an underprediction of the dissipation rate and therefore, lead to the TKE being too large. So, it is worthwhile to asses the impact of the SGS modeling in the near wall region which is analyzed in the next section. The mean velocity does not seem to be impacted by the modeled wall-shear stress. The Reynolds shear stress is also effected near the region of the minimum in C_f. Since only the mean wall-shear stress is imposed on the wall for the *B_F_DNS* case, it would be worthwhile to test adding fluctuations, which are essential for turbulence redistribution, in the future, however, this is left out of the current research work.

Wall-Modeling in the DSM Framework

With results in the earlier sections showing high levels of TKE, it is necessary to analyze whether relying upon the spatial filter as described in section 2.2.1 to remove the unresolved turbulence scales is sufficient or not. The effectiveness of the spatial filter is tested by carrying out a simulation using an explicit SGS model. The DSM model described in section 2.4 is used for this purpose. This case is similar to the *B_C_GEWM* case utilizing a coarse grid and *GEWM* and is denoted as case *B_C_DSM*.

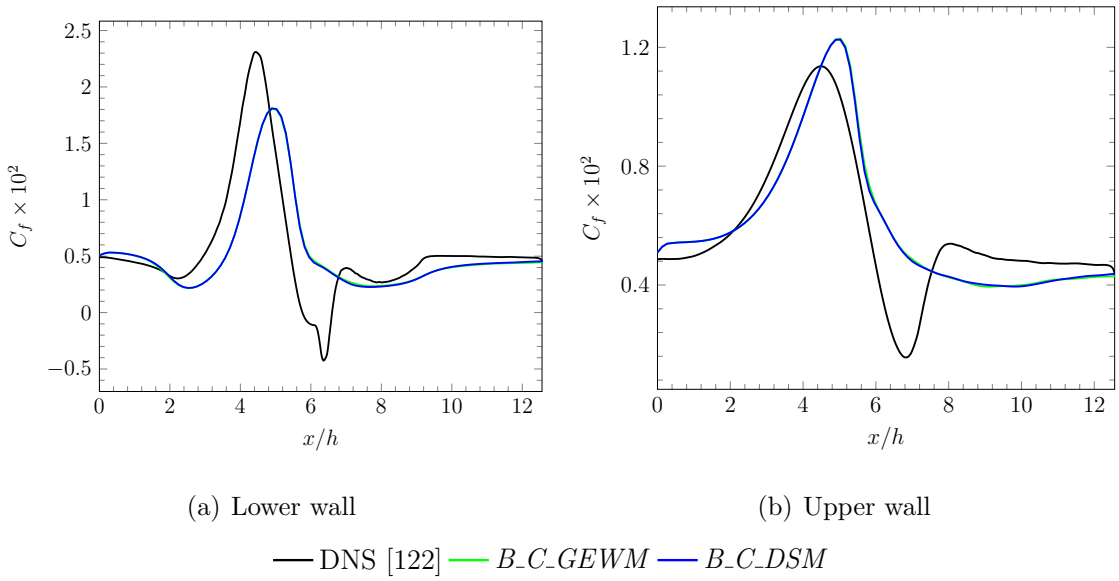

(a) Lower wall (b) Upper wall

Figure 5.25. Friction coefficient along the walls. Comparison of cases utilizing implicit and explicit subgrid scale modeling with the DNS [122].

For brevity, only the skin friction coefficient and the TKE plots are shown and are plotted in figures 5.25 and 5.26 respectively. The results of the case using DSM are compared with its counterpart that uses ILES methodology and the DNS. Unfortunately, the use of DSM did not help in damping the TKE near the walls, and the results show no variation from the case utilizing the ILES methodology. Another case using a fine grid and similar to *B_F_GEWM* was also tested using DSM as the SGS

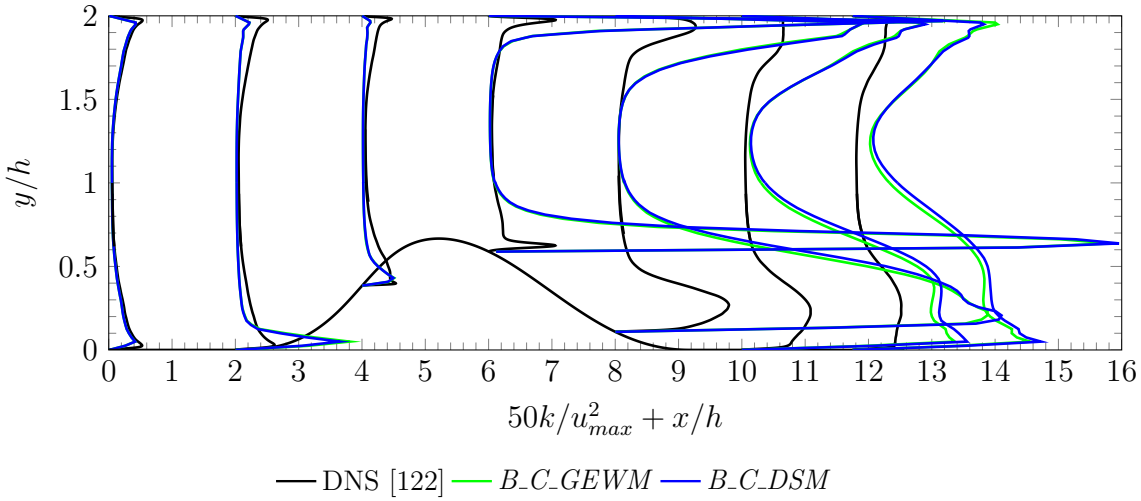

Figure 5.26. Turbulent kinetic energy at various streamwise locations. Comparison of cases utilizing implicit and explicit subgrid scale modeling with the DNS [122].

model which showed no differences with its counterpart simulation using the ILES methodology. Since the primary focus of the current research is to check different wall models within the framework of an ILES SGS model, no further tests using DSM have been carried out.

5.2.3 Summary and Conclusions

The simulations of flow through a converging-diverging channel have been completed to validate and analyze the wall-models that have been implemented in the modular-LES code. A total of eight simulations were performed to understand the behavior of the wall-models, grid quality, and SGS modeling. The following conclusions can be drawn from the analyses of flow through a converging-diverging channel.

A few discrepancies are noticed between the wall-modeled simulations and the DNS. The results show that an adequate grid resolution is required to capture the flow dynamics accurately. The fine grid used in the current study can predict the flowfield with good accuracy away from the walls. However, the grid resolution utilized in the

present study is not fine enough to capture the flow physics in the near wall region. The grids used are unable to predict the separation that occurs on the lower wall. Kuban et al. [126] carried out multiple wall-resolved LES simulations of the same converging-diverging channel flow operating at the same conditions and found that a streamwise resolution of 45 wall units at the summit of the bump is necessary to model the recirculation region. In the current simulations, the grid resolution is coarser than the proposed value. It must be noted that the spatial discretization provided in table 5.5 are at the inlet, and since a uniform grid is used in the current simulations, these values increase as the flow accelerates downstream. However, an attempt to further increase the grid resolution is not made, as the primary focus of the research is for testing wall-models for flows subjected to acceleration and not for decelerating flows or flows having separation. The grids used also overpredict turbulent kinetic energy and Reynolds shear stress in the near wall region. The overprediction of turbulent quantities improves with grid resolution.

The wall-models are found to be sensitive to the pressure gradients in the regions of acceleration and deceleration and produce approximately similar results in the straight section before and after the bump. Among the wall-models used, the IWM captures the peak wall-shear stress noticed in the DNS results but does so at a slightly downstream location. However, the wall-models are unable to capture the flow separation occurring on the lower wall. The current cases utilizing the GNEWM predict the wall-shear stress better than Chen's [123] wall-modeled cases using GNEWM. The imposed boundary condition specified by the wall-models shows only a weak impact on the LES. However, using a more accurate wall-shear stress from DNS improved results but did not adequately address the differences. The use of an explicit SGS model predicts similar results as that of the ILES methodology.

6. AEROACOUSTICS OF JETS FROM SMC000 NOZZLE

The previous chapters discussed the preliminary simulations of the SMC000 nozzle using a shorter domain, development of various wall-models and testing of them for two accelerating flows. The knowledge gained from these chapters is applied to the wall-modeled simulations of the SMC000 nozzle using an extended domain for noise predictions.

The newly implemented wall-models, especially IWM, performed well for the accelerating flows. However, the boundary condition imposed by IWM is ineffective in reducing the TKE levels in comparison with the DNS results. The TKE levels only decrease with grid refinement. But grid refinement is not a feasible option as it increases the simulation cost. On the other hand, the results from Chapter 4 show that reducing the inflow velocity and density fluctuations added to the mean flow effectively reduces the TKE levels of the wall-modeled simulations. The approach of controlling the inflow fluctuations seems to be a viable option due to the low costs involved in running the simulations using a shorter domain. Utilizing this postdiction process, a simulation using an extended domain can be set up for noise predictions. In the current wall-modeled simulations of the SMC000 nozzle for noise predictions, the latter approach of controlling the fluctuations at the inflow is employed along with the GEWM. The GEWM is cheaper than the GNEWM or IWM. Unlike the GEWM, wall-models like the GNEWM or IWM constitute a system of equations that need to be solved iteratively. A total of two wall-modeled simulations operating at the SP12 condition are carried out to this end and compared with the available experimental and simulation flowfield and acoustic data. However, due to the unavailability of the flowfield experimental data at the SP12 operating condition, simulations were also carried out using the operating condition referred to as SP07 by Tanna et al. [56] for which both near-field flow measurements [62] and acoustic data [8] are available.

The remainder of this chapter is organized by first discussing the wall-modeled simulations of the SMC000 nozzle operating at the SP12 operating condition in Section 6.1. Later, in Section 6.2 the simulations carried out at the SP07 operating condition are discussed. The computational domain, simulation settings and results are also discussed in each of the sections.

6.1 Wall-modeled Simulations at the SP12 Operating Condition

The details about the nozzle and operating conditions are described in section 4.1. The first wall-modeled case was simulated by reducing the differences that exist between the settings of the previous wall-resolved simulation of Dhamankar et al. [48] and wall-modeled simulation of Aikens [45]. This case is referred to as *SF_WM* and uses similar inflow conditions as that of the wall-resolved case. The simulation settings of the *SF_WM* case are similar to that of the *SS_12_GEWM* case described in Chapter 4. The second case was simulated by adjusting the amplitudes of the density and velocity fluctuations added to the mean flow at the inflow. In Chapter 4, reducing the amplitudes of the velocity and density fluctuations by 65% compared to the *SS_12_GEWM* case helped in approximating the Reynolds stresses of the wall-resolved simulation at the nozzle exit. So, here the second wall-modeled case is simulated by reducing the fluctuation levels by 65% from that used in *SF_WM*. This case is referred to as *SF_WM_LIT* and is similar to the *SS_12_TURB_0.35* case described in Chapter 4.

6.1.1 Simulation Setup

The computational domain and boundary conditions used in these current simulations are similar to those of the shorter domain simulations that are described in Section 4.2.1. However, downstream of the nozzle, the domain is extended to $80R_j$ and $20R_j$ in the streamwise and radial directions. The domain extents used are similar to the previous wall-resolved [48] and wall-modeled [45] SMC000 simulations. The

sponge zone near the outflow boundary is now located in the region between $x = 70R_j$ and $x = 80R_j$. As mentioned previously, the GEWM is used in the two wall-modeled cases simulated here.

Table 6.1. Domain and grid information for the wall-modeled SMC000 SP12 simulations.

Superblock	**Description**	N_x	N_r	N_θ
1	Nozzle	288	75	512
2	Downstream of nozzle exit	626	75	512
3	Downstream of nozzle exit along the nozzle lip	626	30	512
4	Above the nozzle and upstream of its exit	80	160	512
5	Downstream of Superblock 4	626	160	512

The grid used for the current wall-modeled simulations is shown in figure 6.1 and is designed using the commercial grid generation software Pointwise. The grid is similar to that used in the wall-modeled SMC000 simulation by Aikens [45]. The wall-modeled grid is designed from the wall-resolved grid by coarsening it in the boundary layer inside the nozzle which also affects the grid resolution in the shear layer developing downstream of the nozzle exit. However, the exterior portions of the grids do not correspond exactly, and the placement and resolution of the ADS differ, with the wall-modeled grid having a finer resolution on the ADS. This affects the high frequency portion of the spectra, as discussed in the far-field acoustics results section. The current grid resolution is the same inside and outside of the nozzle (up to $5R_j$ and $3R_j$ in the streamwise and radial directions) as the coarse grid described in Section 4.2.2. At other locations, the grid is smoothly stretched in the streamwise

and radial directions. The overall grid is made up of 101 million grid points, and the details are tabulated in table 6.1.

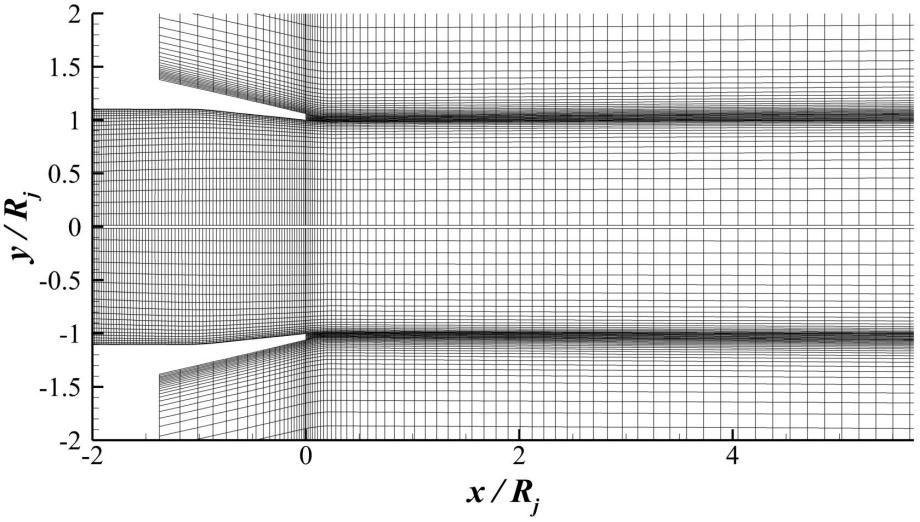

(a) Near Nozzle

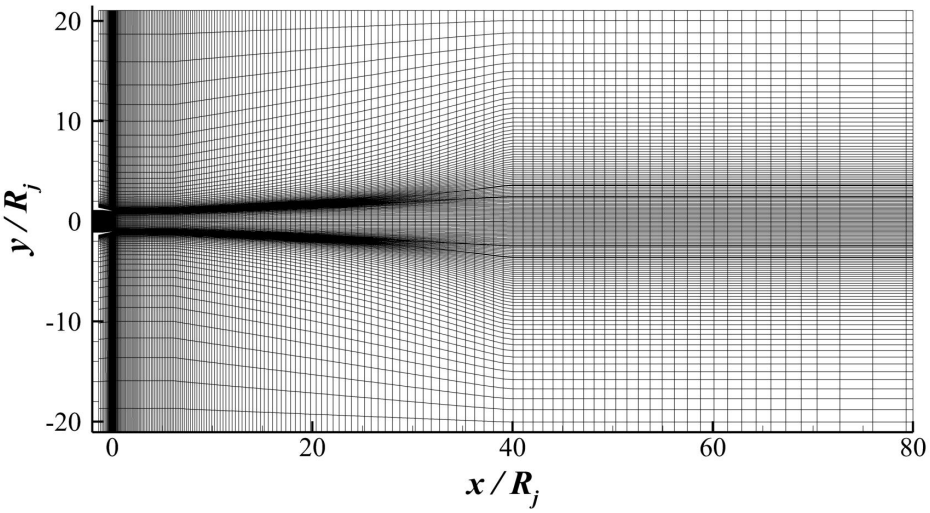

(b) Whole Domain

Figure 6.1. A streamwise slice of the grid used for the wall-modeled SMC000 SP12 simulations. Every fourth point is shown.

The table 6.2 shows the additional settings used in the two wall-modeled simulations. The times shown in the table are in terms of the reference time, $T = R_j/U_j$.

The case *SF_WM* was completed on the Stampede 2 supercomputer of the Texas Advanced Computing Center (TACC) whereas the case *SF_WM_LIT* was completed using both the Stampede and Stampede 2 supercomputers of TACC. By making use of the solution from a previous wall-modeled simulation, the current wall-modeled cases *SF_WM* and *SF_WM_LIT* were simulated only for 80T to remove the transients. The total cost to complete the current wall-modeled cases if run entirely on Stampede 1 or Stampede 2 are reported in table 6.2. Lastly, as described in Section 2.6.3, the minimum and maximum Strouhal numbers based on the acoustic sampling, St_{min} and St_{max}, are also shown in table 6.2.

Table 6.2. Remaining simulation settings used in the wall-modeled SMC000 SP12 simulations.

Time Details		
Time step size, Δt (T)	8×10^{-4}	
Transient period (T)	80	
Statistics gathering period (T)	344	
Max CFL Numbers (x, r, θ)	(0.34, 0.92, 0.70)	
Acoustic Sampling		
Output Frequency (timesteps / sample)	40	
Total Samples	10750	
St_{min}	5.8×10^{-3}	
St_{max}	31	
Machine Details		
Machine	TACC Stampede	TACC Stampede 2
Cores	2800	2800
Cores per node	16	68
Cost (core-hours)	81,000	—
Cost (node-hours)	—	4662

The instantaneous flowfield data required by the FWH method for the prediction of farfield acoustics are collected on different ADS as shown in figure 6.2. The ADS conforms to a given set of grid lines. The surface S_WR used for the previous wall-resolved case [45] starts at a radius of $2.8R_j$ at $x = 0$ and gradually increases in radius to a value of $11.9R_j$ at $x = 40R_j$ and remains constant until $x = 60R_j$. The surface S_WM_1 used for the previous wall-modeled simulation [48] starts at a radius of $2.8R_j$ at $x = 0$ similarly to the wall-resolved case and gradually increases in radius to a value of $10R_j$ at $x = 40R_j$ and remains constant until $x = 60R_j$.

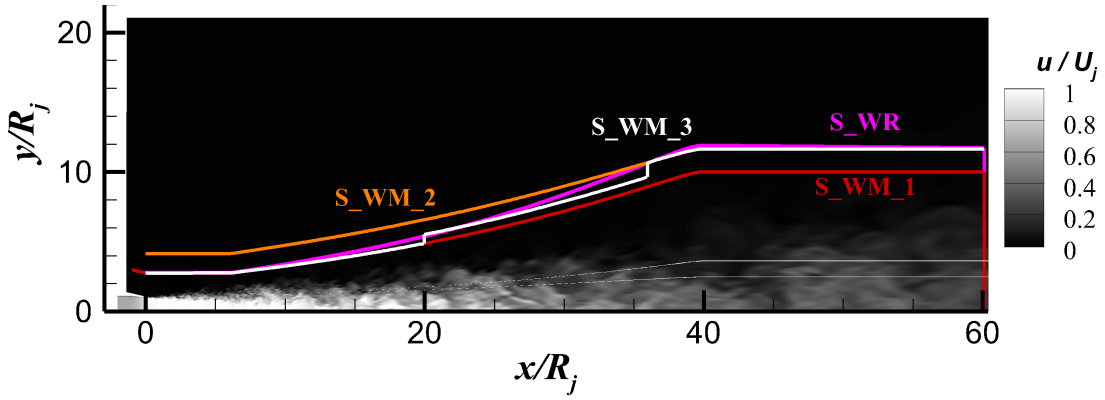

Figure 6.2. Contour plot of instantaneous axial velocity showing the acoustic data surfaces used in the wall-modeled SMC000 SP12 simulations.

The surface S_WM_1 is located on the portion of the grid having a finer resolution in comparison with the surface S_WR, which could affect the high frequency portion of the spectra. To keep the differences between the simulations minimal, in the current wall-modeled simulations, along with the surface S_WM_1, two more surfaces, S_WM_2 and S_WM_3 are used for collecting the flowfield data such that they are closely matched with the surface S_WR. The surface S_WM_2 is set up such that it matches the terminal radius of the surface S_WR. This surface ends up having a radius of $4.1R_j$ at $x = 0$. The surface S_WM_3 is set up as a telescopic surface such that it closely follows the surface S_WR. For both, the final radius is kept constant for $x > 40R_j$. An end-cap is located at $x = 60R_j$ for all of the surfaces.

6.1.2 Discussion of the Flowfield Results

This section discusses the flowfield results of the SMC000 nozzle wall-modeled simulations and comparisons are made with the wall-resolved simulation of Dhamanakar [48]. Since the experimental flowfield data is unavailable at the SP12 operating condition, the simulations results are not compared with the experimental data. As mentioned previously in Section 4.3, the wall-resolved simulation is referred to as *WR*. The radial profiles at the nozzle exit are plotted in figures 6.3 and 6.4. The results of the wall-modeled simulations at the nozzle exit are similar to their counterpart shorter domain simulations discussed in Section 4.3. The mean velocity profiles plotted in figure 6.3(a) are qualitatively similar to each other, and so are the density profiles which are shown in 6.3(b). The differences in the near wall grid resolution affect the boundary layer development between the wall-resolved and wall-modeled simulations. However, the boundary layer of the *SF_WM_LIT* case has a better agreement than the *SF_WM* case when compared with the *WR* case. The simulations show that the velocity decreases towards the centerline. This effect may be due to the 2-D nature of the flow because the nozzle is short and similar behavior might exist even in the experiments.

Various boundary layer parameters that characterize the boundary layer at the nozzle exit are also tabulated in table 6.3 for the three cases. Since the mean velocity decreases towards the centerline, the peak velocity in the boundary layer, u_p, is used as the reference quantity in the computation of boundary layer parameters. The location of the peak velocity, r_p, is used to define the edge of the boundary layer, unlike the traditional approach of using a point in the boundary layer where the velocity reaches 99% of the freestream velocity. It is clear that the *SF_WM_LIT* data are closer to the *WR* results than are the *SF_WM* data for all quantities except the shape factor. Note that a higher shape factor indicates that the boundary layer is less turbulent. This is consistent with the *SF_WM_LIT* case having lower prescribed inlet turbulence compared to the *SF_WM* case.

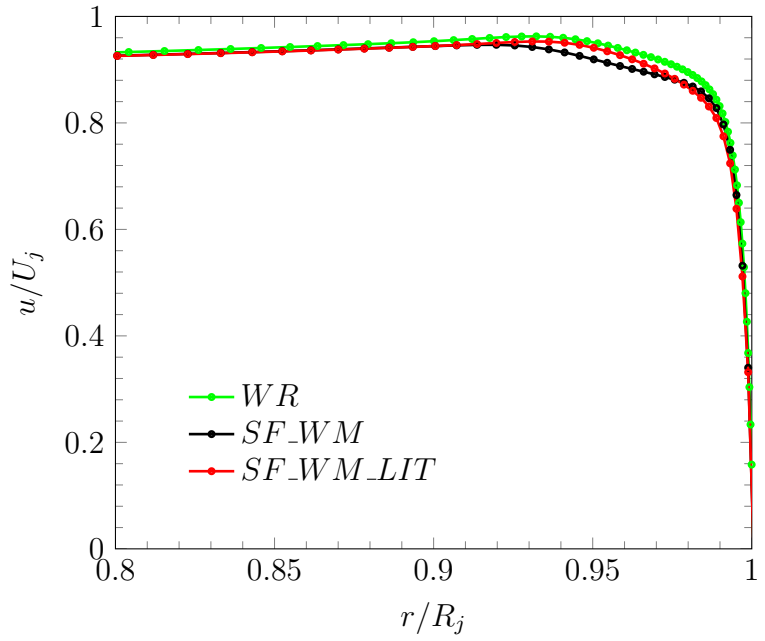

(a) Mean velocity

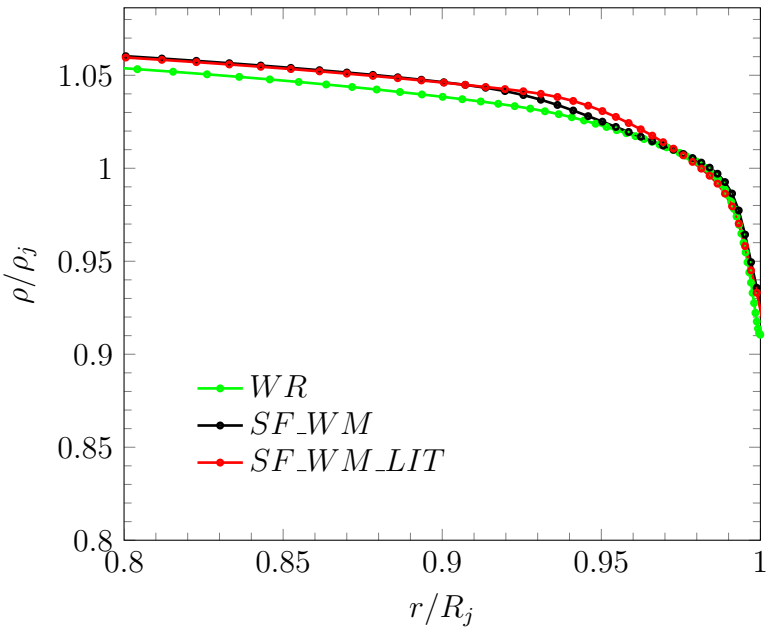

(b) Mean density

Figure 6.3. Comparison of the mean radial profiles at the SMC000 nozzle exit of the wall-modeled simulations with the wall-resolved simulation.

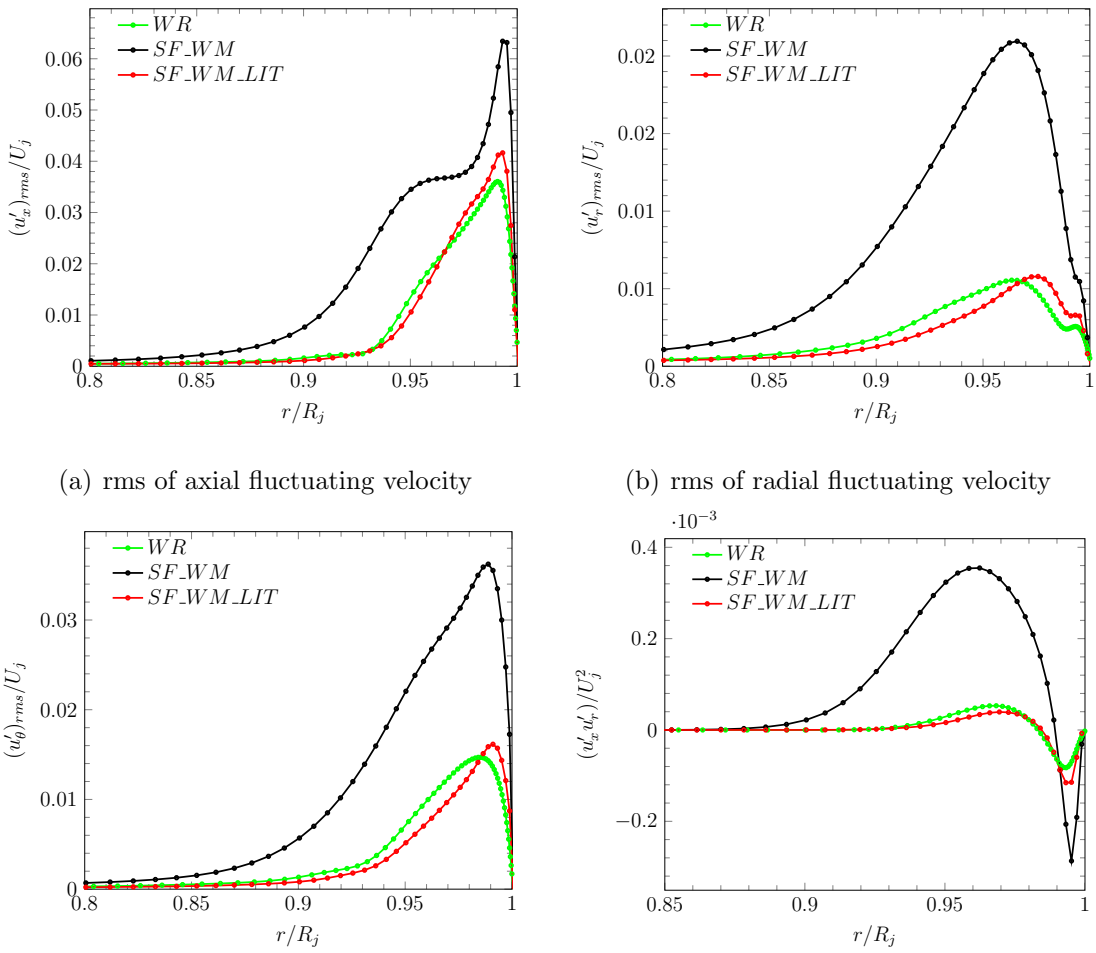

(a) rms of axial fluctuating velocity

(b) rms of radial fluctuating velocity

(c) rms of azimuthal fluctuating velocity

(d) Reynolds shear stress

Figure 6.4. Comparison of the rms fluctuating velocities and Reynolds shear stress at the SMC000 nozzle exit of the wall-modeled simulations with the wall-resolved simulation.

Table 6.3. Boundary layer parameters at the SMC000 nozzle exit of the wall-modeled and wall-resolved simulations.

	WR	***SF_WM***	***SF_WM_LIT***
Peak velocity (u_p/U_j)	0.9625	0.9467	0.9530
Location of peak velocity (r_p/R_j)	0.9323	0.9197	0.9310
Boundary layer thickness (δ_p/R_j)	0.0683	0.0808	0.0696
Displacement thickness (δ_p^*/R_j)	0.0073	0.0087	0.0085
Momentum thickness (θ_p/R_j)	0.0037	0.0043	0.0041
Shape factor ($H = \delta_p^*/\theta_p$)	1.9751	2.0178	2.0635

The rms fluctuating velocities in the axial, radial and azimuthal directions at the nozzle exit are plotted in figures 6.4(a) to 6.4(c). As mentioned before, the trends are similar to those discussed in Section 4.3. Controlling the turbulence levels at the inflow helps in matching the turbulence levels of the *SF_WM_LIT* case with the *WR* case. The turbulence levels of *SF_WM_LIT* and *WR* cases are much lower than those of the the*SF_WM* case. The Reynolds shear stress is shown in figure 6.4(d) also follows the general trends of the rms fluctuating velocities among the three cases.

The contours of TKE plotted in figure 6.5 show the qualitative development of the turbulence inside the nozzle for the wall-modeled and wall-resolved simulations. The TKE is computed using equation 4.2. All of the simulations show qualitatively similar trends. The TKE reduces initially in the redevelopment region until the development of realistic turbulence from the artificial turbulence specified at the inflow [16]. After the recovery to realistic turbulence, the TKE then begins to increase and reaches a peak at the beginning of nozzle contraction before reducing towards the nozzle exit due to the flow acceleration. At the inflow boundary, the peak mean TKE for the *SF_WM* case is higher than the *WR* case by 6.6%. Although the differences are minor, the TKE for the *SF_WM* case is almost twice that of the *WR* case near the beginning of the nozzle contraction, leading to higher turbulence at the nozzle exit. In contrast,

the lowering of turbulence levels at the inflow by 65% for the case *SF_WM_LIT* causes the TKE to be in the range of the *WR* case at the start of the nozzle contraction and thereby to reach similar levels towards the nozzle exit.

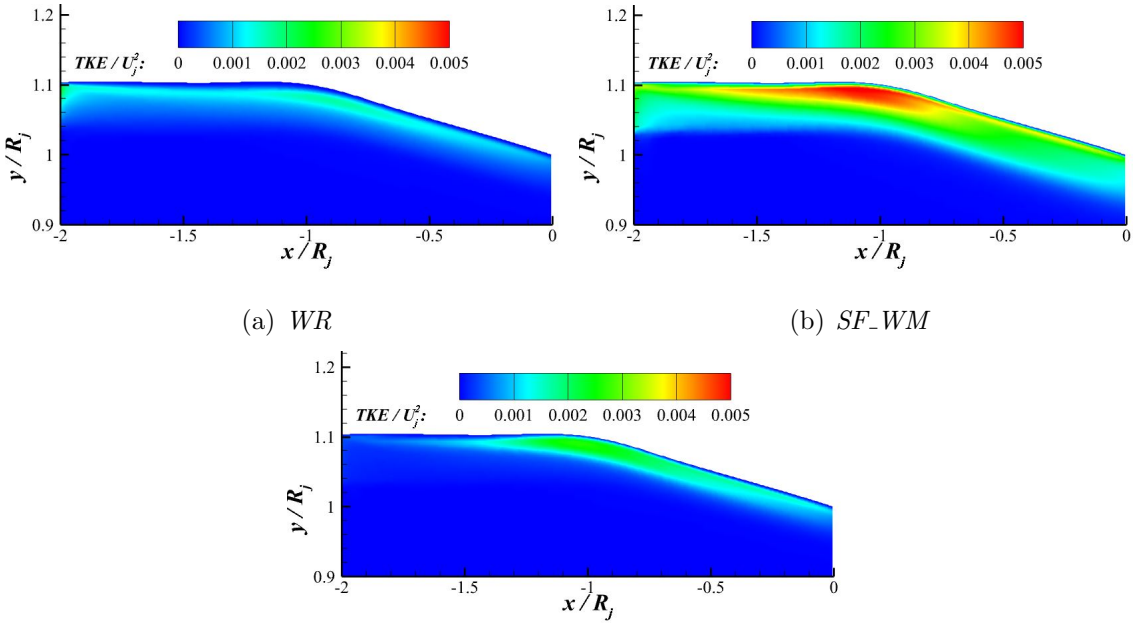

(a) *WR*

(b) *SF_WM*

(c) *SF_WM_LIT*

Figure 6.5. TKE contours close to the nozzle wall for the wall-modeled and wall-resolved simulations.

The flow characteristics downstream of the nozzle are examined by comparing the profiles along the centerline and lipline of the nozzle. The wall-modeled simulation results along the centerline are also compared with the experimental data of Bridges and Wernet [127] and Arakeri et al. [128] along with the wall-resolved simulation, similar to the comparison made by Aikens [45]. The nozzles and operating conditions used in the experiments are different from those of the simulations performed here. The experimental data of Bridges and Wernet is for the unheated jet (as opposed to the isothermal jet in the simulations) through the acoustic reference nozzle operating at Mach 0.98 and having a Reynolds number based on the diameter of approximately 1.5 million. Whereas the data from Arakeri et al. [128] are for a slightly heated jet

(TTR=1.13) through a nozzle operating at Mach 0.9 and having a $Re_D = 500,000$. Details about the nozzle are not provided by Arakeri et al. [128].

Table 6.4. Potential core lengths of the SMC000 nozzle simulations and related experiments.

Case	**Potential Core Length**
WR	$14.8R_j$
SF_WM	$16.7R_j$
SF_WM_LIT	$16.2R_j$
Bridges and Wernet	$16.0R_j$
Arakeri et al.	$15.3R_j$

The mean axial velocity along the centerline is plotted in figure 6.6(a). The results of the wall-modeled simulations match well with both the wall-resolved simulation and experimental results. However, the potential core length, defined as the length of the jet downstream of the nozzle exit where the velocity is greater than $0.95U_j$, is slightly different between the results. The potential core lengths are tabulated in table 6.4 for both the experiments and simulations. The trends seen between the *WR* and *SF_WM* cases are consistent with the findings of Bogey et al. [57], who noticed that an increase in turbulence levels at the jet exit lengthens the jet's potential core. The wall-modeled case *SF_WM* which has higher turbulence levels at the nozzle exit ends up with a longer potential core. That said, the turbulence levels in the BL for the *WM-LIT* case are similar to those of the *WR* case yet the potential core is longer.

The inverse of the centerline velocity is plotted against the Witze correlation [129], $W(x)$, in figure 6.6(b) to analyze the downstream decay rate. The Witze correlation is defined as

$$W(x) = 0.08(1 - 0.16M_j)\left(\frac{\rho_\infty}{\rho_j}\right)^{0.28}\left(\frac{x - x_c}{R_j}\right), \tag{6.1}$$

where x_c is the potential core length and M_j is the jet exit Mach number. For jets operating at different temperature ratios and Mach numbers, the Witze correlation

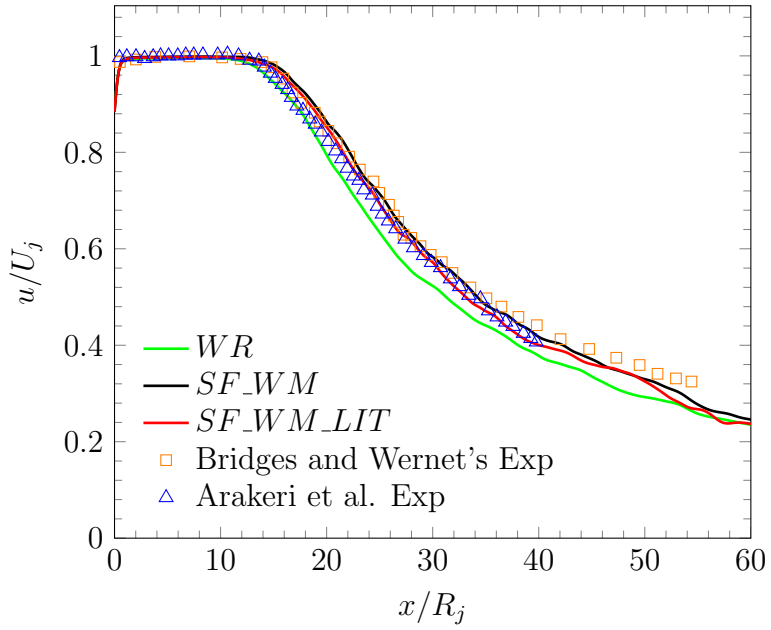

(a) Centerline velocity versus distance downstream from the nozzle exit.

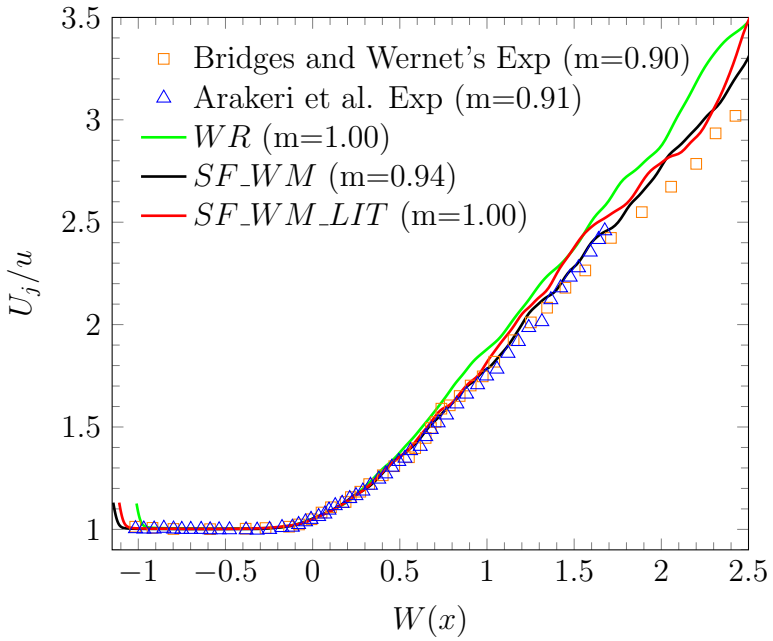

(b) Inverse centerline velocity versus the Witze correlation.

Figure 6.6. Comparison of centerline velocity results of the SMC000 nozzle wall-modeled simulations with the wall-resolved simulation and experiments.

collapses the centerline velocity data. The decay rates are close to each other for both the experiments and simulations. Furthermore, to compare the results quantitatively, the slope of the inverse velocity with respect to $W(x)$, m, is calculated for $0.5 < W(x) < 1.5$ and shown in the figure legend for each result. The jet of the *SF_WM* case decays very similarly to the experimental data. The computed slopes show similar velocity decay rates for the *WR* and *SF_WM_LIT* cases.

Finally, the rms of axial fluctuating velocity is plotted along the centerline and lipline in figure 6.7. Along the centerline, the three simulation results are very similar. However, the results of the *WR* case show a rapid increase in rms levels close to the nozzle exit. This is due to the higher turbulence levels along the lipline (plotted in figure 6.7(b)) for the *WR* case, which cause the shear layer to spread more rapidly leading to an increase in turbulence along the centerline and a shorter potential core. The limited statistical sampling might be the possible reason for the differences seen at the downstream locations along the centerline. The simulations compare well with the experimental data of Arakeri et al. but deviate from the experimental data of Bridges and Wernet at the downstream locations. Bridges and Wernet's data show higher levels at the downstream locations. Perhaps the different operating conditions of Bridges and Wernet's experiment from the other cases cause the discrepancies.

Figure 6.7(b) shows the rms of axial fluctuating velocity for the wall-modeled and wall-resolved cases along the lipline. There are slight variations of the u'_{rms} between the three simulations. The u'_{rms} of the *WR* case peaks higher and slightly downstream from the nozzle exit than that of the wall-modeled simulations. Although the differences in the exit turbulence levels between the *WR* and *SF_WM_LIT* are reduced, the u'_{rms} of the *WM-LIT* case still peaks lower than that of the *WR* case. The difference could be due to the slightly higher turbulence levels in the BL noticed at the nozzle exit for the *SF_WM_LIT* case compared to the *WR* case. These results show the sensitivity of the flow development in the shear layer due to the turbulence present in the BL at the nozzle exit. The trends noticed so far are per the findings of Bogey et al. [57] described earlier. The lengthening of the jet's potential core with

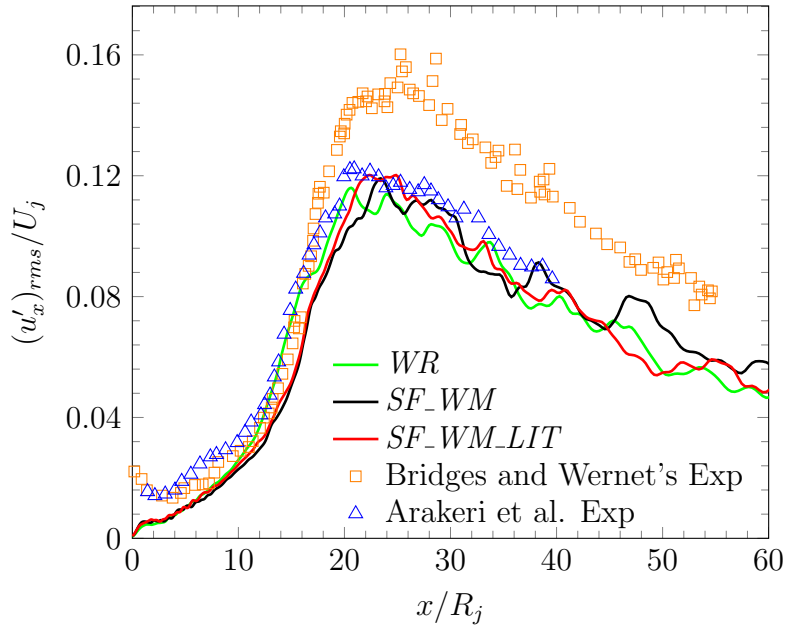

(a) Along centerline

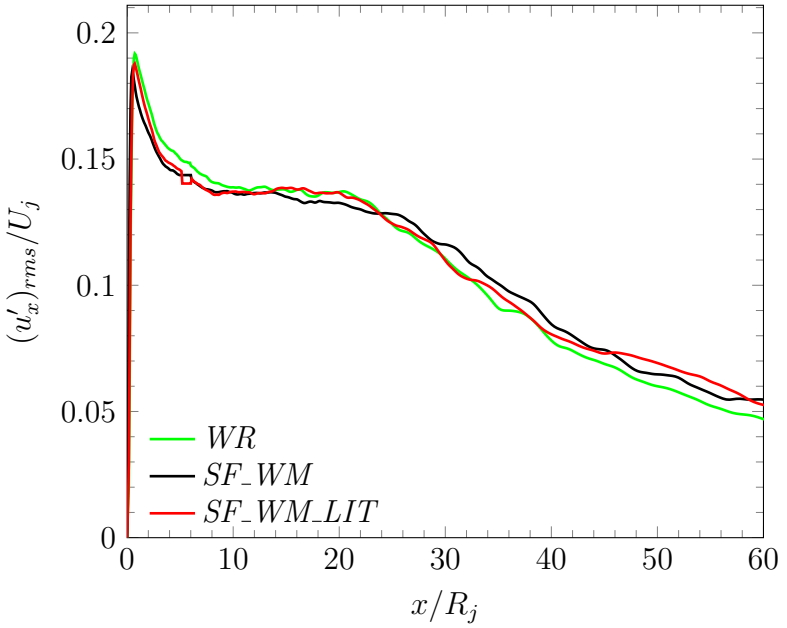

(b) Along lipline ($r = R_j$)

Figure 6.7. Comparison of rms of axial velocity fluctuations of the SMC000 nozzle wall-modeled simulations with the wall-resolved simulation and experiments (no data available along the lipline).

increased boundary layer turbulence at the nozzle exit has already been noted from the mean axial centerline velocity comparisons. Another trend seen here is of lower peak intensity in the shear layer with increased boundary layer turbulence at the nozzle exit. The propagated farfield noise is discussed next.

6.1.3 Discussion of the Farfield Acoustics Results

This section discusses the farfield acoustic results of the current wall-modeled simulations SF_WM and SF_WM_LIT and compares with the results of the wall-resolved simulation [48] and the experiments of Tanna et al. [56] and Brown and Bridges [17]. The experiments were conducted at a higher Reynolds number of 10^6. The SMC000 nozzle is used in the experiments of Brown and Bridges [17], whereas Tanna et al. use ASME nozzles in their experiments [130]. Only the acoustic results of the surface S_WM_1, shown in figure 6.2, are presented here for the current wall-modeled simulations. The surface S_WM_2 is a loose surface and is not able to capture the high frequency noise, resulting in an underprediction of the overall noise at the observer locations. Besides, the surface S_WM_3 shows the same trends as the surface S_WM_1. So, the results of surfaces S_WM_2 and S_WM_3 are not discussed for brevity.

The farfield acoustics of the simulations are computed using the FWH method along with the end-cap methodology from Ikeda et al. [98] as described in section 2.6. The noise at the farfield is computed at discrete observer locations which are positioned along an arc located at a distance of $144R_j$ from the nozzle exit, and varying at uniform intervals between $\Theta = 15°$ and $180°$. Here, Θ is the angle made by the observer with the downstream jet axis. The spectra and OASPL obtained at each observer location are also averaged in the azimuthal direction for smoothing. In the azimuthal direction, the farfield acoustics are computed at eight uniformly-spaced locations. The data is converted to dB using a reference pressure of 20 μPa along with $\rho_j = 1.23$ kg/m^3 and $U_j = 305$ m/s.

The sound pressure level (SPL) values from Brown and Bridges [17] are measured along an observer arc with a radius of $100R_j$. To compare with the acoustic data of Tanna et al. [56] and simulations, Brown and Bridges [17] data are scaled assuming spherical spreading to the observer radius of $144R_j$ using

$$\mathrm{SPL}_{\mathrm{new}} = \mathrm{SPL}_{\mathrm{old}} + 20\log_{10}\left(\frac{R_{\mathrm{old}}}{R_{\mathrm{new}}}\right). \tag{6.2}$$

Figure 6.8 shows the overall sound pressure level (OASPL) at various observer angles, Θ. The OASPL is computed using the one-third octave spectra for $St_{min} \leq St \leq St_{max}$. Comparing the *WR* and *SF_WM* cases, the maximum difference at any given observer angle between $15^\circ \leq \Theta \leq 130^\circ$ is limited to 1.09 dB. The noise levels of the *SF_WM* case underpredicts the *WR* case. This underprediction is due to the corresponding higher turbulence levels noticed in the boundary layer at the nozzle exit of the *SF_WM* case than the *WR* case. The acoustics and the corresponding flowfield data are consistent with the trends noticed by Bogey et al. [57] explained earlier. On the other hand, the *SF_WM_LIT* case shows higher noise levels than the *SF_WM* case and approaches levels of the *WR* case for most observer locations, except for $\Theta > 130^\circ$, with the maximum difference reducing to 0.64 dB for observers located between $15^\circ \leq \Theta \leq 130^\circ$. Due to the differences in the cutoff frequency between the simulations, the OASPL is also computed using one-third octave SPL for the limited range $St_{min} \leq St \leq 2$ for both experiments and simulations. These results are shown in figure 6.8(b). This comparison shows that for observers located between $15^\circ \leq \Theta \leq 130^\circ$, the maximum difference between the *WR* and *SF_WM* cases increases to 1.46 dB as opposed to 1.03 dB between the *WR* and *SF_WM_LIT* cases. The three simulations compare very well with the data from Brown and Bridges [17] except for observers at $\Theta < 40^\circ$. Differences exist between the simulation results and the experimental data of Tanna et al. [56] when the OASPL is computed using the data in the $St_{min} \leq St \leq St_{max}$ range. However, these differences are reduced when the OASPL is computed using the data only in the $St_{min} \leq St \leq 2$ range. This is especially true for the *WR* case, which compares well with the data of Tanna et al. at most of the observer locations, for $\Theta > 40^\circ$. The use of ASME nozzles

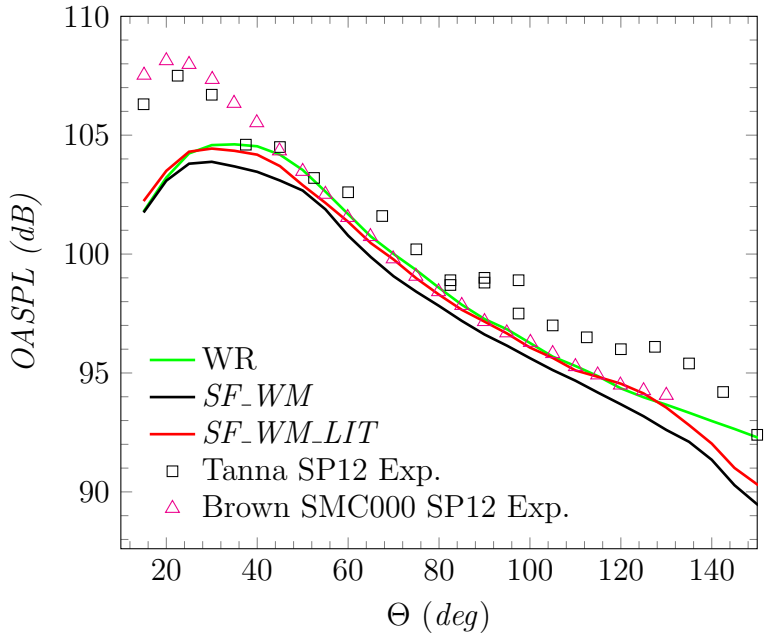

(a) $St_{min} \leq St \leq St_{max}$

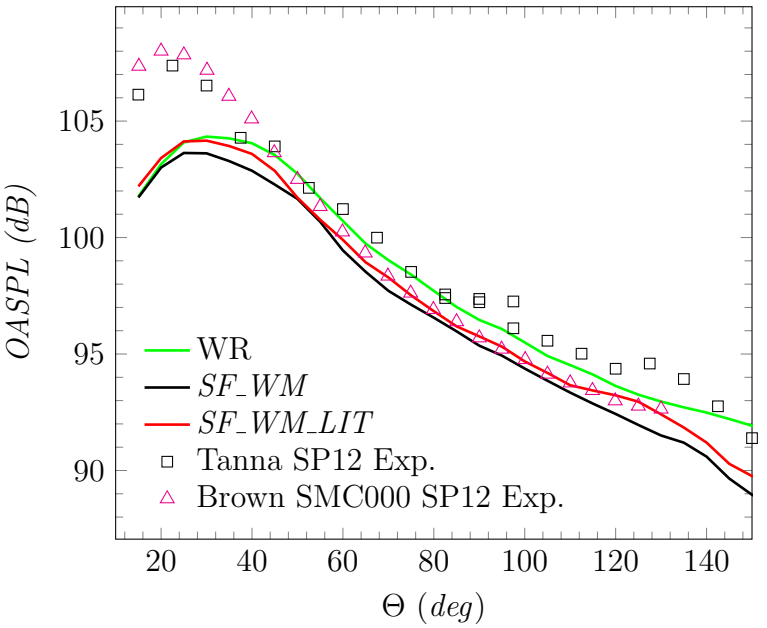

(b) $St_{min} \leq St \leq 2$

Figure 6.8. Comparison of OASPL at $R = 144R_j$ of the SMC000 nozzle wall-modeled simulations with the wall-resolved simulation and experiments.

featuring higher contraction ratios [131] in the experiments by Tanna et al. might have resulted in the developing boundary layer being laminar, leading to increased noise levels. While Tanna's OASPL data is louder than that of Brown and Bridges for $\Theta \geq 45°$, the peak noise level is lower. However, the spectrum at $\Theta = 30°$ discussed further below and presented in figure 6.9(a), shows that the peak in Tanna's spectrum is higher than that of Brown and Bridges and Tanna's low frequency noise levels are higher. Brown and Bridges spectrum is higher at higher frequencies and over a wider range of frequencies, leading to a greater value of OASPL. This behavior is consistent with the boundary layer in Tanna's experiment being quasi-laminar.

Finally, the one-third octave spectra are plotted for various observer angles, Θ, in figure 6.9 to provide better insight into the acoustic results. The plots show that the wall-modeled cases have a higher cutoff frequency than that of the wall-resolved case, which is likely due to the wall-modeled grid having a finer resolution on the ADS. It should be noted that the grid resolution dictates the maximum Strouhal number that can be resolved. This cutoff Strouhal number, $St_{g,max}$, can be approximated using equation 2.50. The trends seen here follow the observations noticed earlier in the OASPL. The higher turbulence intensities at the nozzle exit of the *SF_WM* case cause its sound pressure level (SPL) to be lower than that of the *WR* case. However, comparing the SPL between the *SF_WM* and *SF_WM_LIT* cases at higher observer angles, the noise levels are higher for the *SF_WM_LIT* case at higher Strouhal numbers. For all observer angles, the SPL of the *SF_WM_LIT* case fluctuates over the SPL of the *WR* case at lower Strouhal numbers. However, for larger observer angles, the SPL of the *SF_WM_LIT* case becomes louder and closer to that of the *WR* case at higher Strouhal numbers. Like the results of the OASPL, the one-third octave spectra of simulations are closer to the experimental data of Brown and Bridges [17] than the data of Tanna. Tanna's data is louder than Brown and Bridges data, especially at higher frequencies. Similar discrepancies are also noted by other researchers [130–132]. The differences between the experiments are attributed to the state of the boundary layer at the nozzle exit by Karon and Ahuja [130]. In the current context, it is essential

that the simulations reproduce the experimental boundary layer to predict the noise accurately. Unfortunately, the state of the boundary layers inside the nozzle is not available for the current flow condition making it hard to validate the simulations with experiments.

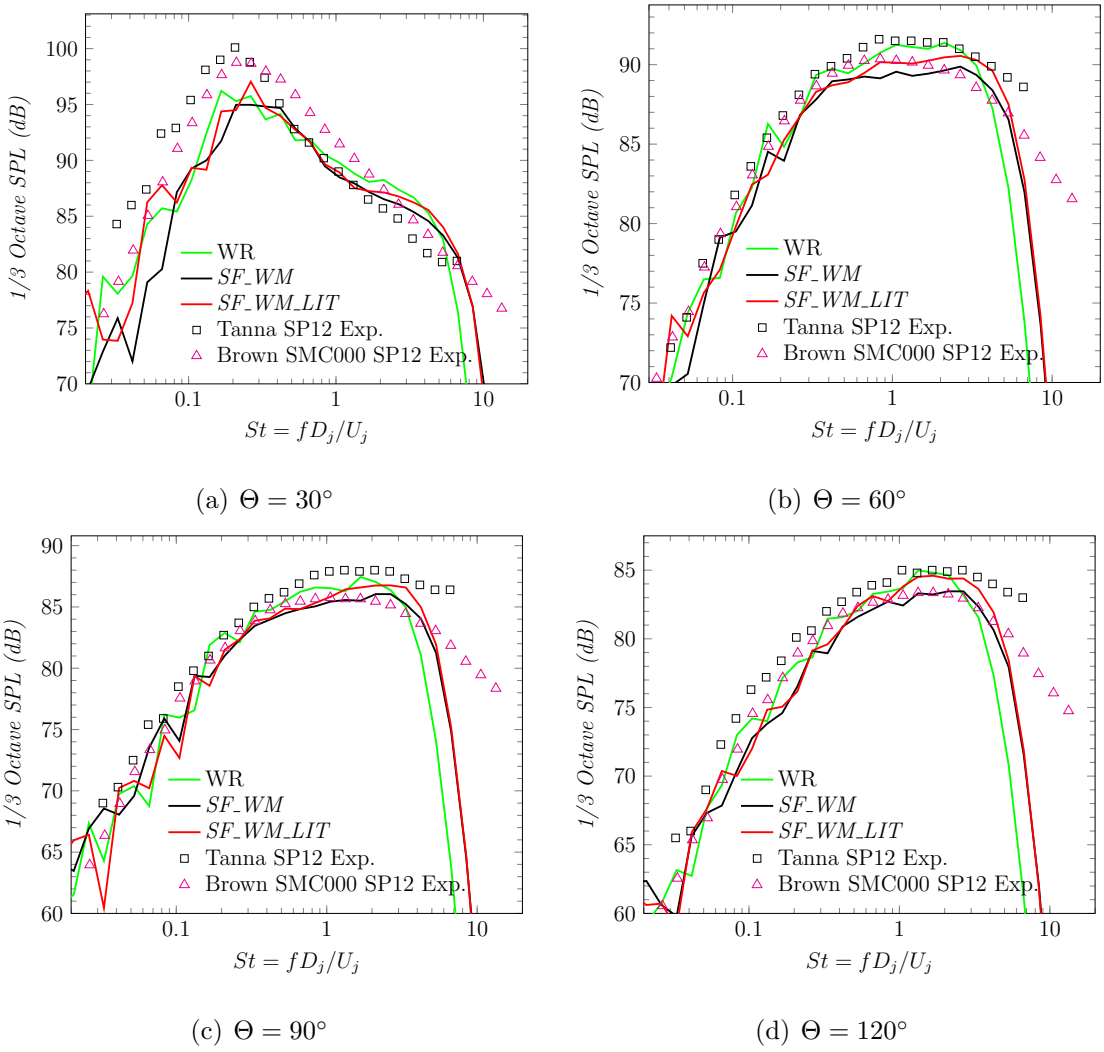

(a) $\Theta = 30°$ (b) $\Theta = 60°$

(c) $\Theta = 90°$ (d) $\Theta = 120°$

Figure 6.9. Comparison of One-third octave spectra at $R = 144R_j$ of the SMC000 nozzle wall-modeled simulations with the wall-resolved simulation and experiments.

The largest discrepancies between the simulations and experiments noticed in the OASPL results for low observer angles can be further analyzed from the spectra at $\Theta = 30°$ plotted in figure 6.9(a). In comparison with the experiments, at

lower Strouhal numbers, the simulation results show an underprediction of the SPL whereas the simulations, especially the *WR* and *SF_WM_LIT* cases, overpredict for $2 < St < 6$. The overprediction can also be noticed at other observer angles. As described by Aikens [45], the reasons for the differences at lower Strouhal number are still unknown and need further study by varying grid resolution, Reynolds number, and boundary layer thickness. Additionally, it would also be worthwhile to collect statistics for more extended times so that there would be ample time for the low frequency pressure signatures to be collected on the ADS resulting in smoother spectra. Similar discrepancies at lower observer angles are also reported in references [95, 133]. However, some insight can be drawn from the studies of Bogey et al. [134] to understand the discrepancies at higher Strouhal numbers. Bogey et al. carried out nozzle simulations by perturbing laminar boundary layers over a range of Reynolds numbers to study the effect of Reynolds number on the computational results. Their results show that with an increase in Reynolds number, the noise is reduced over a range of frequencies at higher observer angles, whereas at lower observer angles, only noise at higher frequencies is reduced. So, the use of a lower Reynolds number in the current simulations could have caused the differences with the experiments at higher Strouhal numbers. Given the above discussion, and the significant impact on the radiated noise due to subtle changes in the nozzle exit conditions, it is essential for the experimental research community to measure detailed flow conditions at the nozzle exit along with the farfield noise. Having such experimental datasets would be helpful for future comparisons between simulations and experiments.

6.1.4 Summary and Conclusions

In this work, two wall-modeled simulations using the generalized equilibrium wall-model were completed for a Mach 0.9 isothermal jet through an SMC000 nozzle [8]. A Reynolds number of $Re_{Dj} = 100,000$ is used in the simulations. The results of the simulations are compared and validated with the similar wall-resolved LES simula-

tion [48], experimental flowfield [127,128] and acoustic data [17,56]. Differences exist between the wall-modeled simulations and the wall-resolved simulation. However, given the cost-benefit of the wall-modeled simulation over the wall-resolved simulation, the results seem to be acceptable. Compared to the wall-resolved simulation, the wall-modeled simulation that uses similar turbulent inflow conditions, the case *SF_WM*, shows larger turbulent fluctuations in the boundary layer, a longer potential core, and noise levels that are systematically lower with a maximum difference of 1.46 dB. For higher boundary layer turbulence levels at the nozzle exit, however, all of these trends are expected based on the study by Bogey et al. [57]. The second wall-modeled case, *SF_WM_LIT*, was simulated by reducing the velocity and density fluctuations added to the mean flow at the nozzle inflow to more closely match the wall-resolved Reynolds stress profiles at the nozzle exit. This improves the flowfield and acoustic data to an extent but does not fully resolve the differences. The length of the potential core, for example, is shortened but not to that of the wall-resolved case. The noise levels also match more closely with the wall-resolved simulation especially at shallow and larger observer angles, and the maximum difference is reduced to 1.03 dB.

The *SF_WM_LIT* case shows similar trends like the wall-resolved case, compare reasonably well with the available experimental data for observers located between $40^\circ \leq \Theta \leq 130^\circ$. At shallow observer angles for $\Theta < 40^\circ$, large differences exist between the *SF_WM_LIT* case and the experiments. These differences are also noted in the wall-resolved simulation. Various factors such as the differences in the Reynolds number and exit flow conditions of the experiments could be possible reasons for the discrepancies. Similar simulation errors are also noticed by other researchers [95, 133, 135]. Overall, given the cost advantage of the wall-model simulations, they performed well in comparison with both the wall-resolved simulation and experiments. While using the wall-models, the approach of controlling the inflow fluctuation levels added to the mean inflow helped in predicting the acoustic results which are on par with the wall-resolved simulation. It is therefore suggested that the wall-model

in combination with the control of turbulence levels at the inflow seems to be an efficient approach for jet noise studies until a more effective wall modeling method is developed, possibly employing an explicit SGS model.

6.2 Wall-modeled Simulations at SP07 Operating Conditions

This section discusses the wall-modeled LES simulations of a Mach 0.9832 jet through an SMC000 nozzle operating at a Reynolds number of $Re_{Dj} = 10^6$. The operating condition corresponds to the SP07 test condition designated by Tanna et al. [56]. The SP07 operating condition is given in table 6.5. Unlike the isothermal condition of SP12, the SP07 operating condition corresponds to an unheated jet. The Reynolds number used here is similar to what is used by Dhamankar et al. [136] for the SP07 case. Dhamankar et al. [136] carried out an SMC000 nozzle wall-modeled simulation on a higher resolution grid consisting of 330 million grid points using an immersed boundary method. An immersed boundary method was incorporated into the modular LES code by Dhamankar et al. [136]. Due to the unavailability of experimental data at the nozzle exit, Dhamankar et al. [136] set up the simulation initially by comparing with the published experimental results available at $x = 8R_j$. They were able to obtain a good agreement between the mean and rms fluctuating velocity in the axial direction is obtained.

However, when later compared with more complete unpublished experimental data, it was found that the simulation of Dhamankar et al. [136] has a thinner shear layer and higher turbulence levels in the shear layer just downstream the nozzle exit, thereby leading to underprediction of noise in comparison with the experiments. So, in the current work, similar to the preliminary analysis carried out for the SMC000 nozzle operating at the SP12 condition, preliminary simulations are carried out at the SP07 operating condition. The boundary layer thickness, $\delta_{99,i}$ in these simulations is double than what was used by Dhamankar et al. in their LES simulation. This is to match the shear layer thickness with the data from the experiment [62] at $x = 0.2R_j$.

Table 6.5. SP07 Operating conditions used for SMC000 nozzle simulations.

Parameter	**Value**
Acoustic Mach number at nozzle exit ($M_a = U_J/c_\infty$)	0.9000
Mach number at nozzle exit ($M_J = U_J/c_J$)	0.9832
Nozzle exit to ambient static temperature ratio (T_J/T_∞)	0.8380
Dimensional ambient temperature(T^*_∞)	293 K
Nozzle temperature ratio (TTR $= T_0/T_\infty$)	1 (Unheated jet)
Nozzle pressure ratio (NPR $= p_0/p_\infty$)	1.8563
Reynolds number at nozzle exit ($Re_{D_J} = \rho_J U_J D_J/\mu_J$)	10^6

The velocity and density fluctuations added to the inflow are also adjusted to match the experimental data at locations just downstream of the nozzle exit.

Therefore, a total of three wall-modeled simulations were carried out using a short domain. The first simulation referred to as *SS_7* is identical to the settings of the LES simulation of Dhamankar et al., except for the boundary layer thickness. Unlike the simulation of Dhamankar et al., the *SS_7* case does not use the immersed boundary method. The other two cases are carried out by halving and doubling the velocity and density fluctuations added to the inflow in comparison with the *SS_7* case. These cases are referred to as *SS_7_TURB_0.5* and *SS_7_TURB_2*, respectively.

As mentioned earlier, based on the results of the preliminary simulations, a simulation using an extended domain of the SMC000 nozzle operating at the SP07 condition was planned for noise predictions. However, the changes made in the settings of the preliminary simulations did not produce the desired experimental flowfield results consistently for all streamwise locations. The results are discussed later. Therefore, noise prediction for an SMC000 nozzle operating at the SP07 condition using an extended domain is not carried out. The following sections present more details of the preliminary simulations set up along with their results.

Table 6.6. Remaining simulation settings used in the wall-modeled SMC000 SP07 preliminary simulations.

Time Details	
Time step size, Δt (T)	9×10^{-4}
Transient period (T)	40
Statistics gathering period (T)	40
Max CFL Numbers (x, r, θ)	(0.38, 1.12, 0.73)
Machine Details	
Machine	TACC Stampede 2
Cores	1008
Cores per node	48
Cost (node-hours)	100

6.2.1 Preliminary Simulations Setup

The computational domain and boundary conditions used for the current simulations are similar to the ones used earlier as described in section 4.2.1. The generalized equilibrium wall-model is applied on the inner wall of the nozzle. As mentioned earlier, a boundary layer thickness of $\delta_{99,i} = 0.14R_j$ is used in the current set of simulations. The integral length scales are set to $\{1.28, 0.25, 0.25\}\delta_{99,i}$ in the streamwise, radial and azimuthal directions. These values are similar to those used in the LES simulation of Dhamankar et al. [136]. The dimensional ambient temperature is assumed to be $T^*_\infty =$ 293 K. The coarse grid described in section 4.2.2 is used here as well. Table 6.6 shows the additional settings used in the simulations. The times shown in the table are in terms of the reference time $T = R_j/U_j$. A time-step size of $\Delta = 0.9 \times 10^{-4}R_j/U_j$ is used. All the simulations were completed on the Stampede 2 machine located at TACC.

6.2.2 Discussion of the Results of the Preliminary Simulations

This section discusses the results of the preliminary SMC000 nozzle simulations operating at the SP07 condition. The results are compared with the numerical results of Dhamanakar et al. [136] and experimental data of Bridges and Wernet [62]. The experimental Reynolds number based on jet diameter is estimated to be $Re_{Dj} \approx 1.43 \times 10^6$. As with the other nozzle simulations, the statistical quantities presented are averaged both in time and in the azimuthal direction. For brevity, only the mean velocity in the streamwise direction and turbulent kinetic energy are shown in this section.

Figure 6.10 shows the mean streamwise velocity profiles in the radial direction at various streamwise locations. No experimental data are available at the nozzle exit. The domain in the current simulation extends to $x = 5R_j$ only. So, comparisons of the present simulations are made with the reference data from the nozzle exit to a streamwise location at $x = 4R_j$. At the nozzle exit, the profiles of the current simulations are slightly different from that of the reference LES. This is likely due to the increase in the boundary layer thickness imposed at the inflow for the current simulations. It is also possible that the finer mesh used in the reference LES could be the reason for the differences seen here. However, the results of the simulations are close to each other. Further downstream at $x = 0.2R_j$, the location where the experimental data is available close to the nozzle exit, the reference LES shear layer is thinner than that of the experiment. Increasing the inflow boundary layer thickness does not help in increasing the shear layer thickness of the current simulations. Further downstream, the profiles of the simulations match better in comparison with the experiments. The change in velocity and density fluctuation added to the inflow does not affect the mean velocity profiles in the current simulations.

As with the mean streamwise velocity, the turbulent kinetic energy is also compared with the reference data at various streamwise locations, as shown in figure 6.11. At the nozzle exit, the reference LES data has a higher TKE than that of the *SS_7*

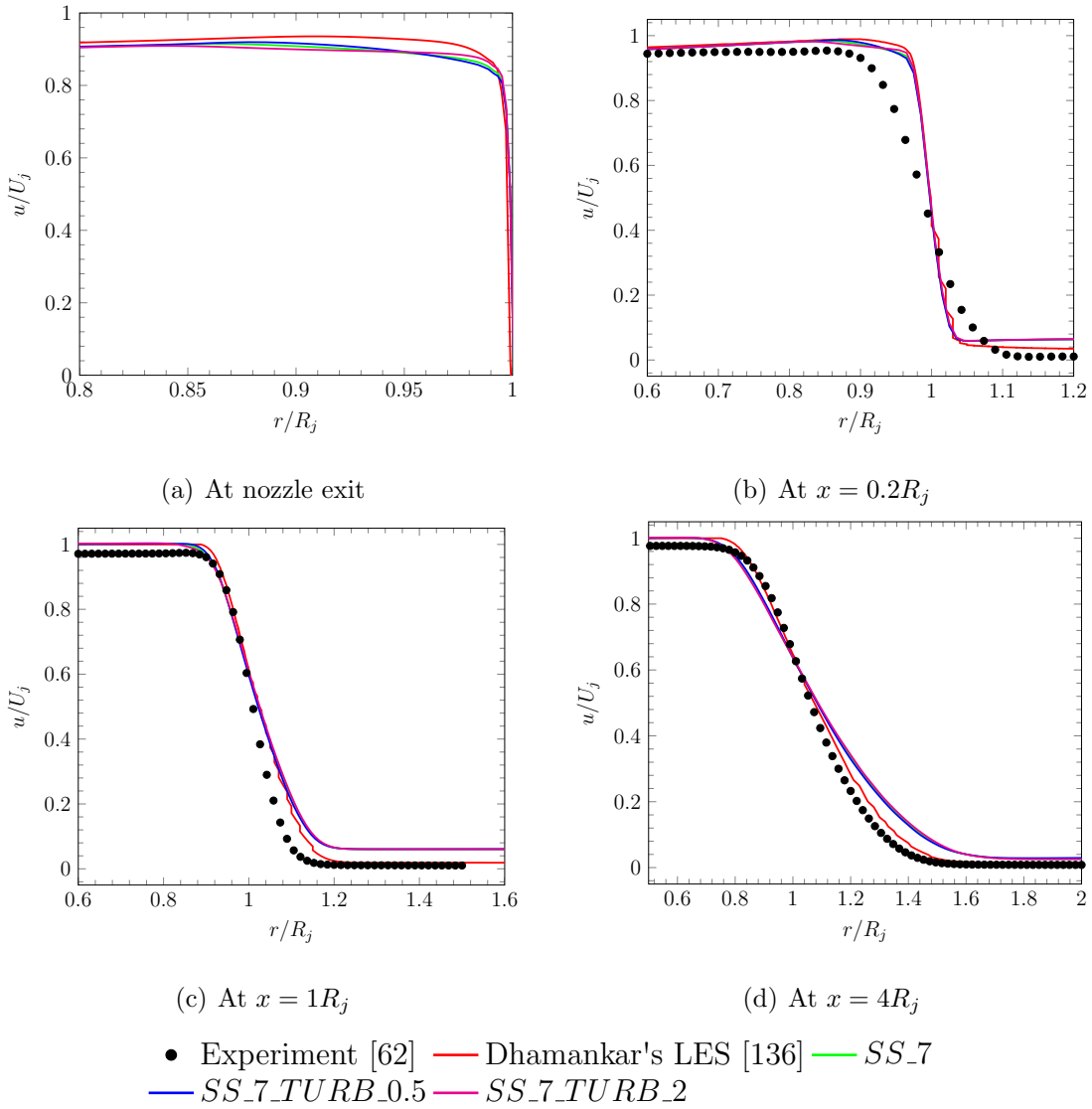

Figure 6.10. Comparison of the mean streamwise velocity profiles at various streamwise locations for the SMC000 nozzle.

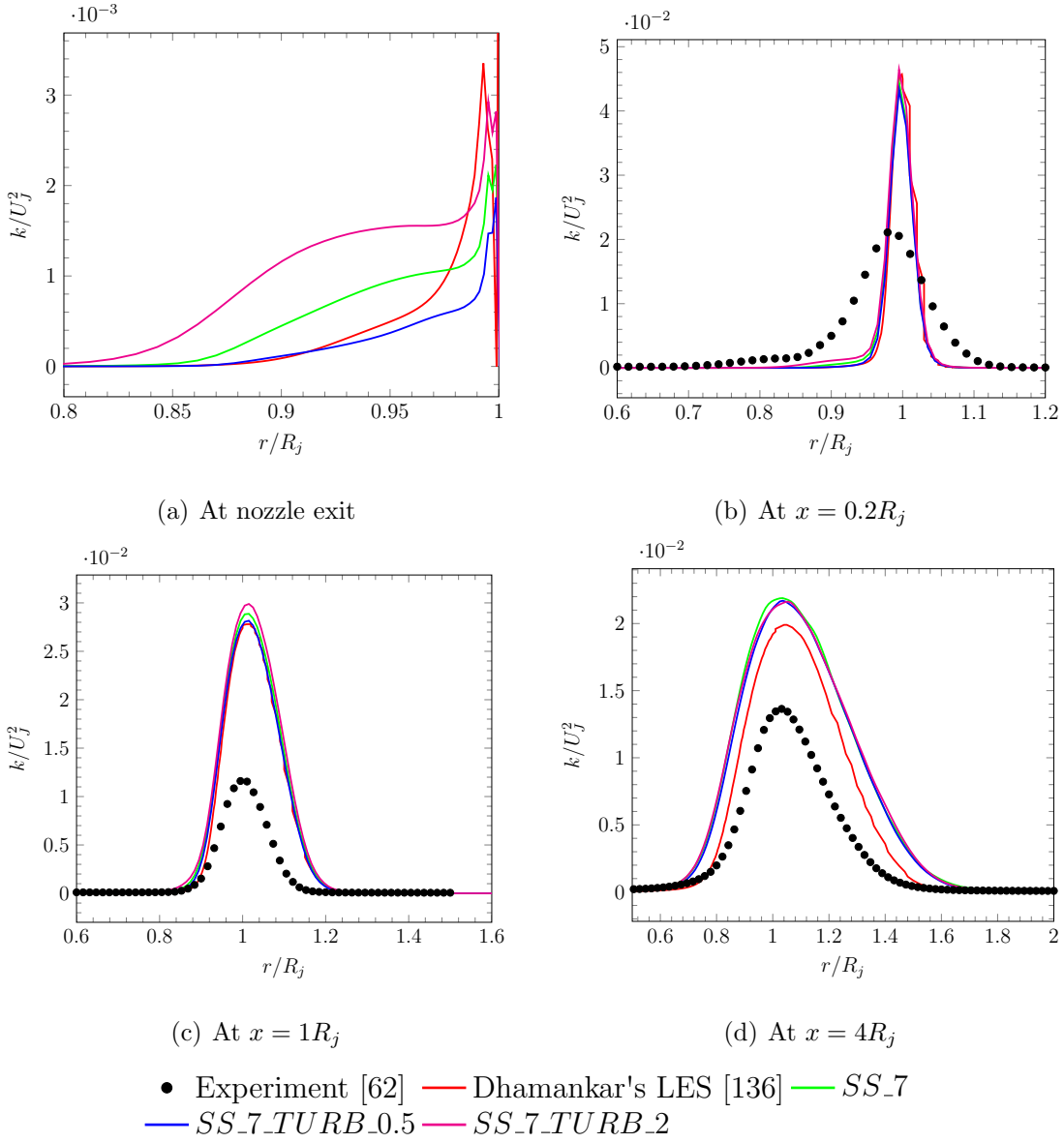

Figure 6.11. Comparison of turbulent kinetic energy profiles at various streamwise locations for the SMC000 nozzle.

case. The TKE of *SS_7_TURB_0.5* and *SS_7_TURB_2* are lower and higher respectively compared to the *SS_7* case. This is per the reduction and increase of velocity and density fluctuations added to the mean flow at the inflow for the *SS_7_TURB_0.5* and *SS_7_TURB_2* cases respectively. However, as the flow propagates downstream, the TKE is almost the same in all the simulations when compared with the experimental data. At $x = 4R_j$, the TKE of the reference LES is slightly lower than the current simulations. This could be due to the differences in grid resolution between the current simulations and the reference LES. The grid used in the reference LES has a very fine resolution in comparison with the grid used in the current simulations. The earlier SMC000 SP12 simulations followed the trends noticed by Bogey et al. [57], who found that turbulence levels in the developing shear layer decrease with increases in the boundary layer turbulence levels at the nozzle exit and vice-versa. However, unlike in the previous nozzle simulations, the approach of controlling the velocity and density fluctuations added to the inflow does not help in affecting the TKE in the developing shear layer. The high Reynolds number and the Mach number being closer to sonic condition could be factors that diminish the influence of the inflow turbulence levels on the flow developing downstream.

6.2.3 Summary and Conclusions

In this work, three wall-modeled simulations using the generalized equilibrium wall-model were completed for a Mach 0.9832 unheated jet through an SMC000 nozzle [8]. A Reynolds number of $Re_{Dj} = 10^6$ is used in the simulations. The results of the simulations are compared and validated with a similar wall-modeled LES simulation from Dhamankar et al. [136] and experimental flowfield data [62]. Differences exist between Dhamankar's LES and the experiment. The shear layer thickness and the turbulent kinetic energy near the nozzle exit of the simulation are different from that of the experiment. In an attempt to match the experimental flowfield conditions, the boundary layer thickness used in the current simulations is double what is

used by Dhamankar et al. In addition, the velocity and density fluctuations added to the mean flow at the inflow are also varied between the three simulations performed here. Although the changes have an impact at the nozzle exit, the flowfield developing downstream of the current simulations show characteristics similar to that of Dhamankar's LES. This behavior is unlike the jets that operate at Mach 0.9 and have a Reynolds number of 10^5 simulated earlier, which are affected by the changes made to the velocity and density fluctuations at the inflow. This shows the limitation of the approach of modifying the velocity and density fluctuations at the inflow to match the experimental turbulence levels near the nozzle exit which eventually affect the noise predictions. Further studies would therefore be necessary to understand how the Mach number and Reynolds number influence the developing shear layer. Since none of the current preliminary simulations reproduce the experimental flowfield data, the initial plan to simulate a jet through the SMC000 nozzle operating at SP07 conditions for noise prediction using the best performing preliminary simulation settings is forfeited.

7. SUMMARY AND RECOMMENDATIONS FOR FUTURE WORK

7.1 Summary

The cost advantage of the wall-modeled LES over the wall-resolved LES makes the use of wall-models vital to control the costs of the already expensive LES simulations required for jet aeroacoustics. At the same time, the stresses supplied by these models should be accurate enough to maintain the fidelity of the simulations. Most of the nozzle design concepts used for noise reduction show less than 4dB noise reduction in noise peak amplitude. However, the wall-modeled SMC000 simulation underpredicts the noise by 1.3 dB compared to its counterpart wall-resolved simulation [45]. This accounts for over 25% of the noise difference noticed due to the use of various noise reduction techniques. Therefore, the current study is focused on understanding the cause of the differences and improving the fidelity of the wall-modeled LES for jet aeroacoustics.

The first part of the study is focused on assessing the modular-LES code [45–49] by carrying out preliminary SMC000 wall-modeled simulations using a short domain operating at the SP12 condition [56]. The condition corresponds to a Mach 0.9 isothermal jet and the Reynolds number based on diameter used in the LES is 10^5. Multiple simulations were performed by varying the integral length scales and velocity fluctuations at the inflow, the wall-model formulation, and the grid compared to what was used in the reference wall-modeled SMC000 simulation [45]. The near-field statistics presented show that varying the integral length scales and wall-model has a negligible impact on the flowfield. The integral length scales are modified to match those of the reference wall-resolved simulation [48]. The first grid point off the inner nozzle wall is located below the logarithmic law region, where the equilibrium wall

model (EWM) is not valid, leading to the prediction of incorrect values of the wall-shear stress. Therefore, a new wall-model, the generalized equilibrium wall model (GEWM) [29], is implemented in the modular-LES code and tested. The GEWM extends the validity of the current EWM, which is only valid in the log-law region of a turbulent boundary layer that is in equilibrium, to include the viscous sub-layer and buffer region as well. Lowering of the velocity fluctuations at the inflow and refining the grid help in reducing the excessive amplitude of the Reynolds stresses at the nozzle exit. The Reynolds stresses at the nozzle exit are reduced to levels similar to those of the wall-resolved simulation. However, by altering the velocity fluctuations, the wall-modeled LES is no longer predictive, and multiple simulations have to be carried out to match the Reynold stresses in the shear layer with experimental data (if available) to obtain better acoustics predictions. On the other hand, refining the grid increases the simulation cost and may defeat the purpose of wall-modeling. These disadvantages show the need to further reassess the wall-models used.

The accelerating flows encountered in nozzle flows have developing boundary layers that deviate from an equilibrium state. Therefore, two new non-equilibrium wall-models are implemented into the modular-LES code and verified along with the existing wall-models based on the equilibrium assumption. The new wall-models are the generalized non-equilibrium wall model (GNEWM) given by Shih et al. [33, 60] and integral wall-model (IWM) of Yang et al. [61]. The wall-models are applied to two non-canonical flows and verified. They are the flow through a converging-diverging channel and a spatially developing accelerating boundary layer.

The results presented for the spatially developing accelerating boundary layer show that the mean velocity is found to be insensitive with the grid-refinement performed in the wall-normal direction. Whereas other results, such as the skin-friction, Reynolds number based on momentum thickness, and Reynolds shear-stress, vary with grid resolution, but show similar behavior as that of the reference data. A grid-independent solution is not achieved with the utilized grids for the results that are affected. A moderately refined grid that is both cost-effective and produces rea-

sonable results among the grids used was chosen for the later simulations. All the wall-models perform well in the non-acceleration region but not in the acceleration region. The non-equilibrium wall-models used also do not provide an improvement and produced results similar to those of the equilibrium wall-models. None of the wall-models capture the deviation of the mean velocity from the logarithmic law to laminar-like profiles in the acceleration region noticed in the reference data. This is likely due to the overprediction of the skin-friction in the acceleration region. The choice of the matching point location also does not affect the results. It is suspected that the non-equilibrium contributions in the GNEWM and IWM wall-models could have been suppressed due to the relatively low Reynolds number of the flow making these wall-models ineffective.

The case with flow through a converging-diverging channel operates at a higher Reynolds number than that used in the spatially developing accelerating boundary layer case. The skin-friction predicted by each of the wall-models demonstrate the response of the wall-models to the developing flowfield. The IWM performs better than the other wall-models used. The current wall-modeled simulations and the DNS show a few discrepancies. The results are seen to improve with increased grid resolution. The finer grid utilized captures the flow dynamics better than the coarse grid. However, the grid used is still unable to capture the flow separation noticed in the DNS. The mean velocity, turbulent kinetic energy (TKE) and Reynolds shear stress are seen not to be impacted by the wall-model used. A test using the wall-shear stress from the DNS slightly improved the results but did not adequately address the differences. The TKE and Reynolds shear stress are over-predicted in all of the cases. It could be possible that the implicit LES (ILES) approach used in the current simulations does not effectively dissipate the turbulence near the wall, leading to higher turbulence levels. The effectiveness of the ILES, which lacks an SGS model, is tested by performing a simulation using the dynamic Smagorinsky model (DSM) [66]. However, the use of an explicit SGS model predicts results similar to those of the case using the ILES methodology.

Two wall-modeled SMC000 simulations for noise predictions were carried out using the GEWM along with adjusting the inflow velocity and density fluctuation levels. Since the approximate boundary conditions supplied by the wall-models are not effective, the GEWM being economical among the implemented wall-models is chosen in these simulations. A grid with 101 million grid points is utilized. The simulations operate at the SP12 condition and have a Reynolds number of $Re_{Dj} = 10^5$. The results are compared and validated with the similar wall-resolved LES simulation [48], experimental flowfield [127,128] and acoustic data [17,56]. The case *SF_WM* was simulated using similar settings to those of the wall-resolved case. The *SF_WM_LIT* case was simulated by reducing the velocity fluctuation levels by 65% compared to the first case, while the other settings are left unchanged. Similar to the reference wall-modeled SMC000 simulation [45], the *SF_WM* case shows larger turbulent fluctuations in the boundary layer, a longer potential core, and noise levels that are systematically lower with a maximum difference of 1.46 dB for observers located between $15^\circ \leq \Theta \leq 130^\circ$ in comparison with the wall-resolved case. Decreasing the inflow velocity fluctuation levels improves the noise predictions of the *SF_WM_LIT* case in comparison to the wall-resolved case. The noise levels between the wall-modeled and wall-resolved cases now match better at shallow and larger observer angles, and the maximum difference is reduced to 1.03 dB for observers located between $15^\circ \leq \Theta \leq 130^\circ$. The simulation results compare reasonably well with the reference experiment data for observers located between $40^\circ \leq \Theta \leq 130^\circ$. As with the wall-resolved simulation, large differences still exist between the wall-modeled cases and the experiments at shallow observer angles for $\Theta < 40^\circ$. Various factors such as the differences in the Reynolds number and exit flow conditions of the experiments could be possible reasons for the discrepancies. Similar simulation errors are also noticed by other researchers [95, 133, 135].

The approach of using the GEWM in combination with adjusting the inflow velocity and density fluctuations, however, is found not to be effective from the preliminary SMC000 wall-modeled simulations operated at the SP07 condition [56]. It was planned to carry out noise predictions at this operating condition as well due to the

availability of both flowfield and acoustic experimental data. The SP07 condition is an unheated jet with a higher Mach number and Reynolds number compared to the SP12 condition. A Mach number of 0.9832, and a Reynolds number of $Re_D = 10^6$ are used in the simulations. Varying the inflow velocity fluctuations impacts the flow at the nozzle exit. However, unlike the SP12 cases, the downstream flowfield development for all the SP07 cases show similar characteristics. The tests carried out do not help in matching the experimental flowfield data near the nozzle exit. Comparing to the SP12 simulations, a higher Mach number which is close to sonic conditions, and a Reynolds number that is higher by an order of magnitude are used in the SP07 simulations. These could be possible factors in the observed differences in behavior. Further analysis would be needed to determine whether differences in Mach number and Reynolds number are the cause of the differences in the observed behavior. Since the approach of varying the inflow velocity and density fluctuations is unable to reproduce the experimental flowfield, it is not worthwhile to carry out simulations for noise prediction at the SP07 operating condition. The farfield acoustics are very dependent on the developing shear layer and it is not possible to capture the noise as in the experiments without matching the flowfield. Therefore, simulations for noise predictions are not performed at this operating condition.

Overall, it can be concluded that wall-modeled LES can predict reasonable results at a cheaper cost than wall-resolved LES. For jet noise predictions, the use of a simple equilibrium wall-model in combination with controlling the inflow velocity and density fluctuations are sufficient to produce results which are on par with the wall-resolved results. However, the approach has limitations and it does not provide improved predictions in all cases. The performance of the method may be dependent on the Mach number and Reynolds number of the flow being considered. Based on the current simulations, dependency on these quantities has not been substantiated yet. Until a more effective approach is found or developed for use with wall-modeled LES, the suggested postdiction process seems to be a possible option. Alternatively, a RANS solver can be used to predict the mean flow and Reynolds stresses at the

nozzle exit and then the LES can be performed by adjusting the inflow boundary conditions to match the RANS solution at the exit. This approach would be a predictive methodology that does not depend on experimental data.

7.2 Recommendations for Future Work

The issue of what SGS model is used should be investigated further to see whether it makes a difference in the behavior of the LES. It is worth implementing and testing various SGS models that are available. Such research may help in lowering of the turbulent kinetic energy noticed in the current wall-modeled simulations and produce results similar to reference data. When using SGS models with model constants, for better predictions, it is necessary to calibrate the model constants for each problem type [126]. When utilizing coarse grids, the dissipation is not modeled accurately by the SGS models due to them not accounting for the near-wall anisotropic turbulence [123]. Therefore, research into the development of SGS models that can be utilized with coarse grids is worthwhile. It is also useful to look into the SGS models allowing backscatter. Such models allow the backward energy transfer from subgrid scales to resolved scale. The use of an explicit SGS model also impacts the noise spectra at both high and low frequencies [71]. The noise predictions are improved at lower frequencies, whereas the SGS model has a detrimental effect on the high-frequency part. Therefore, care must be taken in choosing an appropriate model for aeroacoustic studies.

The tensor transformation of Sondak and Pletcher [105] used in the current wall-model implementation to transform the stresses from generalized coordinates to Cartesian coordinates could be replaced and tested with some other approach. Such an investigation may be helpful to verify or improve the accuracy of fluxes being computed at the wall boundary. For example, Chen [123] utilize the wall-shear force as a source term in the momentum equation. The wall-shear stress given by the wall-model is used to compute the wall-shear force.

The digital-filter based inflow boundary condition that is available in the modular-LES code requires the specification of five primitive variables. However, the use of five primitive variables is unphysical. Moreover, the boundary condition also requires a redevelopment region for the artificial turbulence to develop into physical turbulence. However, the specification of the redevelopment region is not possible when mean profiles from DNS or RANS are used at the inflow to match the related simulations. So, an alternate approach should be researched to address the two issues.

REFERENCES

[1] S. Martens and J. T. Spyropoulos. Practical jet noise reduction for tactical aircraft. ASME Paper GT2010-23699, ASME Turbo Expo 2010, Glasgow, UK, 2010.

[2] C. Tam, K. Viswanathan, K. Ahuja, and J. Panda. The sources of jet noise: experimental evidence. *Journal of Fluid Mechanics*, 615:253, 11 2008.

[3] S. Pope. *Turbulent Flows*. Cambridge University Press, 2000.

[4] D. Bodony and S. Lele. Current status of jet noise predictions using large eddy simulation. *AIAA Journal*, 46(2):364–380, February 2008.

[5] A. Lyrintzis. Surface Integral Methods in Computational Aerocoustics: From the (CFD) Near-Field to the (Acoustic) Far-Field. *International Journal of Aeroacoustics*, 2(2):95–128, 2003.

[6] Anastasios S. Lyrintzis. Review: The Use of Kirchhoffs Method in Computational Aeroacoustics. *Journal of Fluids Engineering*, 116(4):665, 1994.

[7] P. Di Francescantonio. A new boundary integral formulation for the prediction of sound radiation. *Journal of Sound and Vibration*, 202(4):491–509, 1997.

[8] J. Bridges and C. Brown. Parametric testing of chevrons on single flow hot jets. Technical memorandum 213107, NASA, 2004.

[9] J. Bridges and M. Wernet. Cross-Stream PIV Measurements of Jets with Internal Lobed Mixers. AIAA Paper No. 2004-2896, May 2004.

[10] R. Powers, M. Senft, and D. McLaughlin. Acoustics measurements of scale models of military style supersonic beveled nozzle jets. AIAA Paper No. 2011-2702, June 2011.

[11] J. Seiner, B. Jansen, and N. Murray. Aero-Performance Efficient Noise Suppression of a Supersonic Model Twin Jet Nacelle. AIAA Paper No. 2009-3130, May 2009.

[12] A. Pilon, D. McLaughlin, P. Morris, and R. Powers. Design and Analysis of a Supersonic Jet Noise Reduction Concept. AIAA Paper No. 2014-0525, January 2014.

[13] R. Powers, C. Kuo, D. McLaughlin, and P. Morris. Supersonic Jet Noise Reduction by Nozzle Fluidic Inserts with Simulated Forward Flight. AIAA Paper No. 2014-2474, June 2014.

[14] J. Larsson, S. Kawai, J. Bodart, and I. Bermejo-Moreno. Large eddy simulation with modeled wall-stress: recent progress and future directions. *Mechanical Engineering Reviews*, 3(1):15–00418, 2016.

[15] D. Chapman. Computational Aerodynamics Development and Outlook. *AIAA Journal*, 17(12):1293–1313, 12 1979.

[16] N. Dhamankar, C. Martha, Y. Situ, K. Aikens, G. Blaisdell, A. Lyrintzis, and Z. Li. Digital Filter-based Turbulent Inflow Generation for Jet Aeroacoustics on Non-Uniform Structured Grids. AIAA Paper No. 2014-1401, January 2014.

[17] C. Brown and J. Bridges. Small hot jet acoustic rig validation. Technical Report 214234, NASA Technical Memorandum, 2006.

[18] J. Deardorff. A numerical study of three-dimensional turbulent channel flow at large reynolds numbers. *Journal of Fluid Mechanics*, 41(2):453–480, 1970.

[19] U. Piomelli and E. Balaras. Wall-layer models for large-eddy simulations. *Annual Review of Fluid Mechanics*, 34(1):349–374, 1 2002.

[20] U. Piomelli. Wall-layer models for large-eddy simulations. *Progress in Aerospace Sciences*, 44(6):437–446, 8 2008.

[21] S. Kawai and J. Larsson. Wall-modeling in large eddy simulation: Length scales, grid resolution, and accuracy. *Physics of Fluids*, 24(1):015105, 1 2012.

[22] U. Schumann. Subgrid scale model for finite difference simulations of turbulent flows in plane channels and annuli. *Journal of Computational Physics*, 18(4):376 – 404, 1975.

[23] G. Grotzbach. Direct numerical and large eddy simulations of turbulent channel flow. In *Encyclopedia of fluid mechanics: Volume 6*, pages 1337–1391. Gulf Publishing Company, Houston, TX, 1987.

[24] X. Wu and K. Squires. Prediction of the three-dimensional turbulent boundary layer over a swept bump. *AIAA Journal*, 36(4):505–514, 1998.

[25] U. Piomelli, J. Ferziger, P. Moin, and J. Kim. New approximate boundary conditions for large eddy simulations of wallbounded flows. *Physics of Fluids A: Fluid Dynamics*, 1(6):1061–1068, 6 1989.

[26] S. Rajagopalan and R. Antonia. Some properties of the large structure in a fully developed turbulent duct flow. *The Physics of Fluids*, 22(4):614–622, 1979.

[27] P. Mason and N. Callen. On the magnitude of the subgrid-scale eddy coefficient in large-eddy simulations of turbulent channel flow. *Journal of Fluid Mechanics*, 162:439462, 1986.

[28] H. Werner and H. Wengle. Large-eddy simulation of turbulent flow over and around a cube in a plane channel. In *Turbulent Shear Flows 8*, pages 155–168. Springer Berlin Heidelberg, 1993.

[29] D. Spalding. A Single Formula for the Law of the Wall. *Journal of Applied Mechanics*, 28(3):455, 1961.

[30] G. Hoffmann and C. Benocci. Approximate wall boundary conditions for large eddy simulations. In *Advances in Turbulence V*, pages 222–228. Springer Netherlands, 1995.

[31] R. Simpson. Aspects of turbulent boundary-layer separation. *Progress in Aerospace Sciences*, 32(5):457 – 521, 1996.

[32] M. Wang. LES with wall models for trailing-edge aeroacoustics. In *Annual research briefs*, pages 355–364. Center for Turbulence Research, Stanford University, 1999.

[33] T. Shih, L. Povinelli, and N. Liu. Application of generalized wall function for complex turbulent flows. *Journal of Turbulence*, 4:N15, 2003.

[34] E. Balaras, C. Benocci, and U. Piomelli. Two-layer approximate boundary conditions for large-eddy simulations. *AIAA Journal*, 34(6):1111–1119, 6 1996.

[35] E. Diurno, G.and Balaras and U Piomelli. Wall-layer models for LES of separated flows. In *Modern simulation strategies for turbulent flow*, pages 157–174, 2001.

[36] P. Spalart and S. Allmaras. A one-equation turbulence model for aerodynamic flows. AIAA Paper No. 1992-439, January 1992.

[37] M. Wang and P. Moin. Dynamic wall modeling for large-eddy simulation of complex turbulent flows. *Physics of Fluids*, 14(7):2043–2051, 2002.

[38] S. Kawai and J. Larsson. Dynamic non-equilibrium wall-modeling for large eddy simulation at high reynolds numbers. *Physics of Fluids*, 25(1):015105, 2013.

[39] F. Nicoud, J. Baggett, P. Moin, and W. Cabot. Large eddy simulation wall-modeling based on suboptimal control theory and linear stochastic estimation. *Physics of Fluids*, 13(10):2968–2984, 10 2001.

[40] N. Nikitin, F. Nicoud, B. Wasistho, K. Squires, and P. Spalart. An approach to wall modeling in large-eddy simulations. *Physics of Fluids*, 12(7):1629–1632, 7 2000.

[41] R. Baurle, C. Tam, J. Edwards, and H. Hassan. Hybrid simulation approach for cavity flows: blending, algorithm, and boundary treatment issues. *AIAA journal*, 41(8):1463–1480, 2003.

[42] L. Temmerman, M. Hadžiabdić, M. Leschziner, and K. Hanjalić. A hybrid two-layer urans–les approach for large eddy simulation at high reynolds numbers. *International journal of heat and fluid flow*, 26(2):173–190, 2005.

[43] U. Piomelli, E. Balaras, H. Pasinato, K. Squires, and P. Spalart. The inner - outer layer interface in large-eddy simulations with wall-layer models. *International Journal of Heat and Fluid Flow*, 24(4):538–550, 8 2003.

[44] JS Baggett. On the feasibility of merging LES with RANS for the near-wall region of attached turbulent flows. In *Annual Research Briefs*, pages 267–277. Center for Turbulence Research, Stanford University, 1998.

[45] K. Aikens. *High-Fidelity Large Eddy Simulation for Supersonic Jet Noise Prediction*. PhD thesis, Purdue University, West Lafayette, 2014.

[46] C. Martha. *Toward High-Fidelity Subsonic Jet Noise Prediction using Petascale Supercomputers*. PhD thesis, Purdue University, May 2013.

[47] Y. Situ. *Scaling Finite Difference Methods in Large Eddy Simulation of Jet Engine Noise to the Petascale: Numerical Methods and Their Efficient and Automated Implementation*. PhD thesis, Purdue University, December 2014.

[48] N. Dhamankar. Boundary Conditions Towards Realistic Simulation of Jet Engine Noise, Master's Thesis. Purdue University, 2012.

[49] N. Dhamankar. *An Immersed Boundary Method for Efficent Computational Studies of Nozzles Designsed to Reduce Jet Noise*. PhD thesis, Purdue University, 2016.

[50] K. Aikens, N. Dhamankar, Y. Situ, Y. Wang, Z. Li, G. Blaisdell, and A. Lyrintzis. Towards petascale computing for realistic jet noise simulations. WSEAS 17th International Conference on Computers, Rhodes Island, Greece, July 2013.

[51] K. Aikens, N. Dhamankar, C. Martha, Y. Situ, G. Blaisdell, A. Lyrintzis, and Z. Li. Equilibrium Wall Model for Large Eddy Simulations of Jets for Aeroacoustics. AIAA Paper No. 2014-0180, January 2014.

[52] K M Aikens, G A Blaisdell, A S Lyrintzis, and Z Li. Analysis of converging-diverging beveled nozzle jets using large eddy simulation with a wall model. AIAA Paper No. 2015-0509, January 2015.

[53] M. Coderoni, A. Lyrintzis, and G. Blaisdell. Aeroacoustics of supersonic jets with fluidic injection. AIAA Paper No. 2017-3210, June 2017.

[54] M. Coderoni, A. Lyrintzis, and G. Blaisdell. Les of unheated and heated supersonic jets with fluidic injection. AIAA paper No. 2018-0519, January 2018.

[55] M. Coderoni. *A Computational Analysis of the Aerodynamics and Aeroacoustics of Jets with Fluid Injection*. PhD thesis, Embry-Riddle Aeronautical University, July 2018.

[56] H. Tanna, P. Dean, and R. Burrin. The Generation and Radiation of Supersonic Jet Noise. Volume 3. Turbulent Mixing Noise Data. *Technical Report AFAPLTR76-65*, 1976.

[57] C. Bogey, O. Marsden, and C. Bailly. Influence of initial turbulence level on the flow and sound fields of a subsonic jet at a diameter-based Reynolds number of 10ˆ5. *Journal of Fluid Mechanics*, 701(2012):352–385, 6 2012.

[58] R. Narasimha and K. Sreenivasan. Relaminarization in highly accelerated turbulent boundary layers. *Journal of Fluid Mechanics*, 61(03):417–447, 1973.

[59] K. Sreenivasan. Laminarescent, relaminarizing and retransitional flows. *Acta Mechanica*, 44(1-2):1–48, 1982.

[60] T. Shih, L. Povinelli, N. Liu, M. Potapczuk, and J. Lumley. A Generalized Wall Function. Technical memorandum 209398, NASA, 1999.

[61] X. Yang, J. Sadique, R. Mittal, and C. Meneveau. Integral wall model for large eddy simulations of wall-bounded turbulent flows. *Physics of Fluids*, 27(2):025112, 2 2015.

[62] J. Bridges and M. Wernet. The NASA Subsonic Jet Particle Image Velocimetry (PIV) Dataset. Technical memorandum 216807, NASA, 2011.

[63] A. Uzun. *3-D Large Eddy Simulation for Jet Aeroacoustics*. PhD thesis, Purdue University, December 2003.

[64] S. Lo. *Numerical Simulations of Supersonic Jet Flows*. PhD thesis, Purdue University, 2010.

[65] J. Smagorinsky. General Circulation Experiments with the Primitive Equations. *Monthly Weather Review*, 91(3):99–164, 1963.

[66] P Moin, K Squires, W Cabot, and Sangsan Lee. A dynamic subgrid-scale model for compressible turbulence and scalar transport. *Physics of Fluids A: Fluid Dynamics*, 3(11):2746–2757, 1991.

[67] F. Nicoud and F. Ducros. Subgrid-scale stress modelling based on the square of the velocity gradient tensor. *Flow, Turbulence and Combustion*, 62:183–200, 1999.

[68] M. Visbal and D. Gaitonde. On the Use of Higher-Order Finite-Difference Schemes on Curvilinear and Deforming Meshes. *Journal of Computational Physics*, 181:155–185, 2002.

[69] M. Visbal, P. Morgan, and D. Rizzetta. An Implicit LES Approach Based on High-order Compact Differencing and Filtering Schemes (Invited). AIAA Paper No. 2003-4098, June 2003.

[70] D. Rizzetta, M. Visbal, and G. Blaisdell. A time-implicit high-order compact differencing and filtering scheme for large-eddy simulation. *International Journal for Numerical Methods in Fluids*, 42(6):665–693, 2003.

[71] A. Uzun, G. Blaisdell, and A. Lyrintzis. Impact of Subgrid-Scale Models on Jet Turbulence and Noise. *AIAA Journal*, 44(6):1365–1368, june 2006.

[72] F. Grinstein, L. Margolin, and W. Rider. *Implicit Large Eddy Simulation: Computing Turbulent Fluid Dynamics*. Cambridge University Press, 2007.

[73] P. Thomas and C. Lombard. Geometric conservation law and its application to flow computations on moving grids. *AIAA Journal*, 17(10):1030–1037, 1978.

[74] T. Pulliam and J. Steger. Implicit Finite-Difference Simulations of Three-Dimensional Compressible Flow. *AIAA Journal*, 18(2):159–167, 1980.

[75] M. Visbal and D. Gaitonde. Very High-Order Spatially Implicit Schemes for Computational Acoustics on Curvilinear Meshes. *Journal of Computational Acoustics*, 09(04):1259–1286, 2001.

[76] X. Deng, M. Mao, G. Tu, H. Liu, and H. Zhang. Geometric conservation law and applications to high-order finite difference schemes with stationary grids. *Journal of Computational Physics*, 230(4):1100–1115, 2011.

[77] S. Lele. Compact finite difference schemes with spectral-like resolution. *Journal of Computational Physics*, 103(1):16–42, 1992.

[78] D. Gaitonde and M. Visbal. High-order schemes for Navier-Stokes equations: algorithm and implementation into FDL3DI. *Air Vehicles Directorate*, page 50, 1998.

[79] K. Mohseni and T. Colonius. Numerical Treatment of Polar Coordinate Singularities. *Journal of Computational Physics*, 157(2):787–795, 1 2000.

[80] C. Bogey, N. Cacqueray, and C. Bailly. Finite differences for coarse azimuthal discretization and for reduction of effective resolution near origin of cylindrical flow equations. *Journal of Computational Physics*, 230(4):1134–1146, 2011.

[81] T. Lund, X. Wu, and K. Squires. Generation of Turbulent Inflow Data for Spatially-Developing Boundary Layer Simulations. *Journal of Computational Physics*, 140(2):233–258, 3 1998.

[82] N. Dhamankar, G. Blaisdell, and A. Lyrintzis. Overview of Turbulent Inflow Boundary Conditions for Large-Eddy Simulations. *AIAA Journal*, 56(4):1317–1334, 2018.

[83] Z. Xie and I. Castro. Efficient Generation of Inflow Conditions for Large Eddy Simulation of Street-Scale Flows. *Flow, Turbulence and Combustion*, 81(3):449–470, 10 2008.

[84] E. Touber and N. Sandham. Large-eddy simulation of low-frequency unsteadiness in a turbulent shock-induced separation bubble. *Theoretical and Computational Fluid Dynamics*, 23(2):79–107, 6 2009.

[85] C. Tam and Z. Dong. Radiation and Outflow Boundary Conditions for Direct Computation of Acoustic and Flow Disturbances in a Nonuniform Mean Flow. *Journal of Computational Acoustics*, 04(02):175–201, 6 1996.

[86] C. Bogey and C. Bailly. Three-dimensional non-reflective boundary conditions for acoustic simulations: far field formulation and validation test cases. *Acta Acustica united with Acustica*, 88:463–471, 2002.

[87] T. Colonius, S. Lele, and P. Moin. Boundary Conditions for Direct Computation of Aerodynamic Sound Generation. *AIAA Journal*, 31(9), 1993.

[88] J. Kim and D. Lee. Generalized Characteristic Boundary Conditions for Computational Aeroacoustics. *AIAA Journal*, 38(11):2000, 2000.

[89] G. Lodato, P. Domingo, and L. Vervisch. Three-dimensional boundary conditions for direct and large-eddy simulation of compressible viscous flows. *Journal of Computational Physics*, 227(10):5105–5143, 2008.

[90] M. Louis. Validation of characteristic boundary conditions implemented in computational aeroacoustics large eddy simulations of wall bounded flows. Master's thesis, Purdue University, December 2011.

[91] DK Lilly. A proposed modification of the Germano subgrid-scale closure method. *Physics of Fluids A: Fluid Dynamics*, 4(3):633–635, 1992.

[92] E. Polizzi and A. Sameh. A parallel hybrid banded system solver: the SPIKE algorithm. *Parallel Computing*, 32(2):177–194, 2006.

[93] Y. Situ, L. Liu, C. Martha, M. Louis, Z. Li, A. Sameh, G. Blaisdell, and A. Lyrintzis. A communication-efficient linear system solver for large eddy simulation of jet engine noise. *Cluster Computing*, 16(1):157–170, 2013.

[94] Y. Situ, C. Martha, M. Louis, Z. Li, A. Sameh, G. Blaisdell, and A. Lyrintzis. Petascale large eddy simulation of jet engine noise based on the truncated SPIKE algorithm. *Parallel Computing*, 40(9):496–511, 10 2014.

[95] M. Shur, P. Spalart, and M. Strelets. Noise prediction for increasingly complex jets. part I: Methods and tests. *International Journal of Aeroacoustics*, 4(3–4):213–246, 2005.

[96] S. Mendez, M. Shoeybi, Lele. S., and P. Moin. On the use of the Ffowcs Williams–Hawkings equation to predict far-field jet noise from large-eddy simulations. *International Journal of Aeroacoustics*, 12(1&2):1–20, 2013.

[97] T. Ikeda, S. Enomoto, K. Yamamoto, and K. Amemiya. On the Modification of the Ffowcs Williams-Hawkings Integration for Jet Noise Prediction. AIAA Paper No. 2013-2277, May 2013.

[98] T. Ikeda, S. Enomoto, K. Yamamoto, and K. Amemiya. Quadrupole corrections for the permeable-surface ffowcs williams-hawkings equation. *AIAA Journal*, 55(7):2307–2320, 2017.

[99] Tomoaki Ikeda, Shunji Enomoto, and Kazuomi Yamamoto. Quadrupole effects in the Ffowcs Williams–Hawkings equation using permeable control surface. AIAA Paper No. 2012-2069, June 2012.

[100] J. Freund. Noise sources in a low-Reynolds-number turbulent jet at Mach 0.9. *Journal of Fluid Mechanics*, 438:277–305, 2001.

[101] H. Tennekes and J. Lumley. *A First Course in Turbulence*. MIT Press, 1972.

[102] H. Tennekes. Outline of a second-order theory of turbulent pipe flow. *AIAA Journal*, 6(9):1735–1740, 9 1968.

[103] R. Panton. *Incompressible Flow*. John Wiley & Sons, Inc., Hoboken, NJ, USA, 7 2013.

[104] P. Huang, P. Bradshaw, and T. Coakely. Turbulence models for compressible boundary layers. *AIAA Journal*, 32(4):735–740, 4 1994.

[105] D. Sondak and R. Pletcher. Application of wall functions to generalized nonorthogonal curvilinear coordinate systems. *AIAA Journal*, 33(1):33–41, 1 1995.

[106] J. Bridges and C. Brown. Validation of the Small Hot Jet Acoustic Rig for Aeroacoustic Research. AIAA Paper No. 2005-2846, May 2005.

[107] T. Dong. On Boundary Conditions for Acoustic Computations in Non-Uniform Mean Flows. *Journal of Computational Acoustics*, 05(03):297–315, 9 1997.

[108] J. Liu. A Brief Note on Implementing Boundary Conditions at a Solid Wall Using the FCT Algorithm. Technical Report NRL/MR/16410–06-8943, Naval Research Laboratory, 2006.

[109] P. Spalart. Direct simulation of a turbulent boundary layer up to $R_\theta = 1410$. *Journal of Fluid Mechanics*, 187(1):61–98, 1988.

[110] G. Brès, V. Jaunet, M. Le Rallic, P. Jordan, T. Colonius, and S. Lele. Large eddy simulation for jet noise: the importance of getting the boundary layer right. AIAA Paper No. 2015-2535, 6 2015.

[111] P S Klebanoff. Characteristics of turbulence in boundary layer with zero pressure gradient. NACA-TR-1247, 1955.

[112] U Piomelli and J Yuan. Numerical simulations of spatially developing, accelerating boundary layers. *Physics of Fluids*, 25(10):101304, 2013.

[113] D Warnack and H Fernholz. The effects of a favourable pressure gradient and of the Reynolds number on an incompressible axisymmetric turbulent boundary layer. Part 2. The boundary layer with relaminarization. *Journal of Fluid Mechanics*, 359:357–381, 1998.

[114] M. Narayanan and V. Ramjee. On the criteria for reverse transition in a two-dimensional boundary layer flow. *Journal of Fluid Mechanics*, 35(02):225, 1 1969.

[115] W. Jones and B. Launder. Some properties of sink-flow turbulent boundary layers. *Journal of Fluid Mechanics*, 56(02):337, 11 1972.

[116] P. Spalart. Numerical study of sink-flow boundary layers. *Journal of Fluid Mechanics*, 172(1):307, 11 1986.

[117] A. Townsend. *The Structure of Turbulent Shear Flow*. Cambridge University Press, 2 edition, 1976.

[118] U. Piomelli, E. Balaras, and A. Pascarelli. Turbulent structures in accelerating boundary layers. *Journal of Turbulence*, 1(May):N1, 1 2000.

[119] H. Fernholz and D. Warnack. The effects of a favourable pressure gradient and of the Reynolds number on an incompressible axisymmetric turbulent boundary layer. Part 1. The turbulent boundary layer. *Journal of Fluid Mechanics*, 359(May):357–381, 3 1998.

[120] A. Bernard, J. M. Foucaut, P. Dupont, and M. Stanislas. Decelerating Boundary Layer: A New Scaling and Mixing Length Model. *AIAA Journal*, 41(2):248–255, 2 2003.

[121] M. Marquillie, J.-P. Laval, and R Dolganov. Direct numerical simulation of a separated channel flow with a smooth profile. *Journal of Turbulence*, 9:1–23, 2008.

[122] J.-P. Laval. Direct numerical simulations of converging-diverging channel flow. In *Progress in Wall Turbulence: Understanding and Modeling*, pages 203–209, Dordrecht, 2011. Springer Netherlands.

[123] Z. Chen. *Wall Modeling for Implicit Large-Eddy Simulation*. PhD thesis, Technical University of Munich, 2011.

[124] M. Marquillie, U. Ehrenstein, and J.-P. Laval. Instability of streaks in wall turbulence with adverse pressure gradient. *Journal of Fluid Mechanics*, 681:205–240, 2011.

[125] DNS: 2-D Converging-Diverging Channel, Re=12600, 2018. Available online: `https://turbmodels.larc.nasa.gov/Other_DNS_Data/conv-div-channel12600.html`, last accessed on 1 June 2018.

[126] L. Kuban, J. Laval, W. Elsner, A. Tyliszczak, and M. Marquillie. LES modeling of converging-diverging turbulent channel flow. *Journal of Turbulence*, 13:N11, 2012.

[127] J. Bridges and M. Wernet. Measurements of the Aeroacoustic Sound Source in Hot Jets. AIAA Paper No. 2003-3130, May 2003.

[128] V. Arakeri, A. Krothapalli, V. Siddavaram, M. Alkislar, and L. Lourenco. On the use of microjets to suppress turbulence in a Mach 0.9 axisymmetric jet. *Journal of Fluid Mechanics*, 490(1):75–98, 2003.

[129] P. O. Witze. Centerline velocity decay of compressible free jets. *AIAA Journal*, 12(4):417–418, 1974.

[130] A. Karon and K. Ahuja. Effect of nozzle-exit boundary layer on jet noise. AIAA Paper No. 2013-0615, January 2013.

[131] M. Harper-Bourne. Jet noise measurements: Past and present. *International Journal of Aeroacoustics*, 9(4):559–588, 2010.

[132] K. Viswanathan. Aeroacoustics of hot jets. *Journal of Fluid Mechanics*, 516:39–82, 2004.

[133] M. Shur, P. Spalart, and M. Strelets. LES-based evaluation of a microjet noise reduction concept in static and flight conditions. *Journal of Sound and Vibration*, 330:4083–4097, 2011.

[134] C. Bogey, O. Marsden, and C. Bailly. Effects of moderate Reynolds numbers on subsonic round jets with highly disturbed nozzle-exit boundary layers. *Physics of Fluids*, 24(10):105107, 2012.

[135] A. Uzun and M. Hussaini. Some issues in large-eddy simulations for chevron nozzle jet flows. *Journal of Propulsion and Power*, 28(2):246–258, 2012.

[136] N. Dhamankar, A. Lyrintzis, and G. Blaisdell. Analysis of turbulent jet flow and associated noise with round and chevron nozzles using large eddy simulation. AIAA Paper No. 2016-3045, May-June 2016.

VITA

Shanmukesh Vankayala was born in Vijayawada, India in 1988 and completed high school in 2006. He graduated with a Bachelor of Technology (B.Tech.) degree in Aeronautical Engineering from Jawaharlal Nehru Technological University, Hyderabad, India in May, 2010 and then moved to the United States to pursue graduate studies. He obtained a Master's degree in Aerospace Engineering (M.A.E) from Auburn University, Auburn in August, 2012. He then joined Coca Cola Refreshments as a Software Developer and worked for one year. In Fall 2013, he joined the School of Aeronautics and Astronautics at Purdue University to obtain a doctoral degree. His research is focused in the areas of Computational Fluid Dynamics (CFD), Large Eddy Simulations (LES), Computational Aeroacoustics (CAA) and High Performance Computing (HPC).